CHALMERS

Modelling of Concrete Subjected to Cyclic Loading

RASMUS REMPLING

Department of Civil and Environmental Engineering
Division of Structural Engineering
CHALMERS UNIVERSITY OF TECHNOLOGY
Göteborg, Sweden 2009

THESIS FOR THE DEGREE OF DOCTOR OF PHILOSOPHY

Modelling of Concrete Subjected to Cyclic Loading

Rasmus Rempling

8 February 2009

Department of Civil and Environmental Engineering
Division of Structural Engineering
Concrete Structures
CHALMERS UNIVERSITY OF TECHNOLOGY

Göteborg, Sweden, 2009

Modelling of Concrete Subjected to Cyclic Loading
Rasmus Rempling
ISBN 978-91-7385-246-3

Doktorsavhandling vid Chalmers tekniska högskola
Ny serie 2927
ISSN 0346-718X

Department of Civil and Environmental Engineering
Division of Structural Engineering
Concrete Structures
Chalmers University of Technology
SE-412 96 Göteborg
Sweden
Telephone +46 (0)31-772 1000

Chalmers Reproservice
Göteborg, Sweden, 2009

Till min far, min mor och mina bröder.

This page intentionally contains only this sentence.

Modelling of Concrete Subjected to Cyclic Loading

RASMUS REMPLING
Department of Civil and Environmental Engineering
Division of Structural Engineering
Concrete Structures
CHALMERS UNIVERSITY OF TECHNOLOGY

Abstract

The infrastructure of today depends heavily on concrete structures. Most of these structures are subjected to repeated loads, known as fatigue or cyclic loads: the loads weaken the structure. As this phenomenon is of high cost to society, a deeper understanding of the deterioration process of cyclic loading would be beneficial. The aim of this thesis is to add to the knowledge of the deterioration phenomenon and to develop models that can describe the response of concrete subjected to cyclic loading.

In analyses of structures of today, finite element modelling is gaining ground and is being used more frequently in research and structural design. The investigations here use only the finite element method.

Many structures incorporate details that are subjected to complicated loading, which results in complex crack patterns. A suitable tool for describing these crack patterns is anisotropic damage material models. However, anisotropic models are difficult to implement and are often computationally inefficient. One of the investigations in this thesis aims to find out what makes the anisotropic formulation suitable for complex crack patterns. This is done by implementing a model which can control the amount of coupling between volumetric- and deviatoric strains. It was found that this coupling is essential for describing complex crack patterns.

To deepen the understanding of concrete subjected to cyclic loading, the phenomenon was investigated on the meso-scale level. An interface model was developed and applied to a three phase representation of concrete that incorporates: aggregates, cement paste, and interfacial zones around the aggregate. The model in itself does not yield cyclic behaviour, i.e. no hysteresis loops were generated at the constitutive level. Instead, the cyclic response was generated by the meso-structure. It was found that the interfacial transition zones are crucial in amount and strength.

Concrete subjected to cyclic loading was also investigated on the macro-level, with the ambition to describe the response of concrete structures subjected to cyclic loading. Two investigations were made: one aims to describe cyclic response in tension and the other aims to cover tension and the transition to reasonable high states of compression. The investigations are based on the theory of plasticity and damage mechanics, which are combined in both a serial and a parallel fashion. In the serial configuration the nominal stress is computed by adding the damage to the effective stress; for the parallel configuration, the damage stress and the effective stress are evaluated separately for the same strain and then added to yield the nominal stress. Furthermore, both models use two yield surfaces to describe the hysteresis loops. The result of the analyses show an overall agreement with experimental observations.

Key words: concrete, plasticity, damage, cyclic loading, energy dissipation

Modelling of Concrete Subjected to Cyclic Loading

RASMUS REMPLING
Department of Civil and Environmental Engineering
Division of Structural Engineering
Concrete Structures
CHALMERS UNIVERSITY OF TECHNOLOGY

Sammanfattning

Vår infrastruktur är idag i viss mån beroende av betongkonstruktioner varav många utsätts för upprepade laster. Upprepad last med miljontals repetitioner är mer känt som utmattningslast, dvs att konstruktionen utmattas av den återkommande lasten. Om repetitionerna däremot är få till antalet benämns upprepad last ofta som cyklisk last. Utmattning av konstruktioner är en kännbar ekonomisk kostnad för samhället, en kostnad som skulle kunna begränsas av en djupare förståelse. Målet med denna avhandling är att bidra till kunskapsuppbyggnad om utmattning av betongkonstruktioner och att utveckla modeller som kan beskriva betongens cykliska respons.

Betongkonstruktioner innehåller ofta detaljer som utsätts för komplexa belastningsmönster. Sådana fall kan ge komplicerade sprickmönster. Tidigare har det visat sig att man tillfredsställande kan beskriva komplicerade sprickmönster med anisotropa skademodeller. Dessvärre är anisotropa skademodeller ofta svåra att implementera samtidigt som de behöver stor datorkapacitet. I denna avhandling görs ett försök att identifiera vad som gör den anisotropa formuleringen gynnsam för komplicerade sprickmönster. För den studien utvecklades en konstitutiv modell där det är möjligt att kontrollera graden av koppling mellan volumetriska och deviatoriska töjningar. Resultatet påvisar att den identifierade kopplingen är avgörande för att kunna beskriva komplicerade sprickmönster.

För att fördjupa förståelsen för betong som utsätts för cyklisk belastning gjordes en studie på mesoskala. På mesoskala definieras betong som ett material i tre faser: ballast, cementpasta, samt svaghetszoner som skiljer ballast från pasta. Den cykliska responsen är inte beskriven på konstitutiv nivå. Istället ges den cykliska responsen av materialstrukturen. Resultaten påvisar att de svaga zonerna mellan ballast och cementpasta är avgörande för att beskriva cyklisk belastning.

Mesoskala innebär ofta ett större krav på datorkapacitet och är således inte lämpligt för studier av större konstruktioner. För studier av större konstruktioner är i dagsläget makroskala ett bättre alternativ. På makroskala definieras betong som ett homogent material. Inledningsvis studeras cyklisk belastning i drag som därefter expanderas till att också omfatta tryck och lastväxling. Båda studierna baseras på skademekanik och plasticitet som kombineras dels i serie men också parallellt. Resultatet påvisar god överensstämmelse med experimentella observationer.

Nyckelord: betong, plasticitet, skada, cyklisk belastning, energidissipation

Contents

Preface

The thesis deals with fracture of concrete subjected to cyclic loading. It also explores the stress transition between tension and compression, and vice versa, while unloading in tension. The study was carried out at the Department of Civil and Environmental Engineering, Division of Structural Engineering, Concrete Structures, at Chalmers University of Technology in Göteborg, Sweden. The thesis work was made possible by the financial support of the Foundation of Swedish Council for Environment, Agricultural Sciences and Spatial Planning (FORMAS).

The main supervisor and examiner of the work is Professor Kent Gylltoft. Kent Gylltoft is a trustworthy supervisor. His stable personality ensures a creative environment. His experience in the fatigue of concrete has made this work possible.

My assistant supervisors are Associate Professor Karin Lundgren and Per-Ola Svahn, Ph.D., (Skanska Sverige AB), whose experience and knowledge have been very valuable. Karin Lundgren has given me valuable advice and guidance in theory. Her questions and comments are always fruitful and constructive. Per-Ola Svahn introduced a new perspective to my work. His effectiveness and ability to see things in a different light, ranging from the tiniest detail to a high overall perspective, is unique.

Peter Grassl, Ph.D., has had a great influence on my work and deserves warm thanks. He introduced me to the world of constitutive modelling, C++, and the finite element program OOFEM. He has a great capacity as researcher and is able to see where good research can be done. To him I would trust any task. Associate Professor Fredrik Larsson, despite his many projects, has assisted in theory and given crucial advice for the work. A person who deserves an honour is Professor Emeritus Ralejs Tepfers who did pioneering work on concrete and fatigue at Chalmers and despite his 75 years still does advanced research.

It is a privilege to be accepted as doctoral student at the Division of Structural Engineering, Chalmers because you get the time to understand ideas and let your thoughts mature. The creative environment and people are unique. I want to express my appreciation to Kent Gylltoft, Björn Engström and Karin Lundgren for accepting my application. In addition, I want to thank my colleagues at Chalmers for their support and valuable advice during the realisation of the work. In particular, Ingemar Löfgren, Helén Broo, Mohammad Al-Emrani, Mario Plos, Joosef Leppänen and Hendrik Schlune deserve warm thanks for their discussions on the response of concrete and their interest in the progress of my work. I will miss the guidance in travelling that I had with Helén Broo :).

I want to thank all my friends and family for being there, supporting and cheering me on towards the finish. Two friends whom I miss especially are Andreas Andersson and Håkon Langen; the past years have lacked the great mountain trips that we love. I have felt that I was the brake. It is time to make up for lost ground!

Jenny, my life co-driver and joy, is loving, understanding and supportive. She listens, agrees, and disagrees. She shares my innermost thoughts as I share hers. She has given me what I value most – Erik.

D.R. Rempling, Göteborg, 2009

List of publications

This thesis consists of an introduction and six appended papers, referred to by Roman numerals in the text:

I Grassl, P.; Rempling, R. (2007). Influence of volumetric-deviatoric coupling on crack prediction in concrete fracture tests. *Engineering Fracture Mechanics*. 74 (10) pp. 1683–1693.

II Rempling, R.; Lundgren, K.; Gylltoft, K. (2008). Modelling of concrete in tension – Energy dissipation in cyclic loops. *Nordic Concrete Research*. (38) pp. 155–168.

III Grassl, P.; Rempling, R. (2008). A damage-plasticity interface approach to the meso-scale modelling of concrete subjected to cyclic compressive loading. *Engineering Fracture Mechanics*. 75 (16) pp. 4804–4818.

IV Rempling, R.; Grassl, P. (2008). A parametric study of the meso-scale modelling of concrete subjected to cyclic compression. *Computers and concrete*. 5 (4) pp. 359–373.

V Rempling, R.; Svahn, P-O.; Lundgren, K.; Gylltoft, K. (2008). Constitutive modelling of concrete subjected to cyclic loading, including stress reversal. Submitted to *Int. Journal of Fatigue*.

Other publications within the project

1 Rempling, R.; Svahn, P-O.; Lundgren, K.; Gylltoft, K. (2008). A dual model describing concrete subjected to cyclic loading. *The Proceedings of Nordic Concrete Research*. June. Bålsta, Sweden. (1) pp. 206–207.

2 Rempling, R.; Grassl, P. (2008). Interpretation of fatigue mechanisms by means of a meso-scale model. *The Proceedings of Nordic Concrete Research*. June. Bålsta, Sweden. (1) pp. 204–205.

3 Plos, M.; Lundgren, K.; Rempling, R. et al. (2007). Non-Linear Analysis and Remaining Fatigue Life. Report. Sustainable Bridges. pp 185.

4 Rempling, R.; Grassl, P. (2007). How volumetric-deviatoric coupling influences the crack prediction in concrete fracture tests. *Proceedings of the 6th Int. Conf. on Fracture Mechanics of Concrete and Concrete Structures (FRAMCOS)*. June. Catania, Italy. (1) pp. 197–204.

5 Rempling, R. (2007). *Constitutive modelling of concrete subjected to monotonic and cyclic loading*. Licenciate Thesis. Department of Structural Engineering. Chalmers University of Technology. Göteborg, Sweden. p. 24.

6 Rempling, R.; Lundgren, K.; Gylltoft, K. (2007). Constitutive modelling of concrete subjected to tensile cyclic loading. *The Third International Conference on Structural Engineering, Mechanics and Computation*. Sept. Capetown. South Africa. pp. 197–198.

7 Rempling, R. (2006). Implementation of constitutive model for concrete subjected to tensile and compressive loading. Report. Department of Structural Engineering. Chalmers University of Technology. Göteborg, Sweden.

8 Rempling, R.; Lundgren, K.; Gylltoft, K. (2006). Utmattning av betongkonstruktioner (Fatigue of concrete structures). *Bygg och teknik*. (7) pp. 30–31.

9 Rempling, R.; Lundgren, K.; Gylltoft, K. (2005). Constitutive Model for Concrete Subjected to Cyclic Loading; Bi-axial Tension. *The Proceedings of Nordic Concrete Research Meeting*. June. Sandefjord, Norway. pp. 296–298.

Statement of contributions to jointly prepared papers

My own contributions to the appended papers are described.

Paper I
Participated in the planning and writing of the paper.
Participated in the development of the constitutive model.
Took part in the implementation of the model in a FE code.
Carried out the FE analyses.

Paper II
Did the main part of the planning and the writing of the paper.
Was responsible for the development of the constitutive model.
Implemented the model in a FE code.
Carried out the FE analysis.

Paper III
Participated in the planning and writing of the paper.
Took part in the development of the constitutive model.
Shared responsibility in the implementation of the model in a FE code.
Shared responsibility for the FE analyses.

Paper IV
Participated in the planning and writing of the paper.
Took part in the development of the constitutive model.
Shared responsibility for the the implementation of the model in a FE code.
Shared responsibility for the FE analyses.

Paper V
Responsible for the planning and writing of the paper.
Responsible for the development of the constitutive model.
Implemented the model in a FE code.
Carried out the FE analyses.

Nomenclature

$\dot{}$	Superscript: Rate of ...
$_{\mathrm{p}}$	Subscript: Plastic part of ...
$_{\rho}$	Subscript: Deviatoric part of ...
$_{\xi}$	Subscript: Volumetric part of ...
$\boldsymbol{D}_{\mathrm{ep}}$	Tangential stiffness matrix
$\boldsymbol{D}_{\mathrm{e}}$	Elastic stiffness matrix
$\boldsymbol{D}_{\mathrm{s}}$	Secant stiffness matrix
D	Dissipation of energy
F	Bounding surface function
f	Loading and yield functions
f_{D}	Damage loading function
f_{t}	Ultimate strength in tension
G	Elastic shear modulus
g	Plastic potential
g_{D}	Damage evolution function
H_{p}	Hardening modulus
I_1	First stress invariant
J_2	Second stress invariant
K	Elastic bulk modulus
$\hat{L}$	Bounding surface flow rule
M	Mapping rule
q_{n}	An internal variable
$R_{1,2,3}$	Residuals for the plastic part
$\boldsymbol{s}$	Deviatoric part of the stress

u	Displacement
x	State variable
α_{e}	Distribution of free energy between damage and plastic parts
α_{ϕ}	Dilatancy coefficient of the outer-yield surface potential
δ	Distance from elastic domain to bounding surface
$\boldsymbol{\delta}$	Kronecker delta
$\tilde{\varepsilon}$	Equivalent strain
ε_{f}	Uni-axial strain for which no stress transfer is possible
$\boldsymbol{\varepsilon}$	Strain tensor
κ	History variable
λ	Plastic multiplier
ω	Damage variable
ψ	Free energy
ρ	Haigh-Westergaard coordinate for the deviatoric stress
ρ_{ψ}	Mass density
σ_{v}	Volumetric part of the stress tensor
$\bar{\boldsymbol{\sigma}}$	Effective stress tensor
$\hat{\boldsymbol{\sigma}}$	Bounding surface stress tensor
$\boldsymbol{\sigma}$	Stress tensor
θ	Lode angle
ξ	Haigh-Westergaard coordinate for the volumetric stress

1 Introduction

1.1 Problem description

A realistic description of concrete subjected to cyclic loading becomes increasingly important as detailed analyses are more frequently used for design and evaluation. Detailed analyses of concrete structures subjected to cyclic loading are more and more made by the finite element method. Thus, the method adopted for this study is solely the finite element method, which involves material models that describe the material behaviour. For cyclic loading these material models need to include several characteristics: hysteresis loops, stiffness degradation, softening and high and low-cycle fatigue. Consequently, the development of such a material model is a complex process and a deep understanding of the phenomenon is important. Hence, to help the understanding it is natural to focus on the essence of concrete subjected to cyclic loading, by investigating the phenomenon on different levels of observation.

1.2 Aim

The main objective of this thesis is to deepen the understanding of the mechanisms and the causes of concrete fatigue. For that purpose models were developed in meso and macro-scale which, inserted in a finite element framework, make it possible to realistically simulate and predict the load-carrying capacity and the structural behaviour of concrete structures subjected not only to monotonic loads, but especially to cyclic ones. Cyclic loads are, in other words, repeated loads that cyclically load, unload, and reload a structure. At a material point a loading cycle can be completed in tension, compression or as a stress reversal: cycles from tension to compression and back or vice versa. The results and methods will be of use in both existing and new structures, and to professionals such as researchers and practising engineers.

1.3 Limitations

This study concerns the behaviour of the phenomenon known as cyclic loading of concrete. It is limited to the modelling of the response of concrete subjected to monotonic and cyclic loading of a few cycles, whereas high cycle fatigue is not included. The study is limited to relatively low compressive stresses and low confined stress states. No experimental investigations were made, though several experimental results were used for calibrating and verifying numerical models. Experimental results also served as input for understanding the phenomenon. Small deformations are assumed in all modelling.

1.4 Scientific approach

The levels modelled in this thesis are meso and macro-scale. On meso-scale level, concrete was described as a heterogeneous material consisting of three phases: aggregates, cement paste and interfacial zones that bound the aggregates; on macro-scale level concrete was described as a homogeneous material. Moreover, with some exceptions the input parameters used in the analysis are engineering ones which can be evaluated by standard testing of materials, e.g. compressive tests. The macro-models can therefore be used for structural analysis and design.

1.5 Original features

Anisotropic damage mechanics has proven to be better at describing complex crack patterns than other types of theories; however, it is not yet known why. In this work it is shown that the coupling between volumetric strains and deviatoric strains is important for describing complex crack patterns on macro-scale.

In subjecting concrete to cyclic loading, the origin of the hysteresis loops seen in the response has been debated. To pursue this question and to contribute to the debate, an investigation on meso-scale was made. The method used was a numerical model, for a lattice approach to concrete subjected to cyclic loading, developed for this purpose. To the author's knowledge this is pioneering work, as cyclic loading has not, to this extent, been studied on the meso-level before. The model is configured so that the amount of elastic and inelastic strain can be varied. This makes it possible to investigate the differing parameters involved in concrete subjected to cyclic loading. The parameter that was identified as important for describing the response is the interfacial strength between aggregates and cement paste.

On macro-scale a model based on the bounding surface concept was developed. The model can take into account the dissipation of energy due to hysteresis loops and then adjust the response accordingly. Previous research on this by (Gylltoft, 1983) has been questioned by (Hordijk, 1991). To further deepen and support this hypothesis on energy dissipation, a material-model configuration not used before was developed and implemented. The configuration is based on the standard theories: damage mechanics and plasticity. However, the innovation is a parallel configuration with a material parameter which determines the influence of each part on the nominal response.

1.6 Outline

The thesis consists of six appended papers and an introductory part. The intention of the introductory part is to give a more comprehensive background to the appended papers.

In Chapter 2 the main characteristics of concrete subjected to cyclic load are treated. The question: "How does hardened concrete behave under tension, compression and fluctuating load?" is discussed. The basic theories used for the models introduced in Chapter 4 are given in Chapter 3. Furthermore, in Chapter 4 a short review of other "earlier" macro-scale constitutive models is given. Finally, in Chapter 5 the main conclusions are given together with suggestions for future research.

This page intentionally contains only this sentence.

2 Characteristics of concrete cyclic response

Although, investigations of non-reinforced concrete subjected to cyclic loading in compression are widely represented in the literature, (Tepfers, 1978; Holmen, 1979; Gylltoft, 1983; Gopalaratnam and Shah, 1985; Mier, 1986; Reinhardt et al., 1986; CEB, 1988; Thun, 2006; Gustafsson, 1985, among others), non-reinforced concrete subjected to cyclic loading in tension is not so widely reported (Tepfers, 1978; Gylltoft, 1983; Reinhardt, 1984; Gopalaratnam and Shah, 1985; Reinhardt et al., 1986; Hordijk, 1991, among others). As regards concrete subjected to a fluctuating load, the reported knowledge is very scarce. The first report about concrete subjected to a fluctuating load dates back to the 1920s, with (Clemmer, 1922) followed by (Crepps, 1923). Thirty years later (Murdock and Kesler, 1958) and (Murdock, 1965) presented a modified Goodman-diagram for concrete subjected to a fluctuating load. More recent reports found were (Tepfers, 1978; Gylltoft, 1983; Reinhardt, 1984; Reinhardt et al., 1986).

The rupture of a monotonically loaded concrete bar in tension, as shown in Figure 1, is a continuous increase of deformation that localises at the weakest section of the bar. At peak load the ultimate tensile strength of the bar is reached. In a load controlled experiment, the localisation is fast and the rupture is sudden. However, experiments with specific boundary conditions reveal a softening behaviour after peak-load, which is characteristic for concrete. The softening response is defined as a reduction in stress as deformation increases. The part that exhibits a softening behaviour is concentrated to the region with localised deformation, while sections outside the localisation zone behave differently. Outside the localisation zone, the material unloads elastically or with a small inelastic deformation, depending on the distance from the part that softens. Due to stress consistency, the stress in the softening part and the outside sections should be equal. The measured stress-deformation response results in a curve that represents the stress state for a given deformation of the material, when subjected to a monotonic load in tension. The curve is called the envelope; the stress-deformation state of the material cannot be outside the curve.

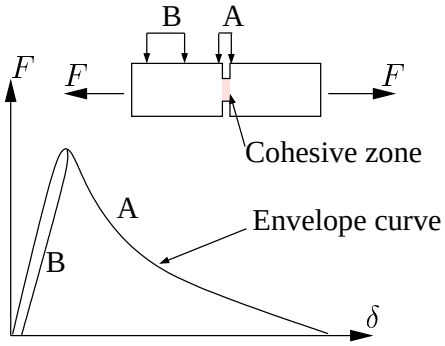

Figure 1: Response of a monotonic loaded concrete bar. A: localised zone; B: non-localised zone.

For cyclic loading the stress states do not follow the envelope curve of the monotonic response because of the repeated unloading and reloading; nevertheless, the envelope still bounds the admissible stress state. Low cycle fatigue is defined for concrete in the softening region, while high cycle fatigue dominates the non-elastic region before peak-load.

The response of high cycle fatigue in tension can only be initiated at the short interval of non-linear response before the peak-load, see Figure 2. Thus, high cycle fatigue is mainly dealt with in compression, for which the inelastic region before peak-load is essentially larger than for tension. The response of high cycle fatigue in tension, as well as in compression, exhibits plastic deformation which causes hysteresis loops with consistent dissipation of energy and stiffness degradation during the cycles. With an increased number of cycles the total deformation increases until the envelope curve is reached, (Hordijk, 1991). For tension this response is rather theoretical, as the non-linear region before peak-load is small. (Reinhardt, 1984) made tests on high cycle fatigue in tension, but was unable to find the non-linear region before peak-load, which should give irreversible deformation. Reinhardt chose the upper stress level initially at 85% of the tensile strength, which resulted in 457 cycles without reaching fracture. The stress level was then raised, but unfortunately the new stress level led directly to failure. Nevertheless, the phenomenon is still accepted by (Reinhardt, 1984) and his followers. To explain this phenomenon of

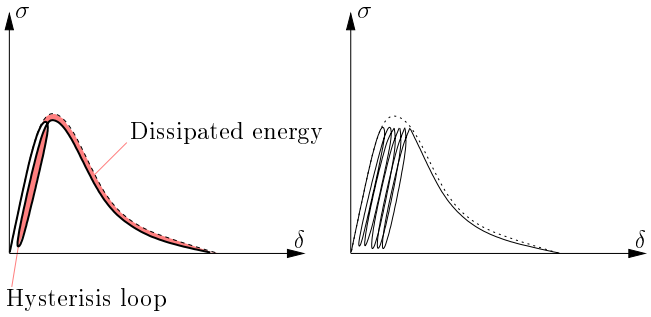

Figure 2: Illustration of the response due to high cycle fatigue.

increasing irreversible deformation, the stress distribution in front of a crack (Figure 3) can be interpreted before and after a loading cycle, assuming, at an applied load F, that only the crack-tip is softening, while the rest of the cross-section is still elastic. Before the loading cycle is initiated, the applied load F gives a stress distribution with a certain extension of the softening zone. However, when unloading the deformation, the material cannot unload the deformation totally because of the softened zone at the crack tip; still, the elastic deformations unload. The part of the softened material which has deformed beyond yielding must be compressed to follow the unloading deformation; this results in a self-equilibrating residual stress distribution when the external stresses are released. Consequently, the material is affected by unloading the deformation, and it is concluded that the parts of the material that are already affected by damage cannot resist the same stress when reloading the deformation. Therefore, the stress distribution is shifted into the material and, furthermore, the crack is extended; see (Reinhardt, 1984).

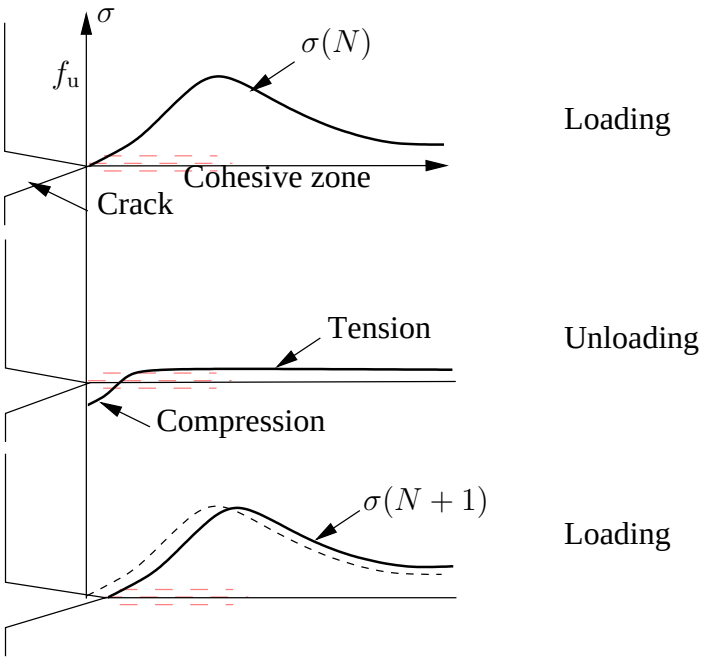

Figure 3: Illustration of the stress distribution at crack tip due to N cycles.

From investigations of the response of low cycle fatigue, such as (Gylltoft, 1983) and (Gopalaratnam and Shah, 1985), it has been found that a load cycle in the softening region causes energy to dissipate, so that the envelope of monotonic loading is not reached at reloading (Figure 4). The energy dissipates due to damage caused by the alternating plastic deformations, an idea initially introduced by (Gylltoft, 1983). This means that the energy dissipated by a load cycle is in fact dissipation of fracture energy. In addition, it has been shown that the stiffness decreases with every load cycle, (Reinhardt, 1984). Furthermore, the reloading stiffness in a load cycle seems to be smaller than the unloading stiffness of the same load cycle.

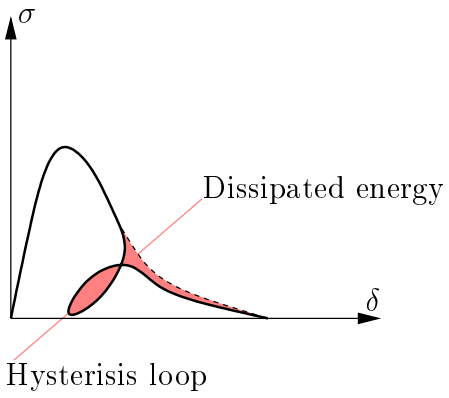

Figure 4: Illustration of the response due to low cycle fatigue.

The first hypothesis about the response of concrete subjected to cyclic loading from compression to tension, (Clemmer, 1922) and (Crepps, 1923), claimed that the fatigue strength is governed by the load which is the highest in comparison with the corresponding ultimate strength. In other words, if the stress in tension is almost the ultimate tensile stress, while the stress in compression is only a small portion of the ultimate compression strength, then the stress in tension governs the fatigue life of the detail, while the stress in compression is considered as zero. (Tepfers, 1978) put this hypothesis to the test and showed that the tendency to fatigue failure increases if the lower stress in a direct tension test is decreased to a relatively low state of uni-axial compression. This clearly contradicted the first hypothesis. (Reinhardt, 1984) contributed to the findings of Tepfers by concluding that the size of the hysteresis loops increases with increasing compression stress.

The response that concrete exhibits when subjected to a fluctuating load is clearly the same for compression and tension, if one disregards the intermediate region, where the active zone translates from one extreme to another. In the intermediate region the response of a part of the softened material enters a state of compression at a level of total deformation which depends on the amount of developed plastic deformation. More plastic deformation in tension results in a higher total deformation, at which the material-point changes state from tension to compression. During unloading the plastic deformation decreases continuously, although with a very low stiffness. In the state of compression the stiffness increases more and more until the original stiffness is almost reached, (Reinhardt et al., 1986).

3 Theoretical framework

3.1 Thermodynamical admissibility

All constitutive formulation needs to be thermodynamically admissible, which means that the energy dissipated from the model must be positive or the model generates energy. The state potential is often based on strain formulation and can be stated on a general form as

$$\rho_\psi \psi(\boldsymbol{\varepsilon}, \boldsymbol{x}) = 0 \tag{1}$$

where ρ_ψ is the material density, $\psi(\boldsymbol{\varepsilon}, \boldsymbol{x})$ is the state potential, $\boldsymbol{\varepsilon}$ is the strain and $\boldsymbol{x}$ is any state variable.

Normally, in constitutive modelling of brittle materials such as concrete, the thermal aspects are ignored. Thermodynamical admissibility can be shown by the Clausius-Duhem inequality. The dissipation rate of energy is often based on a strain formulation and is generally stated as

$$\dot{D} = \boldsymbol{\sigma} : \dot{\boldsymbol{\varepsilon}} - \rho_\psi \dot{\psi} \geq 0 \tag{2}$$

where $\boldsymbol{\sigma} : \dot{\boldsymbol{\varepsilon}}$ is the external work due to the nominal stress $\boldsymbol{\sigma}$, ρ_ψ is the material density, and $\dot{\psi}$ is the derivative of the state potential with respect to time.

If it is assumed that the state potential is linearised around the current value of every state variable, the derivative of the state potential can be written as

$$\dot{\psi} = \frac{\partial \psi}{\partial \boldsymbol{\varepsilon}} \dot{\boldsymbol{\varepsilon}} + \sum_{i=1}^{i} \frac{\partial \psi}{\partial \boldsymbol{x}_i} \dot{\boldsymbol{x}}_i. \tag{3}$$

3.2 The theory of plasticity

A brief description of the theory of plasticity is given in this section. The theory of plasticity is a formalisation of experimental observations on a deformable body, which aims to set up a relationship between effective stress $\bar{\boldsymbol{\sigma}}$ and strain $\boldsymbol{\varepsilon}$ that can represent the observed plastic deformations.

Plasticity models based on flow theory always consist of:

- a yield surface,
- a flow rule, and
- a hardening law,

which, together with the consistency condition, completely control the constitutive behaviour of the material. The consistency condition controls the loading and unloading and is defined by three equations:

$$f \leq 0 \qquad \dot{\lambda} \geq 0 \qquad \dot{\lambda} f = 0. \tag{4}$$

The yield surface f is defined by a set of stress states that satisfy the condition $f(\bar{\boldsymbol{\sigma}}) = 0$, for which plastic flow is present; this means that stress states of $f(\bar{\boldsymbol{\sigma}}) < 0$ are elastic stress states and $f(\bar{\boldsymbol{\sigma}}) = 0$ are plastic stress states.

The flow rule defines the plastic part of the strain (direction and quantity) when the yield surface is reached; plastic strain is utilised for describing the observed plastic deformation. The plastic strain direction is often defined by an associated flow rule $\frac{\partial f}{\partial \bar{\boldsymbol{\sigma}}}$, which results in a flow direction normal to the yield surface. For some applications it is more convenient to choose a non-associated flow rule $\frac{\partial g}{\partial \bar{\boldsymbol{\sigma}}}$. Then the direction is determined by what is known as a plastic potential function, $g(\bar{\boldsymbol{\sigma}})$. An associated flow rule is normally stated in general form as

$$\dot{\boldsymbol{\varepsilon}}_{\mathrm{p}} = \dot{\lambda} \frac{\partial f}{\partial \bar{\boldsymbol{\sigma}}}; \tag{5}$$

while a non-associated flow rule is defined as

$$\dot{\boldsymbol{\varepsilon}}_{\mathrm{p}} = \dot{\lambda} \frac{\partial g}{\partial \bar{\boldsymbol{\sigma}}}, \tag{6}$$

where $\dot{\lambda}$ is the rate of the plastic multiplier.

The main types of hardening are isotropic and kinematic. For isotropic hardening the yield surface expands uniformly, while kinematic hardening results in a rigid body movement in stress-space without volumetric change. Hardening can often be represented by a single parameter, especially for isotropic hardening.

3.3 Damage mechanics

Damage mechanics treats fracture of concrete mainly in tension, with the fundamental assumption that the localised damage in the material can be represented by damage variables. The simplest representation is by a scalar ω, which is attractive due to its simplicity and because it is easy to implement. A simple isotropic damage model is described by the basic equations:

$$\boldsymbol{\sigma} = (1 - \omega) \boldsymbol{D}_{\mathrm{e}} : \boldsymbol{\varepsilon} \tag{7}$$

$$\omega = g_{\mathrm{D}}(\kappa) \tag{8}$$

$$f_{\mathrm{D}} \leq 0 \quad \dot{\kappa} \geq 0 \quad \dot{\kappa} f_{\mathrm{D}} = 0 \tag{9}$$

where $\boldsymbol{\sigma}$ is the nominal stress tensor, ω is the damage parameter, κ is an internal softening variable that drives the damage, and f_{D} is the damage loading function.

The damage loading function describes the stress state when the micro-cracks are joining to a macro-crack; this corresponds to the state at peak-load on the envelope curve and is therefore closely related to physical properties. When the damage function is violated, κ increases and damage evolves.

Isotopic damage models are a simple way to describe a general multi-axial stress state. The stiffness degradation is assumed to be isotropic and dependent on a single scalar parameter ω. The damaged stiffness tensor (secant stiffness matrix) then becomes

$$\boldsymbol{D}_{\mathrm{s}} = (1-\omega)\boldsymbol{D}_{\mathrm{e}}. \tag{10}$$

To trigger the damage evolution, a loading function is introduced. The loading function is normally dependent on a history variable, κ, which is a physical representation of the maximum strain the material has experienced. As κ is a scalar measure, the multi-axial strain tensor, $\boldsymbol{\varepsilon}$, must be represented by a scalar measure of the strain level: normally, the equivalent strain, $\tilde{\varepsilon}$, is convenient as scalar measure. The loading function could then be described according to

$$f_{\mathrm{D}}(\boldsymbol{\varepsilon}, \kappa) = \tilde{\varepsilon}(\boldsymbol{\varepsilon}) - \kappa. \tag{11}$$

A standard type of definition of the equivalent strain is

$$\tilde{\varepsilon} = \sqrt{\boldsymbol{\varepsilon} : \boldsymbol{\varepsilon}}. \tag{12}$$

The evolution of damage, equation 8 is dependent on the applied strain and is represented by a function g_{D} which affects the softening branch of the stress-strain curve.

Instead of having the evolution of damage as a function of the current strain, it can be more convenient to use the history variable, $g_{\mathrm{D}}(\kappa)$. Then, it is possible to express the loading and unloading conditions in the Kuhn-Tucker form according to equation 9. Relating the first condition to the loading function (Equation 11) the meaning of the Kuhn-Tucker statement can be transcribed as $\kappa \geq \tilde{\varepsilon}$. The second condition is that κ cannot be reduced and the third is that κ only can increase if $f_{\mathrm{D}} = 0$.

Though isotropic damage models are often used to represent the failure of concrete, there are some typical known deficiencies.

- (Jirasek and Grassl, 2008) found, in their study of different kinds of damage models, that an isotropic damage model is strongly sensitive to the mesh orientation; it is therefore not suitable by itself for describing concrete failure in tension.
- Experimental observations of concrete in compression and shear show a volumetric expansion in post-peak response that is not captured. The lacking volumetric expansion results from a constant ratio between strain components in a proportional loading path in the stress space.
- For large deformation, the modelled material loses its stiffness in all directions.
- No irreversible strains are generated. Unloading takes place towards the origin.

Anisotropic damage models take into account the anisotropic state from which concrete suffers when loaded in one direction: the direction that suffers from greater stretching usually exhibits a larger degradation of stiffness. Generally, this is taken into account by a tensorial representation of damage, and the new anisotropic state is accounted for by changing the initial elastic stiffness to the damaged secant stiffness by an eight-order tensor. The formulation of a damage-evolution law which takes this into account becomes extremely difficult. Due to this increase in complexity, isotropic damage is used in the present study.

To describe the localisation of deformation, the crack band approach of (Bažant and Oh, 1983) is used for all analyses in this thesis. For the crack band approach, a crack band is introduced, which represents the width, L_s, of the actual fracture zone.

3.4 Coupling of plasticity and damage

The idea of coupling plasticity theory with damage mechanics seems promising at the outset. The volumetric expansion and the irreversible deformation seen in experiments are provided by the theory of plasticity, while the stiffness degradation is described by damage mechanics. This is investigated in Paper I which shows that a model based on plasticity in combination with damage is capable of describing curved crack patterns, previously described only by anisotropic models and plasticity models, due to the coupling between volumetric strains and deviatoric strains. Isotropic damage combined with ideal plasticity is defined as

$$\boldsymbol{\sigma} = (1-\omega) D_\mathrm{e} : (\boldsymbol{\varepsilon} - \boldsymbol{\varepsilon}_\mathrm{p}). \tag{13}$$

This configuration, which is used for the constitutive relations developed in Papers I, II and III, can be pictured as a serial combination of damage mechanics and plasticity, Figure 5.

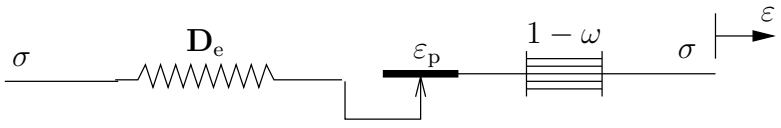

Figure 5: The serial configuration of damage and plasticity in combination.

In contrast, in Paper V the combination of plasticity and damage mechanics is parallel, Figure 6. The contribution of each part is controlled by a material parameter, α_{e}, The stress – strain relationship adopted in Paper V is

$$\boldsymbol{\sigma} = (1-\alpha_{\mathrm{e}})(1-\omega)\boldsymbol{D}_{\mathrm{e}} : \boldsymbol{\varepsilon} + \alpha_{\mathrm{e}}\boldsymbol{D}_{\mathrm{e}} : (\boldsymbol{\varepsilon} - \boldsymbol{\varepsilon}_{\mathrm{p}}). \tag{14}$$

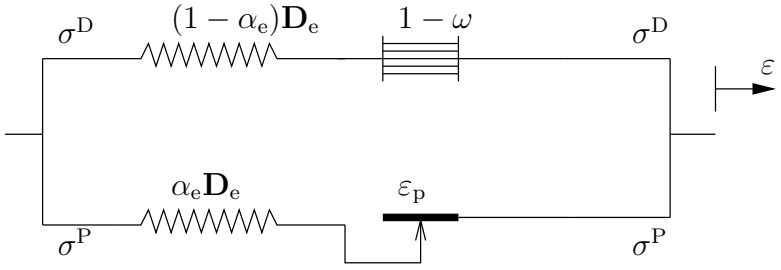

Figure 6: The parallel configuration of damage and plasticity in combination.

3.5 The concept of a bounding surface

Plasticity models constructed with two yield surfaces were introduced to describe the non-linear hardening behaviour for ductile solids with continuum models (Dafalias and Popov, 1975). Two-surface models were later renamed bounding surface models due to the enclosing nature of the bounding surface in regard to the yield surface; see Figure 7a. The purpose of bounding surface models is to describe the non-linear hardening and softening behaviour by prescribing the variation of the plastic modulus κ_{p}, i.e. as a way of describing strain hardening. The plastic modulus is determined by the relation, between the position of the actual plastic loading point and the bounding surface, as the distance δ. A general definition of δ is

$$\delta = \sqrt[2]{(\hat{\boldsymbol{\sigma}} - \bar{\boldsymbol{\sigma}})^2} \tag{15}$$

where $\hat{\boldsymbol{\sigma}}$ is the coordinates of the mirror point, point b or c in Figure 7, on the bounding surface, and $\bar{\boldsymbol{\sigma}}$ is the actual stress point. In Paper II, $\hat{\boldsymbol{\sigma}}$ is determined by the intersection of the normal to the yield surface and the bounding surface, (point b in Figure 7a). The computation of $\hat{\boldsymbol{\sigma}}$ is done by a function $\boldsymbol{M}$ called the mapping rule:

$$\hat{\boldsymbol{\sigma}} = \boldsymbol{M}(\bar{\sigma}, q_{\mathrm{n}}) \tag{16}$$

where q_n is an internal variable.

The bounding surface is constructed in the same way as a yielding surface; the bounding surface and the flow rule are generally described as

$$F = 0, \quad \dot{\hat{L}} = \dot{\hat{\lambda}} \frac{\partial F}{\partial \bar{\boldsymbol{\sigma}}}, \tag{17}$$

respectively, where $\dot{\hat{\lambda}}$ is the rate of the plastic multiplier. The identity condition, $\bar{\boldsymbol{\sigma}}$ on $F = 0$ so that $\bar{\boldsymbol{\sigma}} = \hat{\boldsymbol{\sigma}}$ and $\frac{\partial f}{\partial \bar{\boldsymbol{\sigma}}} = \frac{\partial F}{\partial \hat{\boldsymbol{\sigma}}}$, introduces restrictions on the relative evolution of the surfaces due to the fact that they can never intersect with each other.

In Figure 7 the enclosing concept of the bounding surface is shown:

- k and r are the centre points of the yield surface and the bounding surface, respectively; and
- c is the point where the normal to the bounding surface, $\boldsymbol{n}$, has the same direction as the normal to the yield surface, $\boldsymbol{w}$, for the actual plastic stress point, a.

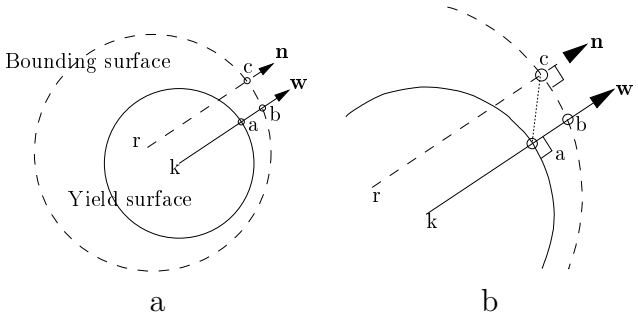

Figure 7: Bounding surface relation to the yield surface, (Suresh, 1998). There exist two ways to determine δ: as the distance from point a to c, or as the distance from a to b.

Bounding surface models make it possible for the plastic response to evolve according to the distance from the actual effective stress state, $\bar{\boldsymbol{\sigma}}$, to the bounding surface itself.

4 Modelling of concrete cyclic response

4.1 Meso-scale

4.1.1 Proposed meso-scale model

In the meso-scale study, Paper III, concrete is characterised by aggregates, mortar paste and interfacial zones that surround the aggregates. The aggregates are interpreted as stiff inclusions and are modelled as a linear elastic material, while the mortar and the interfacial zones are modelled by an interfacial model. The interfacial model is based on a combination of damage mechanics and the theory of plasticity.

The system of coordinates for the interface used in this study is defined by one normal and two tangential directions, i.e. the strain is defined as $\boldsymbol{\varepsilon} = (\varepsilon_{\mathrm{n}}, \varepsilon_{\mathrm{s}}, \varepsilon_{\mathrm{t}})$. The stress–strain relationship for this combination was defined above as

$$\boldsymbol{\sigma} = (1 - \omega)\boldsymbol{D}_{\mathrm{e}}(\boldsymbol{\varepsilon} - \boldsymbol{\varepsilon}_{\mathrm{p}}), \tag{18}$$

but the elastic stiffness was defined to fit the system of coordinates:

$$\boldsymbol{D}_{\mathrm{e}} = \begin{bmatrix} E & 0 & 0 \\ 0 & \gamma E & 0 \\ 0 & 0 & \gamma E \end{bmatrix}. \tag{19}$$

The interfacial model is characterised by a parameter, μ, which determines the ratio of plastic strain and total inelastic strain for tension, as well as compression; $\mu = 0$ corresponds to a pure damage mechanics response, while on the other hand, $\mu = 1$ corresponds to a pure plastic one. The responses for these two cases are shown in Figure 8. The points of unloading for tension and compression are marked by (A,A') and (B,B'), respectively. Note the linear unloading response.

4.1.2 Applications

In Paper III the interface model was applied to a plane stress analysis $\boldsymbol{\varepsilon} = (\varepsilon_{\mathrm{n}}, \varepsilon_{\mathrm{s}}, 0)$, see Figure 9, to investigate the effect of plastic deformations of the hysteresis loops. It is shown in the paper that more aggregates and a higher ratio of plastic strains yield a response with hysteresis loops such as those shown in Figure 10. As the interface model itself does not describe hysteresis loops, the hypothesis is stated that the cyclic response is due to a structural effect.

Paper IV continues this investigation with a parametric study of the mechanisms involved. The study deals with their effect on the hysteresis loops of aggregate density and size, the amount of irreversible displacements in the interfacial zones and the mortar, and the interfacial zones. To investigate these parameters, the same model was used as for the previous meso-scale study. The response and experimental observations are compared in Figure 11. It can be concluded from this study that the amount and strength of the interfacial zones contribute to the formation of hysteresis loops.

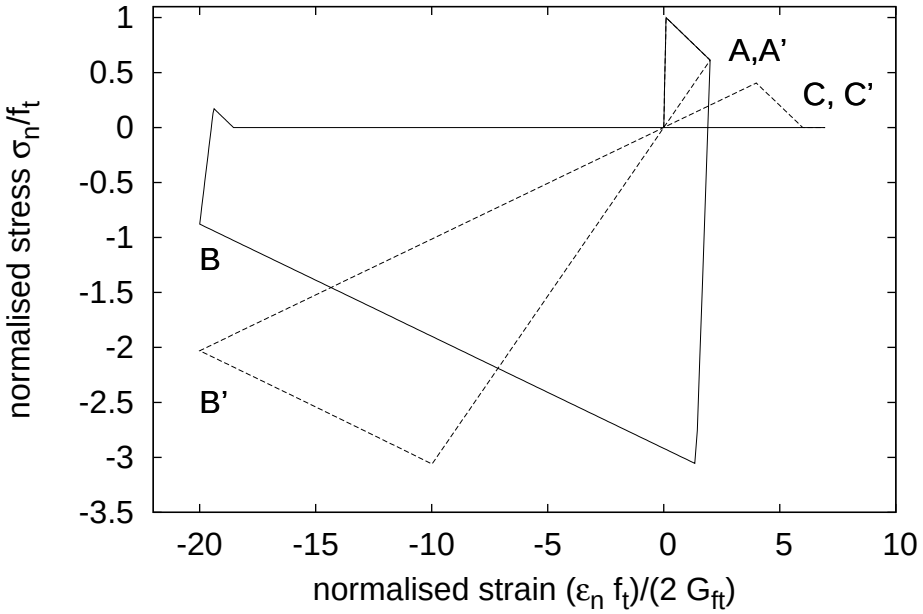

Figure 8: Stress–strain response for normal strain: $\mu = 1$ (solid line) and $\mu = 0$ (dashed line).

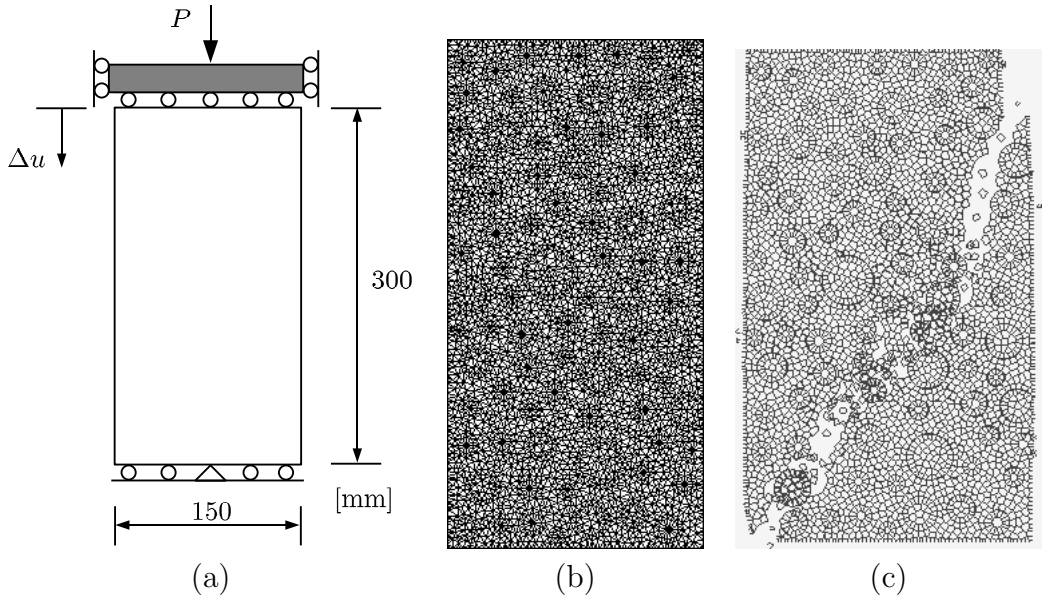

Figure 9: Plane stress application, Paper III. (a) Geometrical setup; (b) Mesh; and (c) Typical deformation pattern.

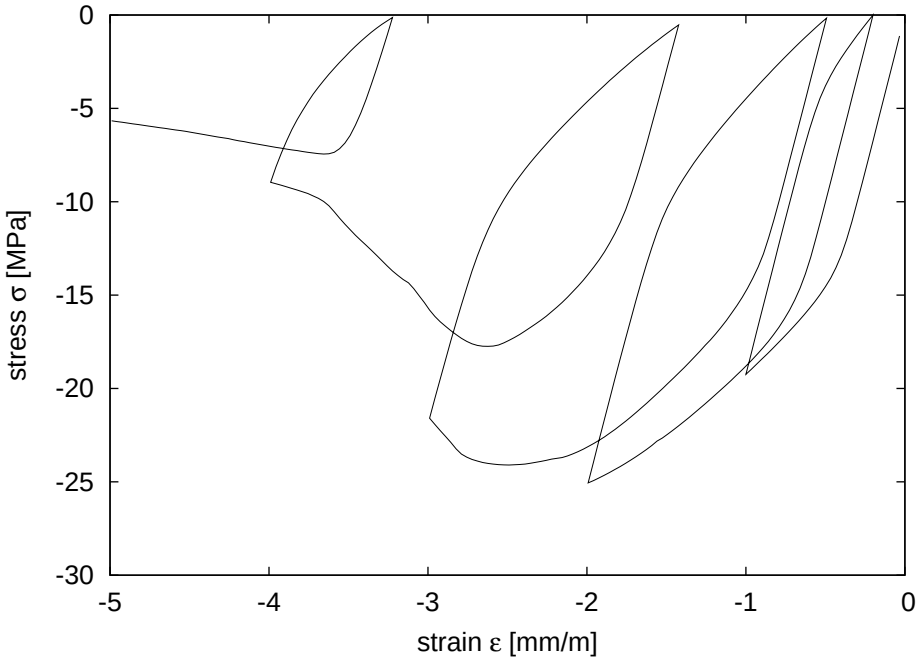

Figure 10: Response of plane stress problem, Paper III.

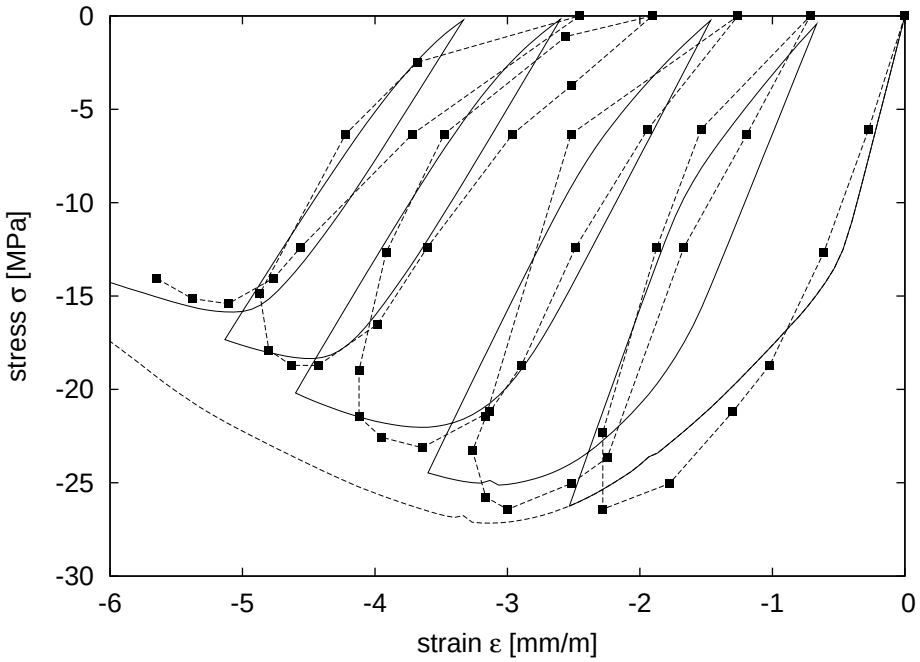

Figure 11: Stress–strain response obtained from the analysis compared with experimental results (dotted line).

4.2 Former macro-scale models

Four material models are presented in this chapter, selected from (Kessler-Kramer, 2002) according to how much they increase the accuracy of describing the response of concrete subjected to cyclic loading. A deeper analysis of these macro-models can be found in (Kessler-Kramer, 2002).

4.2.1 The Rots model

Rots developed and used a traditional damage model for post-peak cyclic loading of concrete in (Rots et al., 1985), see Figure 12. This model, in the sense of modelling of cyclic response, does not aim at describing the hysteresis loops. Nevertheless, the model responds to the closing and reopening of crack bands. Due to its simplicity, the response to cyclic loading is linear, and it does not account for the reduction of the unloading stiffness, nor for the development of plastic deformation. At the reopening of a crack the model returns to the monotonic envelope. Thus, no energy is released by cyclic loops, which is a consequence of the linear unloading-reloading response.

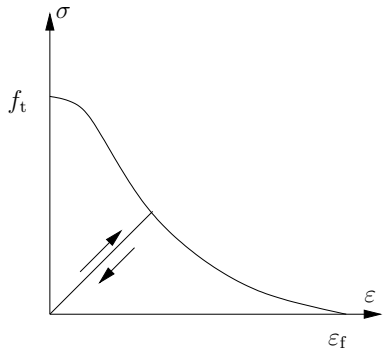

Figure 12: Illustration of the model by (Rots et al., 1985). ε_f is the final strain at which no stress can be transferred

4.2.2 The Gylltoft model

Before the Rots publication, (Gylltoft, 1983) developed a model which introduced the characteristics lacking in the Rots model. Gylltoft introduced an energy concept which was adopted in Paper II: hysteresis loops dissipate energy from the fracture energy. However, the model is limited to post-peak cyclic loading in tension and does not account for stiffness reduction due to damage generated during unloading and reloading on the constitutive level, see Figure 13. The modelling of the cyclic response is based on three material parameters, g_0, g_c, and ε_f, which control the sliding of crack surfaces. This sliding is, according to Gylltoft, different for unloading and reloading. Although the stiffness is the same, this concept yields a hysteresis loop that dissipates energy from the softening branch.

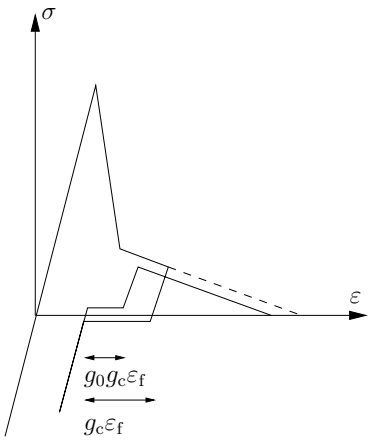

Figure 13: Illustration of the model by (Gylltoft, 1983)

4.2.3 The Hordijk model

With an increasing level of complexity, the race for a realistic description of the cyclic response in tension is made by (Reinhardt et al., 1986; Yankelevsky and Reinhardt, 1987b,a, 1989). This chain of development ends with the Continuous-Function-Model by (Hordijk, 1991). Hordijk strongly states (page 85) that the energy approach by Gylltoft is a misunderstanding in the interpretation of experimental observation; this discussion has continued since then. The energy approach by Gylltoft, adopted in this thesis, is among other characteristics of cyclic response, investigated in Papers III and IV. The results of that work support the approach by Gylltoft. The Continuous-Function-Model consists of a set of continuous functions that are based on characteristic points in the stress–strain response. Apart from the softening expression, the Continuous-Function-Model also includes expressions for: I, the unloading curve; II, the gap in the envelope curve; and III, the reloading curve. The response is shown in Figure 14.

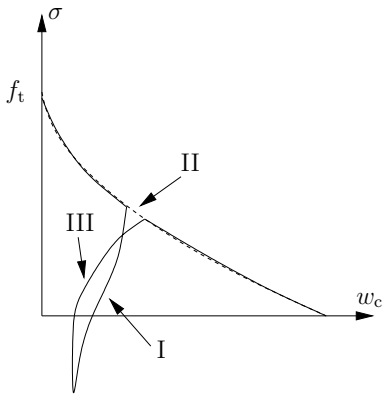

Figure 14: Illustration of the model by (Hordijk, 1991)

4.2.4 The Ožbolt and Bažant model

(Ožbolt and Bažant, 1992) inserted rules in the microplane model by (Bažant and Prat, 1988) to model unloading, reloading and cyclic loading. Their results show a capacity to describe the response of concrete subjected to cyclic loading in shear, compression and tension. In addition, data is presented for a fluctuating load. However, the plastic deformation at unloading is not accounted for correctly, which makes the model unsuitable for this kind of loading.

4.3 Macro-scale

4.3.1 Proposed macro-scale models

Three macro models were formulated and implemented in this thesis. The macro model of Paper I, rather than aiming to describe cyclic loading, was used to investigate the effect of coupling between deviatoric plastic strain and volumetric plastic strain. The model was formulated as a serial combination of damage mechanics and the theory of plasticity, which yields the possibility to control this coupling.

The first approach to a macro model of concrete subjected to cyclic loading in this thesis, Paper II, uses the model of Paper I as a basis (Figure 5, page 12). Paper II aims to describe cyclic loading of concrete in tension by means of the bounding surface concept. To introduce the concept of a bounding surface is, in fact, to define a hardening law based on surfaces that bound different states of stress. The plastic part of the model is described by two such surfaces: one elastic bounding surface that limits the elastic domain (i.e. inside this domain the response is linear elastic). On the edge of the elastic domain, the material starts to yield. Thus, the elastic bounding surface is the same as a yield surface. As soon as yielding starts, the stress point is repelled by the second bounding surface which bounds all admissible states of stress. The repelled stress state finds a new position of the elastic domain, and plastic strain develops. This continues until the outer bounding surface is reached; thus, the actual stress point is positioned on both surfaces. From this position, all strains that develop are plastic ones. At this point damage is initiated.

The damage is determined by an isotropic damage variable which is driven by the developed plastic strain when the two bounding surfaces are in contact. The damage variable decreases the outer bounding surface such that the admissible stress domain is reduced with increased damage. If the deformation is reversed at this stage, the state of stress leaves the surfaces; the response consequently becomes elastic until the border of the elastic domain is reached at a different position. Again, when the state of stress is at the elastic bounding surface, yielding is initiated and the stress point is repelled by the outer bounding surface.

As an illustration, the process described above can be pictured as a point of stress inside two rings that define the bounding surfaces. The inner ring can move inside the outer ring in the direction of the movement. The outer ring repels the movement of the inner ring which yields plastic strains.

The second approach to a macro-model was, instead of a serial combination of damage mechanics and the theory of plasticity, a parallel combination (Figure 6, page 13). The theory of this model is given in Paper V. The fundamental part of the formulation of the parallel combination is the variable, α_e, which controls the contribution of each part to the stiffness according to

$$\boldsymbol{\sigma} = (1-\alpha_e)(1-\omega)\boldsymbol{D}_e\boldsymbol{\varepsilon} + \alpha_e\boldsymbol{D}_e(\boldsymbol{\varepsilon}-\boldsymbol{\varepsilon}_p). \tag{20}$$

The total nominal stress is thus achieved by adding the nominal stress of the sub-parts which are evaluated separately. The basic idea was that the damage part should give the overall response, while the plastic part gives the cyclic response. The formulation reveals a need for a softening of both parts, as no damage is added to the plastic part.

The plastic part of the formulation is based on two yield surfaces defined by stress invariants: one outer and one inner yield surface. The outer one is based on the Ottosen yield surface; the inner one is of the von Mises type. In the hydrostatic stress space, this results in a curved outer yield surface while the inner yield surface is a line parallel to the hydrostatic axis. However, in the deviatoric stress space, both yield surfaces are circular (Figure 15). The fact that the inner yield surface is circular in the deviatoric section causes a numerical problem, as the surface must be concave to yield a solution. To solve this, the inner yield surface is not active until the stress state is inside the space enclosed by the inner yield surface. This is achieved by computing the value of the distortional energy. When the distortional energy is negative, the inner yield surface can be activated and remains so as long as the distortional energy is negative. In Paper V, this is revealed to correspond to the part of the unloading with low stress and stiffness.

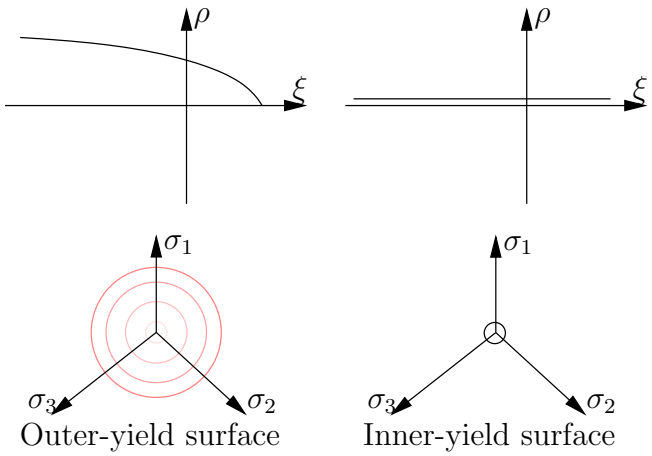

Figure 15: Illustration of the outer and inner-yield surfaces. Above, the volumetric stress space (Haigh-Westergaard coordinates) is given and below the deviatoric stress space.

4.3.2 Applications

The macro model for mainly monotonic loading in Paper I is applied in an analysis of two well known experiments: the four-point shear test made by (Arrea and Ingraffea, 1982) and a double-edge notched test made by (Nooru-Mohamed, 1992). These two tests assess the capability of the material model to describe the response of a curved crack pattern. In Figure 16 the responses of the analyses are shown for the tests with the crack pattern observed during the experiment and for two examples of coupling between volumetric and deviatoric inelastic strains. It is shown in Paper I that this coupling is essential for describing a complex crack pattern. Paper I discusses this coupling which is provided

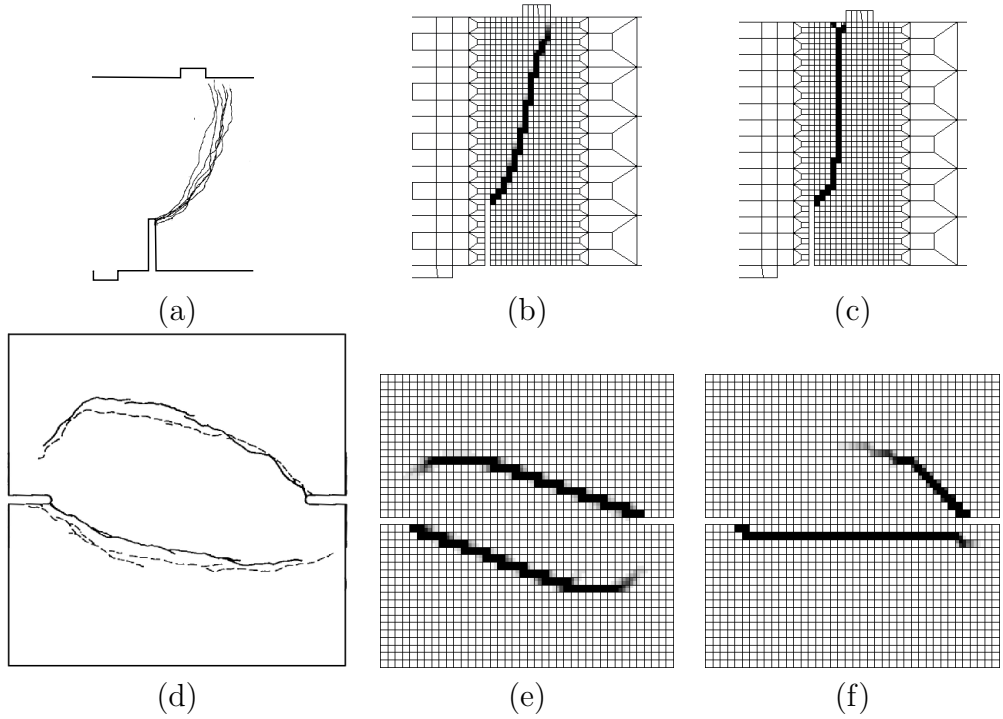

Figure 16: Results from analysis of a four-point shear test and a double-edged notched test in Paper I. (a) Crack pattern of four point shear test; (b) $H_{\mathrm{p}} = 0$; (c) $H_{\mathrm{p}} = 100E$; (d) Crack pattern of double-edged notched test; (e) $H_{\mathrm{p}} = 0$; (f) $H_{\mathrm{p}} = 100E$.

through the hardening modulus in the tangent stiffness matrix: the shear components of the plastic part of the tangent stiffness matrix are non-zero for finite values of H_{p}. Thereby, a shear strain results not only in shear stresses but also in normal stresses. Since the total strain in the analyses is constrained, plastic strains arise which generate compressive stresses. The compressive stresses generated increase the maximum shear stress and the volume fracture energy. Thus, as the strain localises in zones close to the state of uni-axial tension, rather than in the confined zones that are subjected to shear, the crack paths become curved.

The macro models based on the bounding surface concept (Paper II) and the dual-model (Paper V) were validated with a test, from (Gopalaratnam and Shah, 1985), which is a

direct tension test of concrete subjected to cyclic loading. The specimen of the direct tension test is rectangular (305 x 76 mm) with a thickness of 19 mm and notched at the sides. The notches are 3 mm wide and 13 mm deep. To control the loading process clip gauges are placed at the notches, together with extensiometers by a length of 83 mm placed over the notched section which are used for reporting the result. The deformation is applied at the edges by friction hooks. These hooks can rotate in the plane of the specimen, as well as out of the plane. The experimental setup is presented in Figure 17.

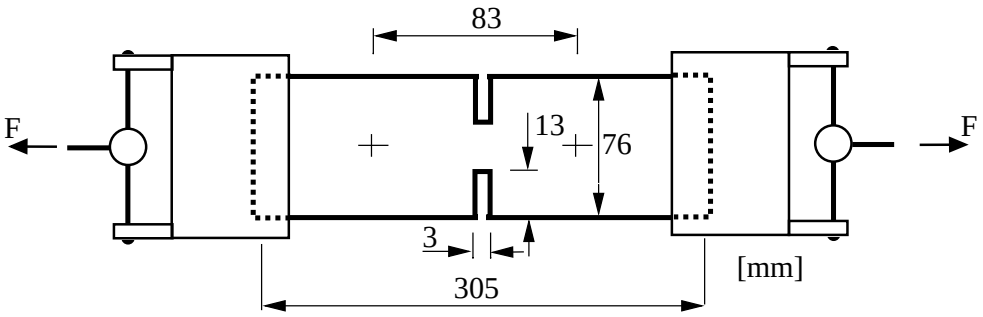

Figure 17: Experimental setup of the direct tension test. Thickness of specimen is 19 mm, (Gopalaratnam and Shah, 1985).

The mesh and configuration of the analysis made by the bounding surface model is presented in Paper II. The result from that analysis is compared with the experimental response in Figure 18. From the analysis, it is shown that the hysteresis loops are well described, but it is also revealed that the stiffness reduction due to increase of damage is not captured. This deficiency is a result of the localisation model chosen, which results in mesh dependent unloading and reloading stiffness. To the author's knowledge, this has not been reported previously.

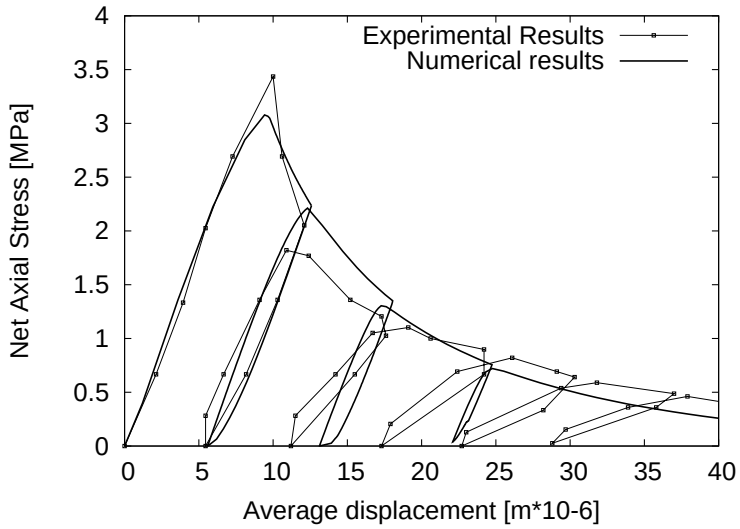

Figure 18: Result from an analysis of concrete subjected to direct tension, Paper II.

The dual-model is studied on the constitutive level in Paper V (Figure 6, page 13). The parameters studied, which are important for the cyclic response, are α_e and W^D. The influence of α_e on the size of the hysteresis loops is shown. It is demonstrated that when the influence of the plastic part is made greater, it generates larger hysteresis loops (Figure 19d). The results also show the correspondence between a negative distortional energy and the development of plastic deformation during unloading, Figure 19a-c. This correspondence reveals the neatness of using the negative distortional energy to control the state of plastic deformation at unloading.

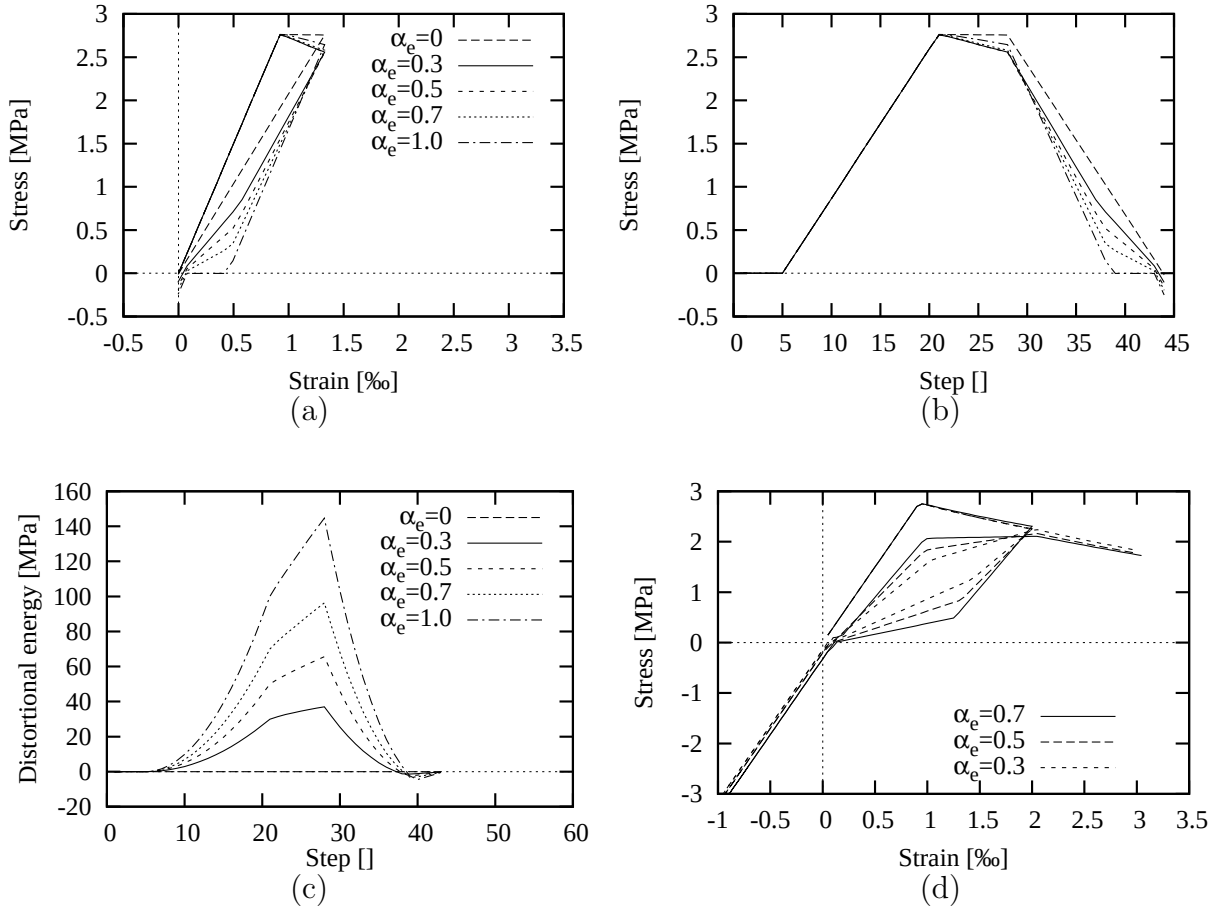

Figure 19: Analyses without lateral confinement for: $\alpha_e = 0$, $\alpha_e = 0.3$, $\alpha_e = 0.5$, $\alpha_e = 0.7$, and $\alpha_e = 1.0$. (a) Stress-strain response; (b) evolution of the stress; (c) behaviour of the distortional energy W^D; and (d) response of an uniaxial deformation with $\alpha_e = 0.7$, $\alpha_e = 0.5$ and $\alpha_e = 0.3$.

For the analyses of the direct tension test made by the dual-model the meshes consists of tetrahedra four-node finite elements. As a direct tension test is complex, due to the symmetry and instability of the experimental procedure (Figure 17), the analyses were made from two different setups of mesh: one setup of a quarter of the bar and one of the full bar. To reduce the symmetry problem the full bar was analysed with one notch only.

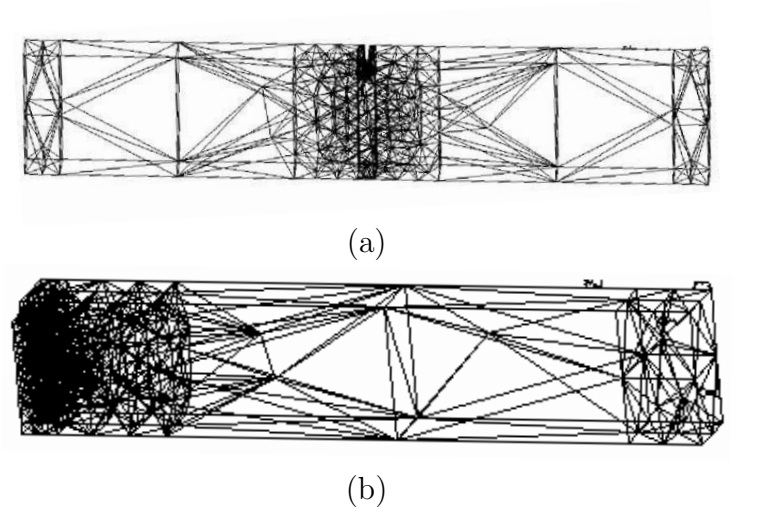

(a)

(b)

Figure 20: (a) Mesh of the full bar analysis and (b) mesh of quarter of bar analysis.

The real response should be between these two approaches. The meshes of the direct tension setups are shown in Figure 20 and the chosen material parameters for the model are presented in Table 1. The fracture energy was adjusted in the analyses to account for the different crack widths.

Table 1: Material parameters chosen for the analyses of the direct tension test by (Gopalaratnam and Shah, 1985)

E	ν	ε_0	ε_f	H
30 MN/m^2	0.18	$9.5e^{-6}$	$1.0e^{-3}$	$0.1E$

C_1	α_ψ	τ_0	$f_\mathrm{y}^\emptyset$
0.50	0.01	5 MN/m^2	1 kN/m^2

The load of the direct tension test was applied by controlling the displacement at the notch opening in both approaches. The load was applied at the end of the bar.

Boundary condition of the direct tension test of the full bar (Figure 21a).

- To avoid displacement in the direction of the thickness of the bar, one side of the mesh was locked in the direction normal to the corresponding side.
- At one of the edges with friction hook, the bar was locked at its position in the direction of the normal to the face. The faces at the edges were able to rotate so that the edge sections remain plane.
- The bar was fixed for global rotation and kinematic movement.

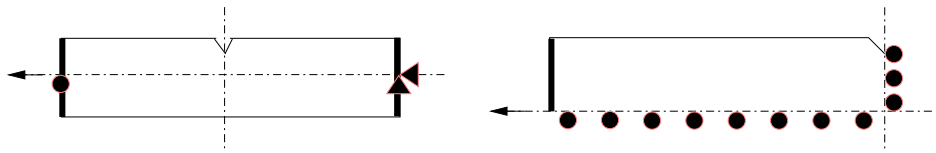

(a) (b)

Figure 21: (a) Boundary conditions of the full bar and (b) boundary conditions of the quarter of a bar.

Boundary condition of the direct tension test of the quarter of a bar (Figure 21b).

- The specimen was locked at one side in the direction of its thickness.
- At the lines of symmetry of the full bar, the quarter was locked in the direction of the normal to the face.
- The bar was fixed for global rotation and kinematic movement.

Next, the result of cyclic loading is given. As supposed, for the full bar and the quarter, the pure damage analysis give an unloading towards origo. While, the pure plastic case results in an unloading stiffness close to the initial elastic stiffness. The hysteresis loops of both approaches are to some extent smaller than in the experiment.

Comparing the cyclic response (Figure 22c and d), the unloading stiffness is more correctly described for the full bar. On the other hand, the size of the hysteresis loop is more correct represented for the quarter of the bar.

An interesting discussion is how the plastic deformation would develop in the crack (micro-crack) during a cycle. In Figures 23 and 24, for the analyses made by the dual-model, the evolution of the volumetric and deviatoric parts of the plastic strain and the total strain is given. For the outer-yield surface a non-associated flow rule was chosen; the chosen configuration results in an evolution of volumetric and deviatoric plastic strains. Depending on the chosen plastic potential the relation between the volumetric and deviatoric parts differ. The interesting part of the question is how these would develop at unloading, i.e. crack closure. The plastic potential of the inner-yield surface was chosen so that no volumetric plastic strain develops during unloading. This is given in Figures 23a and 24a; at unloading, as the plastic volumetric strain remains constant, the elastic part of the volumetric strain is negative. Hence, a state of compression is reached. On the contrary, the deviatoric plastic strain develops alongside the total strain (Figures 23b and 24b). The latter could be interpreted as sliding of irregular crack surfaces, while the first case could be interpreted as volumetric closing of the crack. The development of the deviatoric plastic strain (sliding of crack surfaces) seems to be a good interpretation of the reality. However, the development of the volumetric plastic strain is not that easy to determine. If the crack only opens and closes this may be a good approximation, but the development would probably be different if the crack could not close due to irregularities at the crack surfaces.

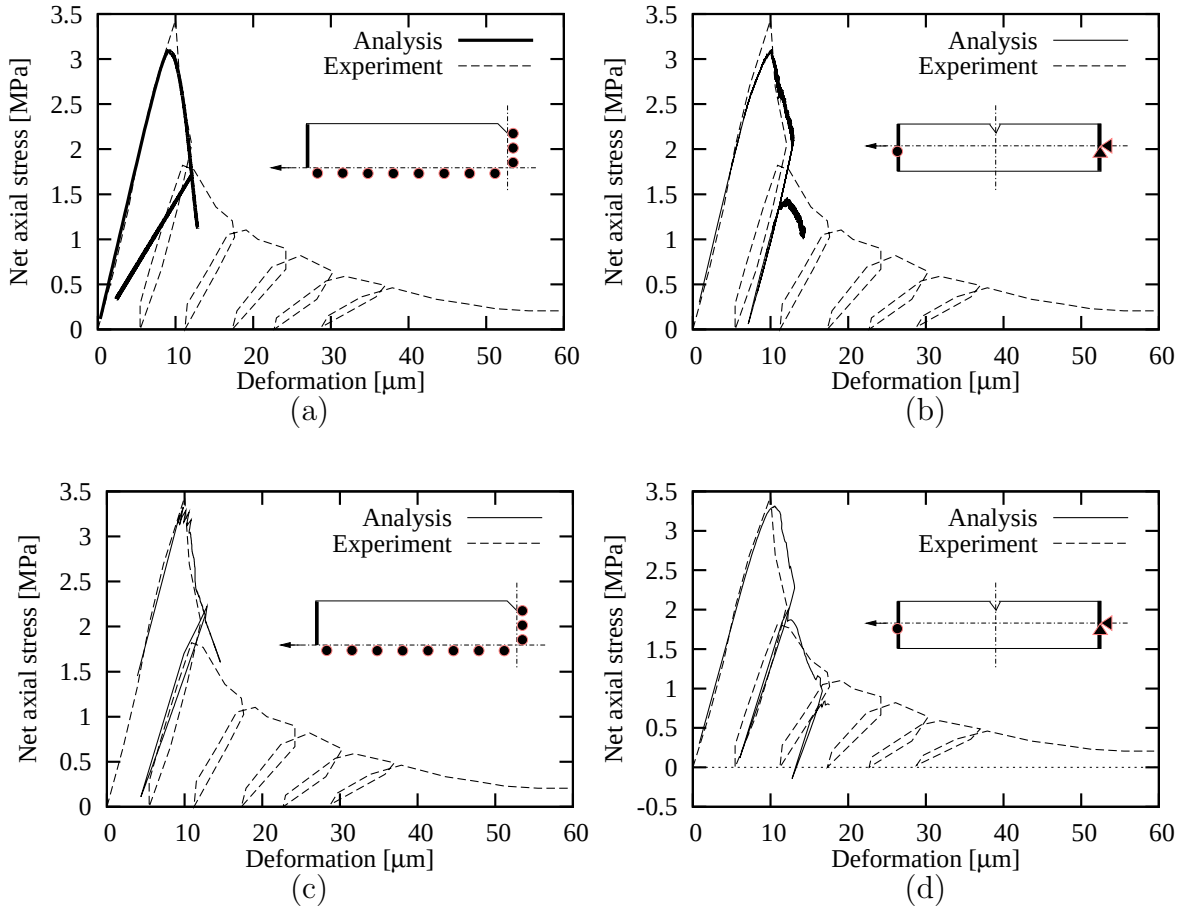

Figure 22: Cyclic loaded analyses of direct tension test with different values of α_e. (a) $\alpha_e = 0$ (Quarter of a bar), (b) $\alpha_e = 1$ (Full sized bar), (c) $\alpha_e = 0.3$ (Quarter of a bar), and (d) $\alpha_e = 0.3$ (Full sized bar).

The relative size of the evolution indicates, for the chosen configuration of the dual-model, that the evolution of deviatoric plastic deformation is greater than the volumetric. In the investigation at meso-scale (Paper III and IV), this is indicated as well. In conclusion, the investigations indicate that the volumetric part of the plastic deformation at unloading most likely influences the response.

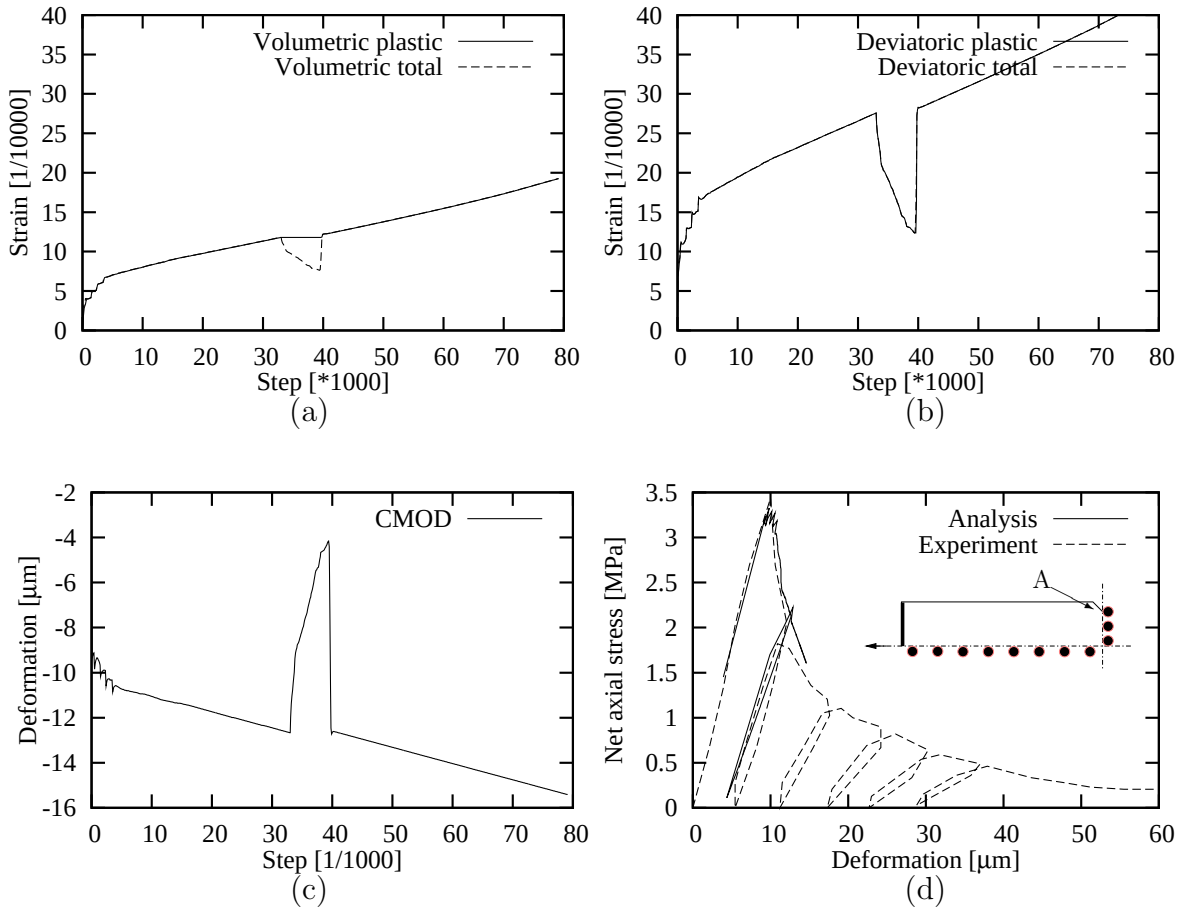

Figure 23: For the quarter of a bar analysis: (a) volumetric plastic strain – step, (b) deviatoric plastic strain – step, (c) crack mouth opening displacement (CMOD) in the direction of the load, and (d) load – deformation response (A is the location of the studied element).

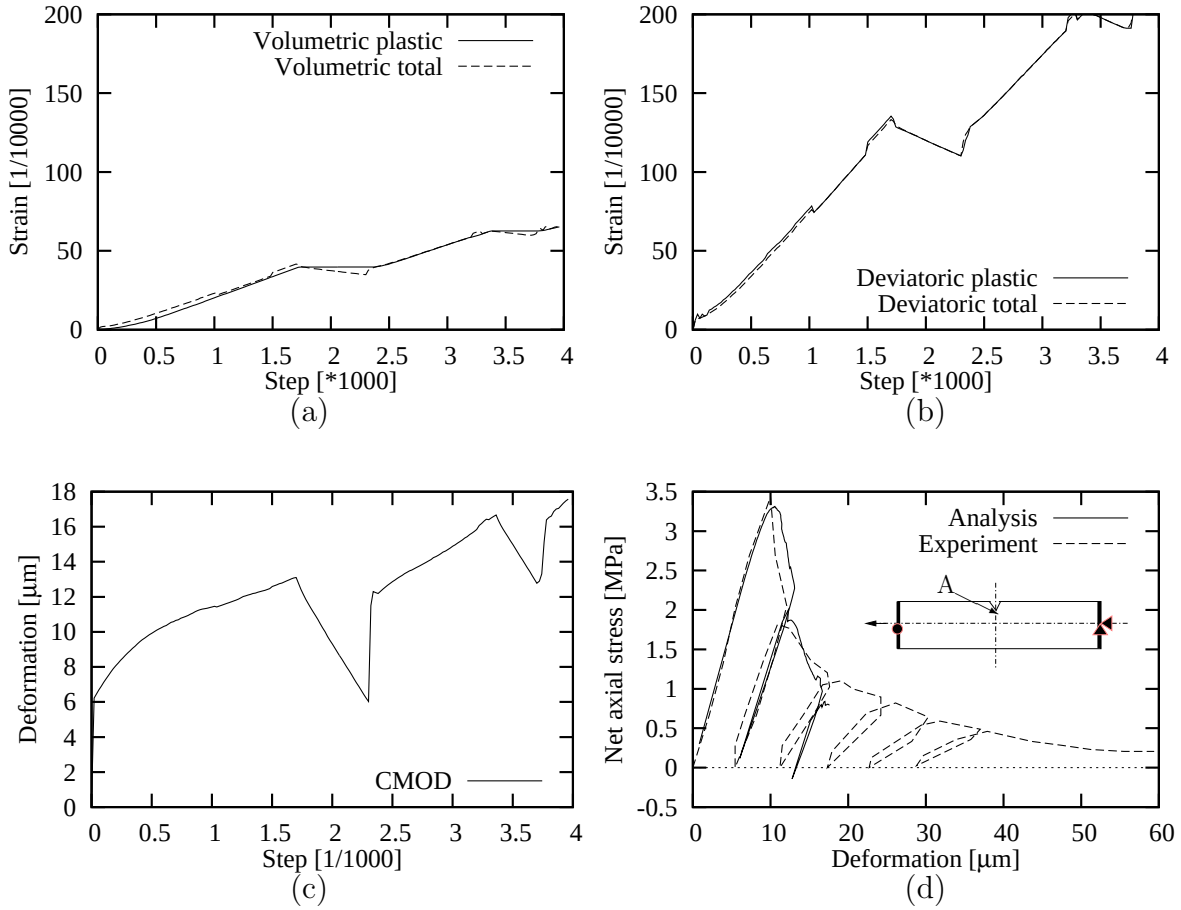

Figure 24: For the full bar analysis: (a) volumetric plastic strain – step, (b) deviatoric plastic strain – step, (c) crack mouth opening displacement (CMOD) in the direction of the load, and (d) load – deformation response (A is the location of the studied element).

This page intentionally contains only this sentence.

5 Conclusions

5.1 General conclusions

The present work aims to describe and deepen understanding of the phenomenon of cyclic loading of concrete. The main theories used for this are those of plasticity and damage mechanics. These theories have proved to be useful for describing concrete subjected to cyclic loading. However, some disadvantages were revealed. In the following these pros and cons are stated.

The theory of plasticity is suitable for describing cyclic loading because the strain can be divided into elastic and inelastic parts. This division makes it possible to describe the increase of plastic deformation, at the localisation of deformation, as well as the observed response of unloading which exhibits low stress and stiffness. The plastic strain is also essential for describing the hysteresis loops of pre and post-peak cyclic loading in tension and compression. However, the theory of plasticity fails to describe the stiffness reduction caused by an increasing number of cycles and damage.

Fortunately, damage mechanics is suitable for describing the stiffness reduction with increasing damage. As long as the damage is evaluated as isotropic, the procedure of computing the damage is efficient. However, damage mechanics alone is not sufficient to describe the response of concrete subjected to cyclic loading.

Hence, a combination of these theories is a tempting approach. In this thesis two combinations are introduced and applied to concrete structures subjected to cyclic loading. The combinations are somewhat modified to fit the two scales of observation and aim of study, but they are intended to preserve the advantages of their essence.

In the appended papers the following conclusions are drawn.

- Constitutive models with volumetric-deviatoric coupling provide higher shear resistance in simple shear than models without coupling. The increase in shear stress is caused by the activation of compressive stresses due to constrained strains.

- In the simulation of curved cracks, the paths of localised strain zones are strongly influenced by the amount of volumetric-deviatoric coupling. Only with volumetric-deviatoric coupling can the curved crack patterns be reproduced, as has not been shown before.

- The bounding surface model describes the cyclic response well, except for the stiffness reduction due to increased numbers of cycles and consequent damage. The deficiency in describing the stiffness reduction was traced back to the chosen localisation model.

- The meso-scale approach with the new interface model results in realistic failure patterns in the form of shear bands. The amount of localised permanent displacement has a strong influence on the material response for repeated loading. With localised

permanent displacement, the stress–strain curves are characterised by hysteresis loops and damage evolves during repeated loading.

- At meso-scale, five parameters were investigated. Their influence on the cyclic response is summarised here.
  - A decrease in the volume fraction of aggregates increases the ultimate strength of concrete, since a smaller proportion of aggregates corresponds to a reduction of interfacial transition zones which weaken the material. The decrease also reduces the size of the hysteresis loops, due to fewer interfacial transition zones. Localised permanent displacements are the main reason for describing hysteresis loops.
  - The size range of aggregates does not strongly influence the response of concrete subjected to monotonic and cyclic loading.
  - Less permanent displacement in the interfacial transition zones results in a reduction of the size of the hysteresis loops.
  - A decrease of the number of permanent displacements in the mortar phase results in a reduction of the size of the loops in the post-peak regime, which is where localised permanent displacements occur in the mortar phase.
  - The strength of the mortar and the interfacial transition zones have a strong influence on both the monotonic and cyclic responses. An increase of the strength of the interfacial zones leads to an increase of the compressive strength, since the permanent displacements in the interfacial zones are reduced.
  - Furthermore, the size of the hysteresis loops is described.
- The proposed material parameter, α_e, influences the size of the hysteresis loops in a direct fashion, making the model easy to calibrate.
- The distortional energy is related to the plastic deformation at unloading. During plastic unloading the distortional energy is negative, which makes it useful as a parameter for controlling this state.

5.2 Suggestions for future research

In finite element analyses of concrete subjected to cyclic loading, the computer time is an important issue, especially for high cycle fatigue analyses in compression. If a variable that can predict the fatigue life without going through the whole number of cycles can be found, the computer time needed could be reduced. The distortional energy used as a parameter for the unloading process of cyclic loading, in Paper V, could be such a variable; as the negative value of the distortional energy decreases with every cycle that generates plastic deformation at unloading, it could be convenient to determine the total value of negative distortional energy to calculate fatigue life. If the prediction of fatigue life could be made less time consuming, then high cycle fatigue could be better investigated.

The investigation in Paper V initiated a discussion about the lateral behaviour of a micro-cracked zone. The complete understanding of this would add to the description of the cyclic response.

This work focuses on concrete. However, the reality is reinforced concrete structures. Therefore, the natural step after this study is to investigate the cyclic behaviour of such structures. Another thing that has caught the author's attention is the fact that today the fatigue life of a structure relies totally on the reinforcement. An interesting investigation would be to examine how the concrete can contribute to the fatigue life of a structure and, thereby, relieve the reinforcement by reduced stress. The benefit would be the reduced amount of reinforcement needed, for which the cost today is high.

This page intentionally contains only this sentence.

References

Åkesson, M. (1996). *Implementation and Application of Fracture Mechanics models for concrete structures.*, Doctoral thesis, Chalmers University of Technology, Division of Concrete Structures, Göteborg, Sweden, pp. 159.

Abu-Lebdeh, T. and Voyiadjis, G. (1993). Plasticity-Damage Model for Concrete under Cyclic Multiaxial Loading, *Journal of Engineering Mechanics-ASCE*, Vol. 119, No. 7, pp. 1465–1484.

Arrea, M. and Ingraffea, A. (1982). *Mixed-mode Crack Propagation in Mortar and Concrete*, Master's thesis, Department of Structural Engineering, Cornell University, Ithaca, NY, pp. 142.

Aurenhammer, F. (1991). Voronoi Diagrams - A survey of a fundamental geomtric data structure, *ACM Computing Surveys*, Vol. 23, pp. 345–405.

Baluch, M., Qureshy, A. and Azad, A. (1987). Fatigue crack propagation in plain concrete, *Fracture of Concrete and Rock: SEM-RILEM International Conference*, Soc for Experimental Mechanics Inc, Bethel, CT, USA, Houston, TX, USA, pp. 112–119.

Bažant, Z. and Prat, P. (1988). Microplane model for brittle-plastic material – Parts I and II, *Journal of Engineering Mechanics*, Vol. 114, No. 10, pp. 1672–1702.

Bažant, Z. and Shieh, C. (1980). Hysteretic Fracturing Endochronic Theory for Concrete, *Journal of the Engineering Mechanics Division-ASCE*, Vol. 106, No. 5, pp. 929–950.

Bažant, Z. P. and Oh, B. H. (1983). Crack band theory for fracture of concrete, *Materiaux et Constructions*, Vol. 16, No. 93, pp. 155–177.

Bolander, J. E., Hong, G. S. and Yoshitake, K. (2000). Structural concrete analysis using rigid-body-spring networks, *J. Comp. Aided Civil and Infrastructure Engng.*, Vol. 15, pp. 120–133.

Bolander, J. E. and Saito, S. (1998). Fracture analysis using spring networks with random geometry, *Engineering Fracture Mechanics*, Vol. 61, pp. 569–591.

Bolander, J. E. and Sukumar, N. (2005). Irregular lattice model for quasistatic crack propagation, *Physical Review B*, Vol. 71, No. 9, pp. 12.

Budiansky, B. and O'Connell, R. (1976). Elastic moduli of a cracked solid, *Int J Solid Struct*, Vol. 12, No. 2, pp. 81–97.

Buyukozturk, O. and Teng, T. (1984). Concrete in biaxial cyclic compression, *Journal of Structural Engineering*, Vol. 110, No. 3, pp. 461–476.

Carpinteri, A., Cornetti, P. and Puzzi, S. (2004). A stereological analysis of aggregate grading and size effect on concrete tensile strength, *International Journal of Fracture*, Vol. 128, No. 1–4, pp. 233–242.

CEB (1988). *Fatigue of Concrete Structures, State of the Art Report*, Tech. Rep. 188, Comité Euro-International du Béton, pp. 300.

Cendón, D., Gálvez, J., Elices, M. and Planas, J. (2000). Modelling the fracture of concrete under mixed loading, *International Journal of Fracture*, Vol. 103, No. 3, pp. 293–310.

Clemmer, H. (1922). Fatigue of concrete, *Proceedings of the American Society for Testing Materials*, 2, pp. 408–419.

Cornelissen, H. A., Hordijk, D. and Reinhardt, H. (1986). Experimental determination of crack softening characteristics of normalweight and lightweight concrete, *Heron*, Vol. 31, No. 2, pp. 45–56.

Crepps, R. (1923). Fatigue of mortar, *Proceedings of the American Society for Testing Materials*, 2, pp. 329–340.

Dafalias, Y. and Popov, E. (1975). Model of Nonlinearly Hardening Materials for Complex Loading, *Acta Mechanica*, Vol. 21, No. 3, pp. 173–192.

Dafalias, Y. F. (1986). Bounding surface plasticity. I: Mathematical foundation and hypoplasticity, *Journal of Engineering Mechanics*, Vol. 112, No. 9, pp. 966–987.

Desmorat, R., Ragueneau, F. and Pham, H. (2007). Continuum damage mechanics for hysterisis and fatigue of quasi-brittle materials and structures, *International Journal for Analytical and Numerical Methods in Geomechanics*, Vol. 31, No. 2, pp. 307–329.

Prisco, di , M., Ferrara, L., Meftah, F., Pamin, J., Borst, de , R., Mazars, J. and Reynouard, J. (2000). Mixed mode fracture in plain and reinforced concrete: some results on benchmark tests, *International Journal of Fracture*, Vol. 103, pp. 127–148.

Dormieux, L., Kondo, D. and Ulm, F. (2006). *Microporomechanics*, Wiley.

Einav, I., Houlsby, G. and Nguyen, G. (2007). Coupled damage and plasticity models derived from energy and dissipation potentials, *International Journal of Solids and Structures*, Vol. 44, No. 7-8, pp. 2487–2508.

Elfgren, L. and Gylltoft, K. (1992). *Utmattningshållfasthet hos betongkonstruktioner*, Tech. rep., Avdelningen för konstruktionsteknik, Tekniska Högskolan i Luleå, Luleå, Sverige, pp. 42.

Galvez, J., Elices, M., Guinea, G. and Planas, J. (1998). Mixed mode fracture of concrete under proportional and nonproportional loading, *International Journal of Fracture*, Vol. 94, No. 3, pp. 267–284.

Gao, Z.-H. and Zhang, X.-Q. (1987). Investigation of complete stress-deformation curves for concrete in tension, *ACI Material Journal*, Vol. 84, No. 4, pp. 278–285.

Gau, L. and Hsu, C. (1998). Fatigue of concrete under uniaxial compression cyclic loading, *ACI Mater J*, Vol. 95, No. 5, pp. 575–581.

Geers, M., Borst, de , R. and Peerlings, R. (2000). Damage and Crack modeling in single-edge and double-edge notched concrete beams, *Engineering Fracture Mechanics*, Vol. 65, pp. 247–261.

Gettu, R. and Aguado, A. (1996). Damage in high-strength concrete due to monotonic and cyclic compression – A study based on splitting tensile strength, *ACI Materials Journal*, Vol. 93, No. 6, pp. 519–523.

Gopalaratnam, V. and Shah, S. (1985). Softening response of plain concrete in direct tension, *Journal of the American Concrete Institute*, Vol. 82, No. 3, pp. 310–323.

Grassl, P. and Jirásek, M. (2004). On mesh biase of local damage models for concrete, Li, V., Leung, C., Willam, K. and Billington, S., eds., *Fracture Mechanics of Concrete Structures*, pp. 323–337.

Grassl, P. and Jirásek, M. (2006). Damage-plastic model for concrete failure, *International Journal of Solids and Structures*, Vol. 43, No. 22–23, pp. 7166–7196.

Grassl, P. and Rempling, R. (2007). Influence of volumetric-deviatoric coupling on crack prediction in concrete fracture tests, *Engineering Fracture Mechanics*, Vol. 74, No. 10, pp. 1683–1693.

Grassl, P. and Rempling, R. (2008). A damage-plasticity interface approach to meso-scale modelling of heterogeneous materials subjected to cyclic loading, *Engineering Fracture Mechanics*, Vol. 75, No. 16, pp. 4804–4818.

Griffiths, D. and Mustoe, G. (2001). Modelling of elastic continua using a grillage of structural elements based on discrete element concepts, *International Journal for Numerical Methods in Engineering*, Vol. 50, No. 7, pp. 1759–1775.

Gustafsson, P. J. (1985). *Fracture Mechanics Studies of Non-Yielding Materials like Concrete : Modelling of Tensile Fracture and Applied Strength Analyses*, Doctoral thesis, Lund University of Technology, Lund, Sweden, pp. 430.

Gylltoft, K. (1983). *Fracture Mechanics Models for Fatigue in Concrete structures.*, Doctoral thesis 1983:25d, Luleå University of Technology, Luleå, Sweden, pp. 210.

Hai-cheng, L., Wei, C. and Yu-pu, S. (2004). Fatigue properties of plain concrete under triaxial compressive cyclic loading, *China Ocean Engineering*, Vol. 18, No. 3, pp. 457–468.

Han, T., Ural, A., Chen, C., Zehnder, A., Ingraffea, A. and Billington, S. (2002). Delamination buckling and propagation analysis of honeycomb panels using a cohesive element approach, *International Journal of Fracture*, Vol. 115, pp. 101–123.

Heukamp, F., Lemarchand, E. and Ulm, F. (2005). The effect of interfacial properties on the cohesion of highly filled composite materials, *Int J Solid Struct*, Vol. 42, No. 1, pp. 287–305.

Holmberg, G. (2001). *Fatigue of Concrete Piles of High Strength Concrete Exposed to Impact Load*, Licentiate thesis, Chalmers University of Technology, Department of Structural Engineering, Göteborg, Sweden, pp. 71.

Holmen, J. (1979). *Fatigue of Concrete by Constant and Variable Amplitude Loading*, Doctoral thesis, The Norwegian Institute of Technology, Trondheim, Norway, pp. 218.

Hordijk, D. (1991). *Local Approach to Fatigue of Concrete*, Doctoral thesis, Technische universiteit te Delft, Delft, The Netherlands, pp. 210.

Hordijk, D. and Reinhardt, H. (1993). Numerical and Experimental Investigation into the Fatigue Behavior of Plain Concrete, *Experimental Mechanics*, Vol. 33, No. 4, pp. 278–285.

Imran, I. (1994). *Applications of Non-Associated Plasticity in Modelling the Mechanical Response of Concrete*, Doctoral thesis, Univerity of Toronto, Department of Civil Engineering, Toronto, Canada, pp. 208.

Jason, L., Huerta, A., Pijaudier-Cabot, G. and Ghavamian, S. (2006). An elastic plastic damage formulation for concrete: Application to elementary tests and comparison with an isotropic damage model, *Computer Methods in Applied Mechanics and Engineering*, Vol. 195, No. 52, pp. 7077–7092.

Jason, L., Pijaudier-Cabot, G., Huerta, A., Crouch, R. and Ghavamian, S. (2004). An elastic plastic damage formulation for the behavior of concrete, Li, V., Leung, C., Willam, K. and Billington, S., eds., *Fracture mechanics of concrete structures*, pp. 549–556.

Jirásek, M. and Bažant, Z. P. (1995). Particle model for quasibrittle fracture and application to sea ice, *Journal of Engineering Mechanics, ASCE*, Vol. 121, pp. 1016–1025.

Jirasek, M. and Bažant, Z. P. (2001). *Inelastic analysis of structures*, John Wiley and Sons, pp. 734, 1 ed.

Jirasek, M. and Grassl, P. (2008). Evaluation of directional mesh bias in concrete fracture simulations using continum damage models, *Engineering Fracture Mechanics*, Vol. 75, No. 8, pp. 1921–1943.

Johansson, U. (2004). *Fatigue Tests and Analysis of Reinforced Concrete Bridge Deck Models*, Licentiate thesis, Royal Institute of Technology, Stockholm, Sweden, pp. 198.

Karsan, I. and Jirsa, J. (1969). Behaviour of concrete under compressive loadings, *Journal of Structural Division-ASCE*, Vol. 95, pp. 2543–2563.

Kawai, T. (1977). New element models in discrete structural analysis, *J Soc Naval Arch Jpn*, Vol. 141, pp. 187–193.

Kessler-Kramer, C. (2002). *Zugtragverhalten von Beton Unter Ermüdungsbeanspruchung*, Ph.D. thesis, Universität Fridericiana zu Karlsruhe, Karlsruhe, Deutschland, pp. 261.

Larsson, R. (1990). *Numerical Simulation of Plastic Localization*, Doctoral thesis, Chalmers University of Technology, Göteborg, Sweden, pp. 94.

Laurenco, P. B. and Rots, J. G. (1997). Multisurface interface model for analysis of masonry structures, *Journal of Engineering Mechanics, ASCE*, Vol. 123, pp. 660–668.

Lee, H. and Kim, Y. (1998). Viscoelastic constitutive modeling for asphalt concrete under cyclic loading, *Journal of Engineering Mechanics-ASCE*, Vol. 124, No. 2, pp. 32–40.

Lee, J. and Fenves, G. (1998). Plastic-damage model for cyclic loading of concrete structures, *Journal of Engineering Mechanics-ASCE*, Vol. 124, No. 8, pp. 892–900.

Lee, M. and Barr, B. (2004). An overview of the fatigue behaviour of plain concrete and fibre reinforced concrete, *Cement Concrete Composites*, Vol. 26, No. 4, pp. 299–305.

Lee, Y. and Willam, K. (1997). Mechanical properties of concrete in uniaxial compression, *ACI Materials Journal*, Vol. 94, No. 6, pp. 457–471.

Lilliu, G. and Mier, J., van (2003). 3D lattice type fracture model for concrete, *Engineering Fracture Mechanics*, Vol. 70, pp. 927–941.

Mier, J., van (1984). *Strain-softening of Concrete Under Multiaxial Loading Conditions*, Doctoral thesis, Technische Hogeschool Eindhoven, Eindhoven, The Netherlands, pp. 248.

Mier, J., van (1986). Fracture of concrete under complex stress, *HERON*, Vol. 31, No. 3, pp. 89.

Mier, J., van (2007). Multi-scale interaction potentials (F- r) for describing fracture of brittle disordered materials like cement and concrete, *International Journal of Fracture*, Vol. 143, No. 1, pp. 41–78.

Morikawa, O., Sawamota, Y. and Kobayashi, N. (1993). Local fracture analysis of a reinforced concrete slab by the discrete element method, Press, M., ed., *Proceedings of the 2nd International Conf. on Discrete element methods*, pp. 275–286, cambridge, MA, USA.

Murdock, J. (1965). A critical review of research on fatigue of plain concrete, *Univeristy of Illinois College of Engineering, Engineering experiment station*, Vol. 62, No. 62.

Murdock, J. and Kesler, C. (1958). Effect of range of stress on fatigue strength of plain concrete beams, *ACI Journal*, pp. 221–231.

Nooru-Mohamed, M. (1992). *Mixed-mode Fracture of Concrete: An Experimental Approach*, Ph.D. thesis, Delft University of Technology, Delft, The Netherlands.

Ortiz, M. and Pandolfi, A. (1999). Finite-deformation irreversible cohesive elements for three-dimensional crack-propagation analysis, *International Journal for Numerical Methods in Engineering*, Vol. 44, pp. 1267–1282.

Ottosen, N. S. (1977). A failure criterion for concrete, *Journal of Engineering Mechanics, ASCE*, Vol. 103, pp. 527–535.

Ožbolt, J. and Bažant, Z. (1992). Microplane model for cyclic triaxial behavior of concrete, *Journal of Engineering Mechanics*, Vol. 118, No. 7, pp. 1365–1386.

Ožbolt, J. and Reinhardt, H. (2002). Numerical study of mixed-mode fracture in concrete, *International Journal of Fracture*, Vol. 118, pp. 145–161.

Pandolfi, A., Krysl, P. and Ortiz, M. (1999). Finite element simulation of ring expansion and fragmentation: The capturing of length and time scales through cohesive models of fracture, *International Journal of Fracture*, Vol. 95, pp. 279–297.

Pandolfi, A. and Talercio, A. (1998). Bounding surface models applied to fatigue of plain concrete, *Journal of engineering Mechanics*, Vol. 124, pp. 556–564.

Papa, E. and Taliercio, A. (1996). Anisotropic damage model for the multiaxial static and fatigue behaviour of plain concrete, *Engineering Fracture Mechanics*, Vol. 55, pp. 163–179.

Patzák, B. (1999). Object oriented finite element modeling, *Acta Polytechnica*, Vol. 39, pp. 99–113.

Patzák, B. and Bittnar, Z. (2001). Design of object oriented finite element code, *Advances in Engineering Software*, Vol. 32, pp. 759–767.

Patzák, B. and Jirásek, M. (2003). Adaptive resolution of localized damage in quasibrittle materials, *Journal of Engineering Mechanics, ASCE*, Vol. 130, pp. 720–732.

Petkovic, G. (1991). *Properties of Concrete Related to Fatigue Damage with Emphasis in High Strength Concrete*, Doctoral thesis, Univeristetet i Trondheim, Norges Tekniske Hogskole, Trondheim, Norway, pp. 217.

Pivonka, P., Ožbolt, J., Lackner, R. and Mang, H. (2004). Comparative studies of 3D-constitutive models for concrete: application to mixed-mode fracture, *International Journal for Numerical Methods in Engineering*, Vol. 60, pp. 549–570.

Plizzari, G., Cangiano, S. and Alleruzzo, S. (1997). The fatigue behaviour of cracked concrete, *Fatigue and Fracture of Engineering Materials and Structures*, Vol. 20, No. 8, pp. 1195–1206.

Prado, E. and Mier, J., van (2007). Effect of particle structure on mode I fracture process in concrete, *Engineering Fracture Mechanics*, Vol. 70, pp. 927–941.

Ragueneau, F., Borderie, C. L. and Mazars, J. (2000). Damage model for concrete-like materials coupling cracking and friction, contribution towards structural damping: first uniaxial applications, *Mechanics of Cohesive-Frictional Materials*, Vol. 5, pp. 607–625.

Reinhardt, H. (1984). Fracture mechanics of an elastic softening material like concrete, *Heron*, Vol. 29, No. 2, pp. 42.

Reinhardt, H. W., Cornelissen, H. A. W. and Hordijk, D. A. (1986). Tensile tests and failure analysis of concrete., *Journal of Structural Engineering*, Vol. 112, No. 11, pp. 2462–2477.

Rempling, R. and Grassl, P. (2008). A parametric study of the meso-scale modelling of concrete subjected to cyclic compression, *Computers and Concrete*, Vol. 5, No. 4, pp. 359–373.

Rots, J., Nauta, P., Kusters, G. and Blaauwendraad, J. (1985). Smeared crack approach and fracture localization in concrete, *Heron*, Vol. 30, No. 1.

Schlangen, E. (1993). *Experimental and Numerical Analysis of Fracture Processes in Concrete*, Doctoral thesis, Delft University of Technology, Delft, The Netherlands.

Schlangen, E. and Garboczi, E. J. (1996). New method for simulating fracture using an elastically uniform random geometry lattice, *International Journal of Engineering Science*, Vol. 34, No. 10, pp. 1131–1144.

Schlangen, E. and Mier, J., van (1992). Simple lattice model for numerical simulation of fracture of concrete materials and structures, *Materials and Structures*, Vol. 25, pp. 534–542.

Shewchuk, J. R. (1996). Triangle: Engineering a 2D Quality Mesh Generator and Delaunay Triangulator, Lin, M. C. and Manocha, D., eds., *Applied Computational Geometry: Towards Geometric Engineering*, Vol. 1148 of *Lecture Notes in Computer Science*, Springer-Verlag, pp. 203–222, from the First ACM Workshop on Applied Computational Geometry.

Simo, J. and Ju, J. (1987). Strain-Based and Stress-Based Continuum Damage Models 1. Formulation, *International Journal of Solids And Structures*, Vol. 23, No. 7, pp. 821–840.

Sinha, B. and Gerstle, L., K.and Tulin (1964). Stress-strain relations for concrete under cyclic loading, *American Concrete Institute – Journal*, Vol. 61, No. 2, pp. 195.

Spooner, D. and Dougill, J. (1975). Quantitative Assessment of Damage Sustained in Concrete During Compressive Loading, *Magazine of Concrete Research*, Vol. 27, No. 92, pp. 151–160.

Spooner, D., Pomeroy, C. and Dougill, J. (1976). Damage and Energy-Dissipation in Cement Pastes in Compression, *Magazine of Concrete Research*, Vol. 28, No. 94, pp. 21–29.

Subramaniam, K., Popovics, J. and Shah, S. (1999). Fatigue response of concrete subjected to biaxial stresses in the compression-tension region, *ACI Materials Journal*, Vol. 96, No. 6, pp. 663–669.

Suresh, S. (1998). *Fatigue of materials*, Cambridge University Press, Cambridge, United Kingdom, pp. 102–114, 2nd ed.

Svahn, P.-O. (2005). *Dynamic Behaviour of Reinforced Concrete Structures: Analyses with a strong discontinuity approach*, Doctoral thesis, Chalmers University of Technology, Department of Structural Engineering, Göteborg, Sweden, pp. 46.

Tepfers, R. (1978). *En undersökning av betongens utmattningshållfashet*, Tech. Rep. R86:1978, Avdelningen för husbyggnadsteknik, Chalmers University of Technology, Göteborg, Sweden, pp. 121.

Tepfers, R. (1979). Tensile Fatigue Strength of Plain Concrete, *Journal of the ACI*, pp. 919–933.

Tepfers, R. (1980a). Fatigue of plain concrete subjected to stress reversals, *Contribution to ACI Symposium at 1980 Fall Convention*, SP 75-9, American Concrete Institute, San Juan, Puerto Rico, pp. 195–215.

Tepfers, R. (1980b). Tensile Fatigue Strength of Plain Concrete, *Journal of the ACI*, pp. 203–205, discussion.

Tepfers, R. and Kutti, T. (1979). Fatigue Strength of Plain, Ordinary and Lightweight Concrete, *Journal of the ACI*, pp. 635–652.

Thelandersson, S. (1974). *Characteristics of Fire Exposure and Consequenses on Mechanical Behavior of Concrete.*, Doctoral thesis, Lund University of Technology, Lund, Sweden, pp. 13.

Thelandersson, S. (1987). Modeling of combined thermal and mechanical action in concrete, *Journal of engineering mechanics-ASCE*, Vol. 113, No. 6, pp. 893–906.

Thun, H. (2006). *Assessment of Fatigue Resistance and Strength in Existing Concrete Structures*, Doctoral thesis, Luleå University of Technology, Luleå, Sweden, pp. 48.

Ueda, T., Sato, Y., Kakuta, Y. and Tadokoro, T. (1998). A study on crack propagation in concrete under cyclic loading, *AEDIFICATIO Publishers, Fracture Mechanics of Concrete Structures,*, Vol. 1, pp. 655–663.

Voyiadjis, G. and Abulebdeh, T. (1994). Plasticity Model for Concrete Using the Bounding Surface Concept, *International Journal of Plasticity*, Vol. 10, No. 1, pp. 1–21.

Voyiadjis, G. Z. and Abulebdeh, T. M. (1993). Damage Model for Concrete Using Bounding Surface Concept, *Journal of Engineering Mechanics-ASCE*, Vol. 119, No. 9, pp. 1865–1885.

Willam, K., Hansen, E. and Kang, H. (2001). Performance evaluation of damage and plasticity formulations for concrete, Shing, P. and Tanabe, T., eds., *Modeling of inelastic behavior of rc structures under seismic load*, American Society of Civil Engineers, pp. 1–19.

Willam, K., Rhee, I. and Shing, B. (2004). Interface damage model for thermomechanical degradation of heterogeneous materials, *Computer Methods in Applied Mechanics and Engineering*, Vol. 193, No. 30–32, pp. 3327–3350.

Winnicki, A. and Cichon, C. (1998). Plastic model for concrete in plane stress state. i.: Theory, *Journal of Engineering Mechanics*, Vol. 124, pp. 591–602.

Yang, B., Dafalias, Y. F. and Herrmann, L. R. (1985). Bounding surface plasticity model for concrete, *Journal of Engineering Mechanics*, Vol. 111, No. 3, pp. 359.

Yankelevsky, D. and Reinhardt, H. (1987a). Response of plain concrete to cyclic tension, *ACI Materials Journal*, Vol. 84, pp. 365–373.

Yankelevsky, D. and Reinhardt, H. (1989). Uniaxial behaviour of concrete in cyclic tension, *ASCE Journal of Structural Engineering*, Vol. 115, No. 1, pp. 166–182.

Yankelevsky, D. Z. and Reinhardt, H. W. (1987b). Model for cyclic compressive behaviour of concrete, *ASCE Journal of structural engineering*, Vol. 113, No. 2, pp. 228–240.

Zubelewicz, A. and Bažant, Z. (1987). Interface modeling of fracture in aggregate composites, *J Engng Mech - ASCE*, Vol. 113, pp. 1619–1630.

This page intentionally contains only this sentence.

Grassl, P.; Rempling, R. (2007).
Influence of volumetric-deviatoric coupling on crack prediction in concrete fracture tests.
Engineering Fracture Mechanics. 74 (10) pp. 1683–1693.

This page intentionally contains only this sentence.

Available online at www.sciencedirect.com
ScienceDirect
Engineering Fracture Mechanics 74 (2007) 1683–1693
Engineering Fracture Mechanics
www.elsevier.com/locate/engfracmech

Influence of volumetric–deviatoric coupling on crack prediction in concrete fracture tests

P. Grassl [a], R. Rempling [b,*]

[a] University of Glasgow, Department of Civil Engineering, G12 8LT Glasgow, United Kingdom
[b] Chalmers University of Technology, Department of Structural Engineering and Mechanics, 41296 Göteborg, Sweden

Received 5 January 2005; received in revised form 2 June 2006; accepted 18 August 2006
Available online 1 November 2006

Abstract

The influence of volumetric–deviatoric coupling on the prediction of curved crack patterns in concrete fracture tests is analyzed by using an elasto-plastic-damage model, for which the amount of volumetric–deviatoric coupling is controlled by the hardening modulus of the plasticity model. First, the tangent stiffness matrix and the total stress–strain response for simple shear are investigated. Then, two fracture tests reported in the literature are simulated with significantly varying amounts of coupling. It is shown that volumetric–deviatoric coupling greatly improves the description of curved crack patterns in mixed-mode fracture tests.

Keywords: Plasticity; Damage mechanics; Concrete; Mixed-mode concrete fracture; Volumetric–deviatoric coupling

1. Introduction

Constitutive models based on damage mechanics, plasticity and combinations of both are often used to describe the fracture process of quasi-brittle materials, such as concrete, rock, tough ceramics or ice. In these materials, fracture is characterized by the development of nonlinear fracture process zones, which can be described macroscopically as regions of highly localized strains. The performance of constitutive models for concrete is often evaluated by analyzing fracture tests with curved crack patterns [1–4]. The results of such analysis have been reported in [5–11]. Anisotropic damage models have proved to be capable of reproducing many of the often complex crack patterns, as reported in [8] and [10]. Isotropic damage models, on the contrary, often fail to describe realistically the crack patterns of these mixed-mode fracture tests. Anisotropic damage models differ from isotropic ones in, among other things, that they provide volumetric–deviatoric coupling, i.e. in a simple shear test, the shear strain generates not only a shear stress, but also compressive normal stresses. Simple shear is defined as a state with three-dimensional constant volume strain. Willam et al. [12]

* Corresponding author. Tel.: +46 31 7722212; fax: +46 31 7722260.
E-mail address: rasmus.rempling@chalmers.se (R. Rempling).

0013-7944/$ - see front matter © 2006 Elsevier Ltd. All rights reserved.
doi:10.1016/j.engfracmech.2006.08.028

Nomenclature

$\mathbf{D}_e$	isotropic elast ic stiffness tensor
$\mathbf{D}_{epd}$	elasto-plastic-damage stiffness tensor
E	Youngs modulus
G_f	fracture energy
H_p	plastic hardening modulus
P	Applied force
P_s	Applied shear force
R_d	plastic part of the elasto-plastic-damage stiffness tensor
R_p	damage part of the elasto-plastic-damage stiffness tensor
f_t	tensile strength
n_1	normalized eigenvector
$\boldsymbol{\varepsilon}$	total strain
ε_f	model parameter
$\boldsymbol{\varepsilon}_p$	plastic strain
η	Poisson's ratio
κ_p	plastic hardening parameter
$\dot{\lambda}$	rate of plastic multiplier
σ	nominal stress
$\bar{\sigma}$	effective stress
$\bar{\sigma}_1$	maximum principal value of effective stress
σ_y	yield stress
ω	isotropic damage scalar

have studied the volumetric–deviatoric coupling on the constitutive level for various plasticity models with regard to loss of stability and uniqueness.

In the present paper the influence of the volumetric–deviatoric interaction on the modeling of curved crack patterns in mixed-mode fracture tests is investigated. This is accomplished by using an isotropic elasto-plastic-damage model, which permits one to vary the amount of volumetric–deviatoric interaction by controlling the hardening law of the plasticity model. It is expected that this interaction is the key to an accurate description of curved crack patterns observed in several fracture tests of plain concrete. This has not been shown before to the knowledge of the authors. Thus, this study contains novel features, which help to understand the performance of modeling techniques for concrete subjected to complex combinations of loading.

The fracture tests mentioned are often analyzed by assuming plane stress. Consequently, a modified simple shear state is examined, where the condition of constant volume strain is limited to the in-plane strain components, and the out-of-plane component is determined from the condition of zero stress in this direction.

The basic equations of the elasto-plastic-damage model are stated and the volumetric–deviatoric interaction is illustrated with the elasto-plastic-damage tangent stiffness matrix for the onset of inelastic behavior in simple shear. Next, the total stress–strain response for this state is analyzed with the model for four different degrees of interaction. Finally, two fracture tests with curved crack patterns, reported in the literature, are analyzed with significantly varying amounts of volumetric–deviatoric coupling.

2. The plasticity-damage model

The model consists of an elasto-plasticity part combined with isotropic damage that is determined by the cumulative plastic strain. For the combined elasto-plastic-damage model, the stress–strain relation is given as

$$\boldsymbol{\sigma} = (1-\omega)\bar{\boldsymbol{\sigma}} = (1-\omega)\mathbf{D}_e : (\boldsymbol{\varepsilon} - \boldsymbol{\varepsilon}_p) \tag{1}$$

where $\boldsymbol{\sigma}$ is the nominal stress, ω is the scalar describing the amount of isotropic damage, $\bar{\boldsymbol{\sigma}}$ is the effective stress, $\mathbf{D}_e$ is the isotropic elastic stiffness, $\boldsymbol{\varepsilon}$ is the total strain and $\boldsymbol{\varepsilon}_p$ is the plastic strain.

2.1. Basic equations

The plasticity model, which is formulated on the assumption of small strains, is based on the effective stress, $\bar{\boldsymbol{\sigma}}$, and consists of the yield function, the flow rule, the evolution law for the hardening variable and the loading–unloading conditions. For plane stress:

$$f_p(\bar{\boldsymbol{\sigma}}, \kappa_p) = \bar{\sigma}_1 - \sigma_y(\kappa_p) = \bar{\sigma}_1 - (f_t + H_p\kappa_p) \tag{2}$$

describes the Rankine yield function, where $\bar{\sigma}_1$ is the maximum principal value of the effective stress tensor $\bar{\boldsymbol{\sigma}}$, σ_y is the yield stress, f_t is the tensile strength, H_p is the plastic hardening modulus and κ_p is the plastic hardening parameter. Plastic yielding is initiated when the maximum principal effective stress reaches the yield stress σ_y. For equibiaxial tension, when both principal values are equal to the yield stress, the value of the second principal stress also influences the yielding process. Only one active surface is dealt with here, since the behavior is studied in biaxial tension and compression, see Fig. 1a.
For the structural analysis in Section 4, however, the case of two active yield surfaces for equibiaxial tension is included.

For one active surface, the flow rule is given as

$$\dot{\boldsymbol{\varepsilon}}_p = \dot{\lambda}\frac{\partial f_p}{\partial \bar{\boldsymbol{\sigma}}} = \dot{\lambda}\frac{\partial \bar{\sigma}_1}{\partial \bar{\boldsymbol{\sigma}}} = \dot{\lambda}\mathbf{n}_1 \otimes \mathbf{n}_1 \tag{3}$$

where $\mathbf{n}_1$ is the normalized eigenvector corresponding to the first principal eigenvalue of the effective stress tensor, $\otimes$ denotes the dyadic product of two vectors, and $\dot{\lambda}$ is the rate of the plastic multiplier.

The evolution of the hardening parameter, κ_p, is given by the norm of the plastic strain rate,

$$\dot{\kappa}_p = \|\dot{\boldsymbol{\varepsilon}}_p\| = \dot{\lambda} \tag{4}$$

Loading–unloading conditions complete the description of the plasticity part:

$$f_p \leqslant 0, \quad \dot{\lambda} \geqslant 0, \quad \dot{\lambda} f_p = 0 \tag{5}$$

The damage variable, ω, is related to the plastic hardening parameter, κ_p, by

$$\omega = g_d(\kappa_p) = 1 - \frac{f_t \exp(-\kappa_p/\varepsilon_f)}{f_t + \kappa_p H_p} \tag{6}$$

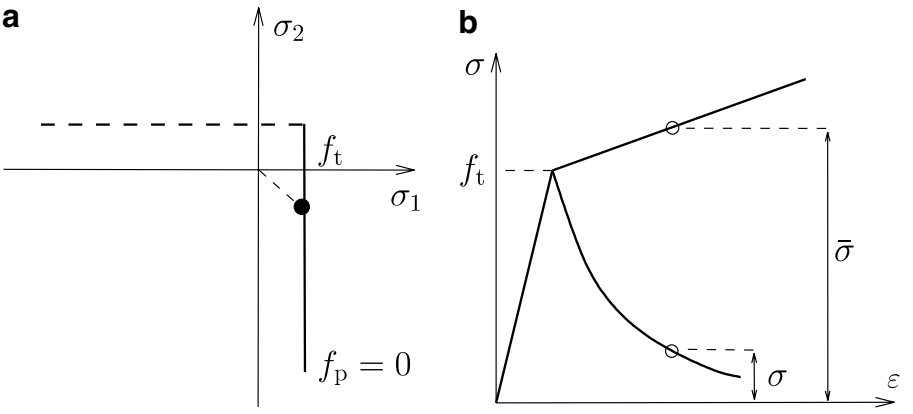

Fig. 1. (a) Schematic drawing of the Rankine yield surface at the onset of yielding for pure shear. (b) Schematic drawing of the stress–strain and effective stress–strain curve for uniaxial tension.

which results in an exponential total stress–strain curve, see Fig. 1b. The model parameter, ε_f, controls the area under the stress–strain curve and can be related to the fracture energy G_f. There is no plastic process without damage evolution, since it is directly linked to the plastic process.

2.2. The tangent stiffness matrix

The tangent stiffness is studied to gain information on the form of the volumetric–deviatoric coupling, which is introduced by the plastic-damage model. The rate form of the general stress–strain relation in Eq. (1) is

$$\dot{\boldsymbol{\sigma}} = (1-\omega)\dot{\bar{\boldsymbol{\sigma}}} - \dot{\omega}\bar{\boldsymbol{\sigma}} = (1-\omega)\mathbf{D}_e : \left(\dot{\boldsymbol{\varepsilon}} - \dot{\lambda}\frac{\partial \bar{\sigma}_1}{\partial \bar{\boldsymbol{\sigma}}}\right) - g_d'\dot{\lambda}\mathbf{D}_e : (\boldsymbol{\varepsilon} - \boldsymbol{\varepsilon}_p) \tag{7}$$

where

$$g_d' = \frac{\partial g_d}{\partial \kappa_p} = \frac{f_t/\varepsilon_f \exp(-\kappa_p/\varepsilon_f)(f_t + \kappa_p H_p) + f_t \exp(-\kappa_p/\varepsilon_f) H_p}{(f_t + \kappa_p H_p)^2} \tag{8}$$

The plastic multiplier, $\dot{\lambda}$, is determined from the consistency condition of the plasticity part:

$$\dot{f}_p = \frac{\partial \bar{\sigma}_1}{\partial \bar{\boldsymbol{\sigma}}}\mathbf{D}_e : \left(\dot{\boldsymbol{\varepsilon}} - \dot{\lambda}\frac{\partial \bar{\sigma}_1}{\partial \bar{\boldsymbol{\sigma}}}\right) - \dot{\lambda} H_e = 0 \tag{9}$$

as

$$\dot{\lambda} = \frac{\frac{\partial \bar{\sigma}_1}{\partial \bar{\boldsymbol{\sigma}}} : \mathbf{D}_e : \dot{\boldsymbol{\varepsilon}}}{\frac{\partial \bar{\sigma}_1}{\partial \bar{\boldsymbol{\sigma}}} : \mathbf{D}_e : \frac{\partial \bar{\sigma}_1}{\partial \bar{\boldsymbol{\sigma}}} + H_p} \tag{10}$$

By setting Eq. (10) in Eq. (7)

$$\dot{\boldsymbol{\sigma}} = \mathbf{D}_{epd} : \dot{\boldsymbol{\varepsilon}} \tag{11}$$

is obtain, where

$$\mathbf{D}_{epd} = (1-\omega)\left(\mathbf{D}_e - \frac{\mathbf{D}_e : \frac{\partial \bar{\sigma}_1}{\partial \bar{\boldsymbol{\sigma}}} \otimes \frac{\partial \bar{\sigma}_1}{\partial \bar{\boldsymbol{\sigma}}} : \mathbf{D}_e}{\frac{\partial \bar{\sigma}_1}{\partial \bar{\boldsymbol{\sigma}}} : \mathbf{D}_e} : \frac{\partial \bar{\sigma}_1}{\partial \bar{\boldsymbol{\sigma}}} + H_p\right) - g_d'\left(\frac{\mathbf{D}_e : (\boldsymbol{\varepsilon} - \boldsymbol{\varepsilon}_p) \otimes \frac{\partial \bar{\sigma}_1}{\partial \bar{\boldsymbol{\sigma}}} : \mathbf{D}_e}{\frac{\partial \bar{\sigma}_1}{\partial \bar{\boldsymbol{\sigma}}} : \mathbf{D}_e : \frac{\partial \bar{\sigma}_1}{\partial \bar{\boldsymbol{\sigma}}} + H_p}\right) \tag{12}$$

is the tangent stiffness of the elasto-plastic-damage model for one active surface.

Now, the tangent stiffness for simple shear is analyzed. Before the onset of inelastic behavior the stress state in simple shear is determined by the isotropic elastic stiffness matrix as

$$\begin{pmatrix} 0 \\ 0 \\ \sigma_{12} \end{pmatrix} = \frac{E}{1-\nu^2}\begin{bmatrix} 1 & \nu & 0 \\ \nu & 1 & 0 \\ 0 & 0 & \frac{1-\nu}{2} \end{bmatrix}\begin{pmatrix} 0 \\ 0 \\ \gamma_{12} \end{pmatrix} \tag{13}$$

where E is Young's modulus and ν is Poisson's ratio. The shear strain rate results in a shear stress rate only, since the components (1,3) and (2,3) of the isotropic linear elastic stiffness matrix in Eq. (13) are equal to zero. Thus, for isotropic elasticity, simple shear coincides with pure shear since the normal strain and stress components are zero. The direction of the maximum principal stress component with respect to the Cartesian coordinate system, for this stress state, is determined as

$$\mathbf{n}_1 = \left\{ 1/\sqrt{2} \quad 1/\sqrt{2} \right\}^T \tag{14}$$

Now, Eq. (3) is used to determine the derivative of the maximum principal stress, with respect to the effective stress tensor, which results in engineering notation to

$$\frac{\partial \bar{\sigma}_1}{\partial \bar{\boldsymbol{\sigma}}} = \left\{ 1/2 \quad 1/2 \quad 1 \right\}^T \tag{15}$$

Finally, we set Eqs. (15) and (8) into Eq. (12) and obtain, for the onset of the inelastic behavior ($\kappa_p = \omega = 0, \boldsymbol{\varepsilon}_p = \mathbf{0}$ and $\sigma_{12} = f_t$)

$$\mathbf{D}_{epd} = \mathbf{D}_e - \mathbf{R}_p - \mathbf{R}_d \tag{16}$$

where $\mathbf{D}_e$ is the elastic stiffness matrix in Eq. (13), $\mathbf{R}_p$ is the contribution of the plasticity part with

$$\mathbf{R}_p = \frac{1}{h_p}\frac{E^2}{4(1-\nu^2)^2}\begin{bmatrix} (1+\nu)^2 & (1+\nu)^2 & 1-\nu^2 \\ (1+\nu)^2 & (1+\nu)^2 & 1-\nu^2 \\ 1-\nu^2 & 1-\nu^2 & (1-\nu)^2 \end{bmatrix} \tag{17}$$

and $\mathbf{R}_d$ is the contribution of the damage part with

$$\mathbf{R}_d = \frac{g_d'}{h_p}\frac{E}{2(1-\nu^2)}\begin{bmatrix} 0 & 0 & 0 \\ 0 & 0 & 0 \\ f_t(1+\nu) & f_t(1+\nu) & f_t(1-\nu) \end{bmatrix} \tag{18}$$

Furthermore,

$$h_p = \frac{E(5+3\nu)}{8(1-\nu^2)} + H_p \tag{19}$$

and

$$g_d' = \frac{1}{\varepsilon_f} + \frac{H_p}{f_t} \tag{20}$$

The matrix, $\mathbf{R}_p$, provides volumetric–deviatoric coupling, since the components (1, 3) and (2, 3) of $\mathbf{R}_p$ are not zero for finite values of H_p. A shear strain rate, $\dot{\gamma}_{12}$, results, therefore, not only in a shear stress rate $\dot{\sigma}_{12}$, but also in two normal stress rates, $\dot{\sigma}_{11} = \dot{\sigma}_{22}$. The components (1, 3) and (2, 3) of $\mathbf{R}_d$, on the other hand, are zero, so that the damage part does not provide any volumetric–deviatoric coupling. The value of h_p in Eq. (19) depends on the hardening modulus, H_p. Consequently, the amount of volumetric–deviatoric coupling given by $\mathbf{R}_p$ is controlled by H_p. For the limit $H_p = \infty$, the components of $\mathbf{R}_p$ are zero and the volumetric–deviatoric coupling vanishes.The components of matrix $\mathbf{R}_d$, however, do not tend to zero for $H_p \to \infty$, since g_d' in Eq. (20) depends also on H_p, so that

$$\lim_{H_p \to \infty}\left(\frac{g_d'}{h_p}\right) = \frac{1}{f_t} \tag{21}$$

Thus, the elasto-plastic-damage stiffness is reduced to a pure elasto-damage stiffness for $H_p \to \infty$.

3. Elasto-plastic-damage simulation of a simple shear test in-plane stress

The total stress–strain response of the damage-plasticity model was analyzed, in particular the influence of volumetric–deviatoric interaction on the simple shear response. Four values of the plastic hardening modulus, H_p, ranging from 0 to $100E$ are used. The other model parameters chosen are $E = 30$ GPa, $\nu = 0.18$, $f_t = 3.5$ MPa and $\varepsilon_f = 0.0004$.

The influence of H_p is illustrated by the unloading behavior in uniaxial tension in Fig. 2. For $H_p = 0$, the inelastic strain is mainly irreversible ($\boldsymbol{\varepsilon}_p - \omega\boldsymbol{\varepsilon}_p$), while only a small amount of inelastic strain is reversible ($\omega\boldsymbol{\varepsilon}$).

The situation is different for $H_p = 100E$, where the plastic strain is nearly zero and the inelastic strains are almost fully reversible. Thus, the model unloads almost back to the origin of the stress–strain curve in the figure.

Also, the amount of volumetric–deviatoric coupling differs. This is illustrated by a simple shear test in-plane stress. In this strain controlled test, the shear strain is increased, while the two normal strain components are kept at zero. The shear stress–strain response is strongly influenced by the value of the plastic hardening modulus, H_p, which controls the amount of volumetric–deviatoric interaction, see Fig. 3. The maximum shear stress for $H_p = 0$ (strong interaction) is nearly 1.4 times greater than for $H_p = 100E$ (weak interaction). This

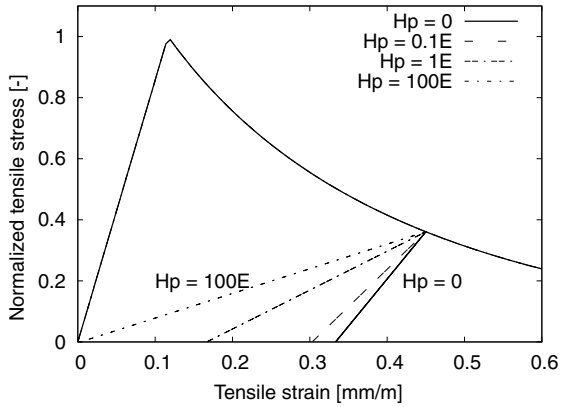

Fig. 2. The influence of the plastic hardening modulus H_p on the unloading stiffness for the elasto-plastic-damage Rankine model. The tensile stress is normalized by the tensile strength f_t.

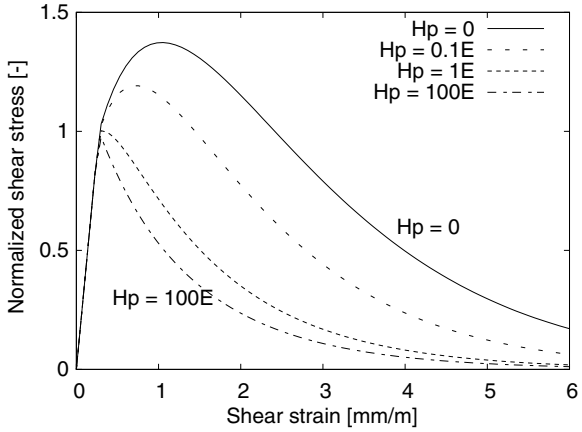

Fig. 3. The influence of the plastic hardening modulus, H_p, on the response in simple shear for the elasto-plastic-damage Rankine model. The shear stress is normalized by the tensile strength f_t.

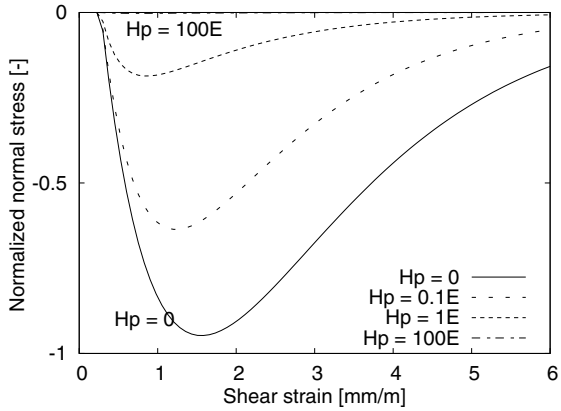

Fig. 4. The amount of activated negative normal stress due to the volumetric–deviatoric interaction, which is controlled by the plastic hardening modulus, H_p. The normal stress is normalized by the tensile strength, f_t.

difference is explained by the activation of normal compressive stresses when there is volumetric–deviatoric interaction, see Fig. 4. When the plasticity model has a strong influence, normal plastic strain components

develop; since the total strain in the normal direction is fixed, these lead to normal compressive stresses. For $H_p = 100E$ (weak influence) almost no normal compressive stresses are activated.

It should be stressed that the volumetric–deviatoric coupling not only depends on the hardening modulus, which in the present study controlls the ratio of damage and plasticity, but also on the form of the yield surface and flow rule of the plasticity model. However, in the present study only a Rankine plasticity model is considered for simplicity and coupling is only controlled by the hardening modulus.

4. Analysis of fracture tests

In the present section the results of finite element simulations of two fracture tests with curved crack patterns are presented. The crack band approach, Bažant and Oh [13], is used to obtain a mesh independent description of the dissipated energy. Two amounts of volumetric–deviatoric coupling, $H_p = 0$ and $H_p = 100E$, are considered. The plastic hardening modulus of $H_p = 0$ corresponds to strong coupling, while $H_p = 100E$ corresponds to weak coupling. The specimens are discretized by a fine mesh of bilinear quadrilateral elements assuming plane stress.

4.1. Four-point shear test

The first example is a four-point shear test of a single-edge-notched beam, conducted by Arrea and Ingraffea [1], shown in Fig. 5. The material parameters chosen are $E = 30$ GPa, $v = 0.18$, $f_t = 3.5$ MPa and $G_f = 140$ J/m^2 as used in [10]. The results are given as contour plots of the maximum principal strain (Fig. 10), and load crack mouth sliding displacement (CMSD) curve (Fig. 6).

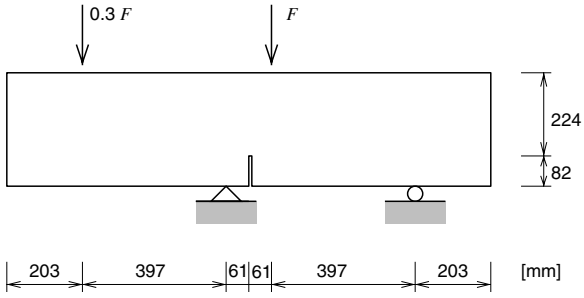

Fig. 5. The experimental setup of the four-point shear test.

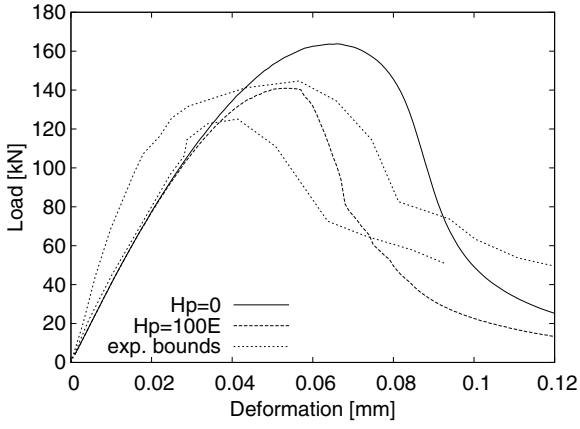

Fig. 6. Comparison of load CMSD curves for analysis and experimental bounds in the four-point shear test.

4.2. Double-edge-notched (DEN) specimen

The second example is the double-edge-notched specimen tested by Nooru-Mohamed [2]. The experimental setup is presented in Fig. 7.

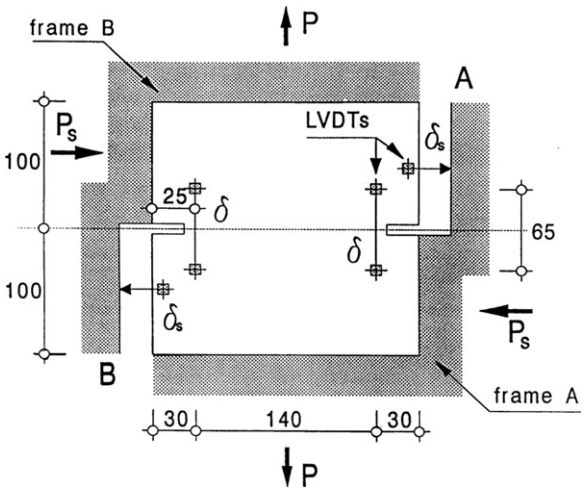

Fig. 7. The geometry and the loading setup of the DEN specimen.

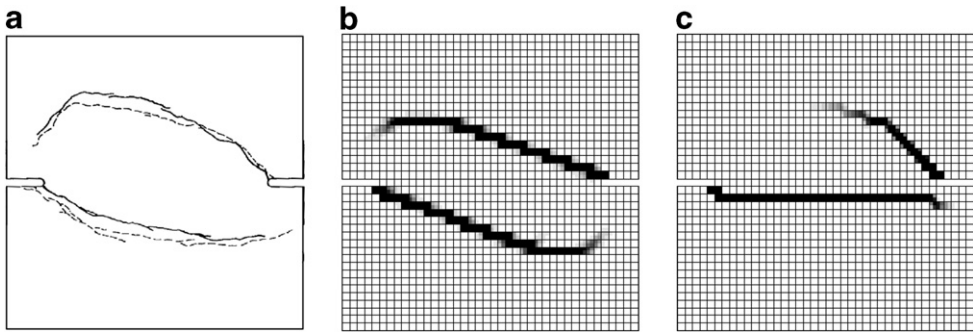

Fig. 8. Influence of the volumetric–deviatoric interaction on the crack pattern in the DEN test: (a) experiments, (b) strong interaction ($H_p = 0$), and (c) weak interaction ($H_p = 100E$).

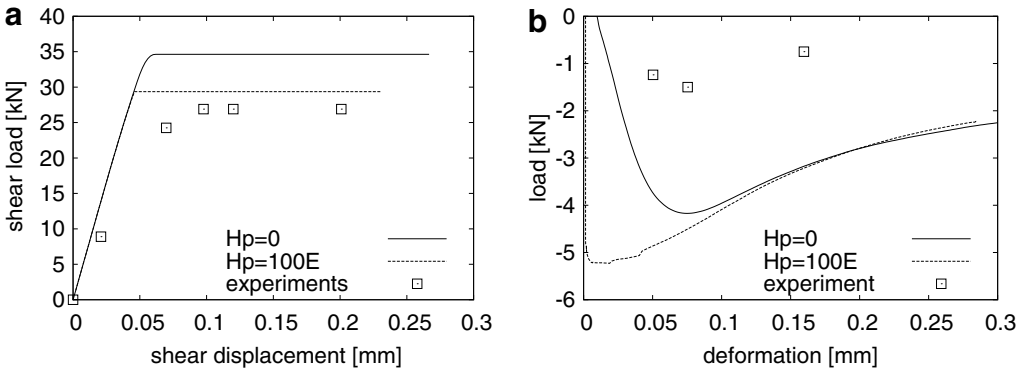

Fig. 9. Comparison of load–displacement of analysis and experiments of (a) shear force and shear displacement and (b) normal force and normal displacement for the double-edge-notched specimen.

The non proportional loading path 4c is chosen. This is the most challenging test of the entire program, because the final crack pattern consists of two cracks with a relatively strong curvature, see Fig. 8a. During the first stage, the specimen is loaded by an increasing "shear force", P_s, until the maximum force that the specimen can carry is reached. Then, in the second stage, this force is kept constant and a "normal" force, P, is applied in the vertical direction. The material parameters chosen are $E = 30$ GPa, $v = 0.2$, $f_t = 3$ MPa and $G_f = 110$ J/m^2 as used in [6] and [10]. The contour plots of the maximum principal strain for strong and weak coupling are compared with the experimental crack patterns in Fig. 8. Furthermore, the load–displacement curves for "shear" and "normal" loading are compared with the experimental results in Fig. 9, where the simulated load–deflection curve for the normal and shear directions are shown.

4.3. Discussion of the results

For strong volumetric–deviatoric coupling ($H_p = 0$), the experimental crack patterns are well represented by the elasto-plastic-damage model for both the four-point shear tests and the DEN test, see Figs. 10b and 8b. With weak coupling ($H_p = 100E$), on the other hand, the crack patterns cannot be captured. The zone of localized strains in the four-point shear test is strongly attracted by the direction of the mesh lines, see Fig. 10c. For the DEN test, the results are even worse. A horizontal localization zone forms as soon as the

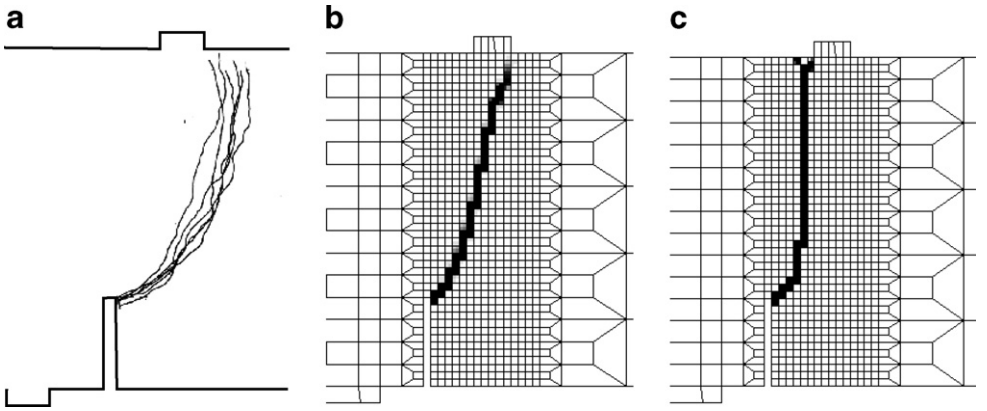

Fig. 10. Influence of the volumetric–deviatoric interaction on the crack pattern in the four-point shear test: (a) experiments, (b) strong interaction ($H_p = 0$), and (c) weak interaction ($H_p = 100E$).

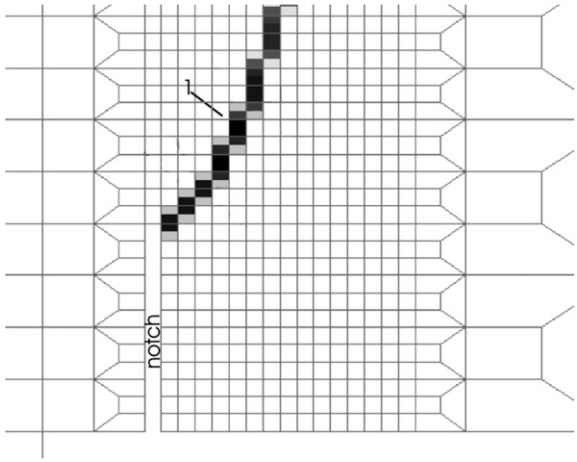

Fig. 11. Detail of the crack pattern of the four-point shear test obtained with strong interaction ($H_p = 0$).

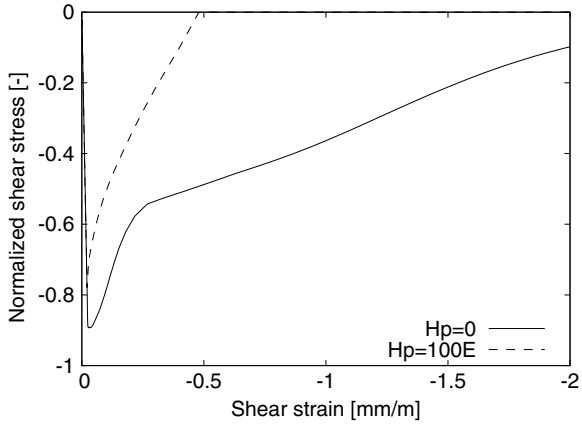

Fig. 12. The shear stress versus the shear strain in Point 1. The shear stress is normalized by the tensile strength, f_t.

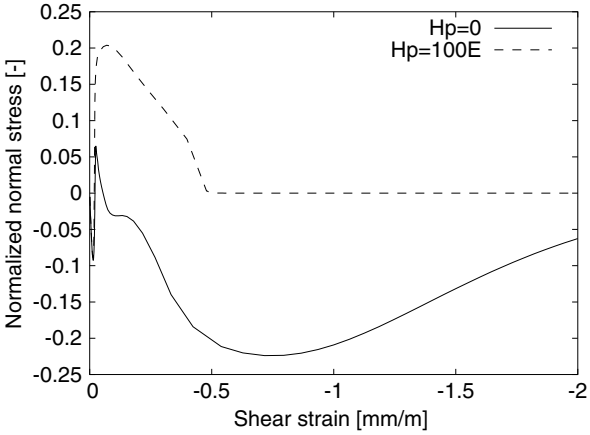

Fig. 13. The normal stress versus the shear strain in Point 1. The normal stress is normalized by the tensile strength, f_t.

tensile load is applied in the second stage of the test, see Fig. 8c. This does not agree with the curved crack patterns observed in the experiments. The results of the simulation of the mixed-mode fracture tests were further interpreted by the evaluation of the stress–strain history of an integration points close to the zones of localized strains where the profiles of the simulation with and without coupling deviate (see Fig. 11). The results in the form of the shear stress versus the shear strain and the normal stress versus the shear strain are presented in Fig. 12 and 13, respectively. With strong coupling negative normal stresses are present and the area below the shear stress–shear-strain curve is greater than without coupling. The findings in Section 3 and the stress–strain histories shown in Figs. 12 and 13 suggest that the maximum shear stress and the volume fracture energy in simple shear are increased by volumetric–deviatoric coupling, because of the restrained normal strains that generate normal compressive stresses. The strain localizes in regions where the stress state is close to uniaxial tension, since zones subjected to shear are confined and resist, therefore, higher stresses. This is the reason why, for volumetric–deviatoric coupling, the curved crack patterns can be represented, but not without coupling.

5. Conclusions

The study of the influence of volumetric–deviatoric coupling on modeling curved crack patterns leads to the following conclusions.

- Constitutive models with volumetric–deviatoric coupling provide higher shear resistance in simple shear than models without coupling. The increase in shear stress is caused by the activation of compressive stresses due to constrained strains.
- In the simulation of curved cracks, the paths of localized strain zones are strongly influenced by the amount of volumetric–deviatoric coupling. Only with volumetric–deviatoric coupling can the curved crack patterns be reproduced.

Coupling can be provided by the theory of plasticity or anisotropic damage models.

Acknowledgements

This work was supported by the Swedish Research Council for Environment, Agricultural Sciences and Spatial Planning. The simulations were made using the object-oriented finite element package OOFEM [14,15] extended by the present authors.

References

[1] Arrea M, Ingraffea AR. Mixed-mode crack propagation in mortar and concrete. Department of Structural Engineering, Cornell University, Ithaca, NY; 1982.
[2] Nooru-Mohamed MB. Mixed-mode fracture of concrete: an experimental approach. PhD thesis, Delft University of Technology, The Netherlands; 1992.
[3] Schlangen E. Experimental and numerical analysis of fracture processes in concrete. PhD thesis, Delft University of Technology, Delft, The Netherlands; 1993.
[4] Galvez JC, Elices M, Guinea GV, Planas J. Mixed mode fracture of concrete under proportional and nonproportional loading. Int J Fracture 1998;94:267–84.
[5] Cendón DA, Gálvez JC, Elices M, Planas J. Modelling the fracture of concrete under mixed loading. Int J Fracture 2000;103:293–310.
[6] di Prisco M, Ferrara L, Meftah F, Pamin J, de Borst R, Mazars J, Reynouard JM. Mixed mode fracture in plain and reinforced concrete: some results on benchmark tests. Int J Fracture 2000;103:127–48.
[7] Geers MGD, de Borst R, Peerlings RHJ. Damage and crack modeling in single-edge and double-edge notched concrete beams. Eng Fracture Mech 2000;65:247–61.
[8] Grassl P, Jirásek M. On mesh biase of local damage models for concrete. In: Li V., Leung C.K.Y., Willam K.J., Billington S.L., editors. Fracture mechanics of concrete structures: 2004; p. 323–37.
[9] Ožbolt J, Reinhardt HW. Numerical study of mixed-mode fracture in concrete. Int J Fracture. 2002;118:145–61.
[10] Patzák B, Jirásek M. Adaptive resolution of localized damage in quasibrittle materials. J Engng Mech 2003;130:720–32. ASCE.
[11] Pivonka P, Ožbolt J, Lackner R, Mang HA. Comparative studies of 3D-constitutive models for concrete: application to mixed-mode fracture. Int J Numer Meth Engng 2004;60:549–70.
[12] Willam K, Hansen E, Kang HD. Performance evaluation of damage and plasticity formulations for concrete. In: Shing P.B., Tanabe T., editors. Modeling of inelastic behavior of RC structures under seismic load. American Society of Civil Engineers; 2001. p. 1–19.
[13] Bažant ZP, Oh B-H. Crack band theory for fracture of concrete. Mater Struct 1983;16:155–77.
[14] Patzák B. Object oriented finite element modeling. Acta Polytech 1999;39:99–113.
[15] Patzák B, Bittnar Z. Design of object oriented finite element code. Adv Engng Softw 2001;32:759–67.

This page intentionally contains only this sentence.

Rempling, R.; Lundgren, K.; Gylltoft, K. (2008).
Modelling of concrete in tension – Energy dissipation in cyclic loops.
Nordic Concrete Research. (38) pp. 155–168.

This page intentionally contains only this sentence.

Modelling of Concrete in Tension – Energy dissipation in Cyclic Loops

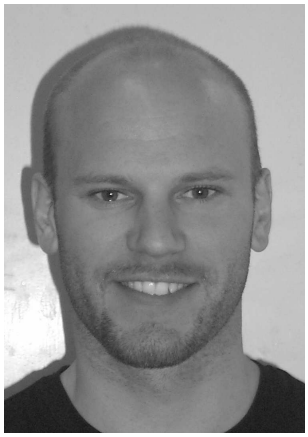

Rasmus Rempling[1]
Ph.D. student
rasmus.rempling@chalmers.se

Karin Lundgren[1]
Ass. Professor

Kent Gylltoft[1]
Professor

[1] Department of Civil and Environmental Engineering
Structural Engineering, Concrete Structures
Chalmers University of Technology
Gothenburg, Sweden

ABSTRACT

This paper deals with modelling of concrete subjected to cyclic loading in tension. A model based on the theory of plasticity combined with the theory of damage mechanics was developed. To describe the non-linearity that concrete exhibits during cyclic loading, the concept of bounding surface is used as a hardening function. An evolution law for the elastic domain is proposed that depends on the consumption of fracture energy in hysteresis loops. In addition, an energy balance equation is proposed, which deals with the consumption of fracture energy by completing hysteresis loops. Finally, a drawback in the smeared crack approach for combined damage and plasticity is identified and presented.

Keywords: plasticity theory; damage mechanics; bounding surface; concrete; fracture; cyclic loading; fatigue

1 INTRODUCTION

Cyclic loading is one of the deterioration processes of great importance for concrete structures such as piles, sleepers, machinery foundations, parts of bridges, etc. The deterioration of concrete structures entails heavy costs for the society. These costs can be cut down by an increased understanding of the cyclic-loading phenomenon and by the development of constitutive models with an increased accuracy.

Due to the non-linear stress-strain response that concrete exhibits, cyclic loading can be divided into two main characteristic responses: pre-peak cyclic loading and post-peak cyclic loading. Pre-peak cyclic loading is cyclic loading before maximum load is reached, while post-peak cyclic loading is cyclic loading after maximum load and localization of deformation. These phenomena are equally important as parts of cyclic loaded structures may be in pre-peak state, while other parts are in post-peak state.

The work presented here deals with concrete subjected to cyclic loading in biaxial tension with focus on improving the analysis methods for such cases and increasing the understanding of the deterioration processes related to repeated loading.

Plasticity, damage mechanics, and the combination of both, are often used to describe the non-linear response of concrete, e.g. models [1]-[3]. Moreover, the concept of bounding surface, introduced by [4], has been proved to be useful to describe the hysteresis loops that concrete exhibits when subjected to cyclic loading: [5]-[10]. Research that identifies the characteristic hysteresis loops has been conducted by [11]-[30]. The combination of plasticity and damage mechanics used in this investigation was previous investigated by e.g. [31]-[33] and [34], and shows good results for complex crack patterns.

The model presented here is based on the theory of plasticity combined with the theory of damage mechanics, using the concept of bounding surface to describe the non-linearity seen when hysteresis loops from experiments are examined. The basic equations for the plasticity-damage model are presented together with the hardening rule that is based on the bounding surface concept. An evolution law for the elastic domain is proposed that describes the increasing non-linearity with increasing damage. Moreover, an energy balance equation is stated and motivated, which considers the dissipated fracture energy while completing a loading cycle in biaxial tension (Figure 1).

The crack band approach of [35] is used to control the mesh dependence of the softening branch of the stress-strain curve. The crack band approach makes it possible to consider the crack strain as the average over a characteristic crack band width w_c of the fracture process zone.

2 THE CONCEPT OF BOUNDING SURFACE

Plasticity models with two yield surfaces were introduced by [36] to describe the non-linear hardening behaviour for ductile solids with continuum models. Two surface models have later been renamed as bounding surface models due to the enclosing nature of the bounding

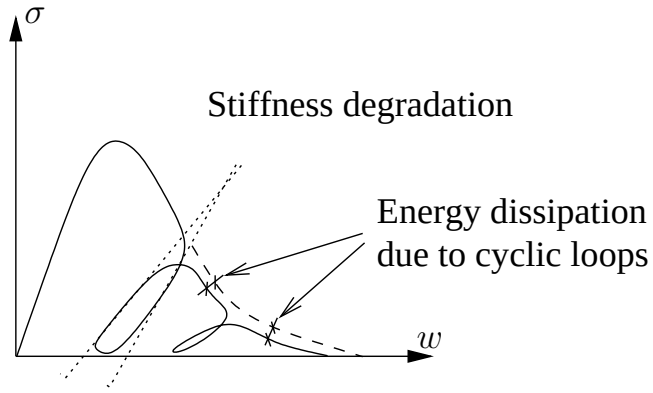

Figure 1: Illustration of the observed mechanisms related to fatigue.

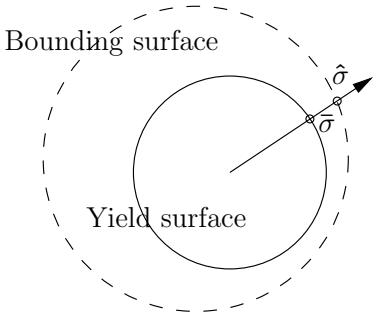

Figure 2: Illustration of the enclosing nature of the bounding surface with regard to the yield surface and the actual stress $\bar{\boldsymbol{\sigma}}$, with the corresponding mirror stress $\hat{\boldsymbol{\sigma}}$.

surface with regard to the yield surface. The concept of bounding surface models is to describe the non-linear hardening and softening behaviour by prescribing the variation of the plastic modulus K_{p}, i.e. another way of describing strain hardening. The plastic modulus is determined by the distance between the position of the actual plastic loading point and the mirror point on the bounding surface δ. A general definition of δ is

$$\delta = \sqrt{(\hat{\boldsymbol{\sigma}} - \bar{\boldsymbol{\sigma}})^2} \tag{1}$$

where $\hat{\boldsymbol{\sigma}}$ contains the coordinates of the mirror point on the bounding surface and $\bar{\boldsymbol{\sigma}}$ is the actual plastic stress point; in this study the actual plastic stress is the effective stress, i.e. the stress in the undamaged stress space. $\hat{\boldsymbol{\sigma}}$ is determined along the normal to the bounding surface (Figure 2). The computation of $\hat{\boldsymbol{\sigma}}$, is done with a function, $\boldsymbol{M}$, called the mapping rule:

$$\hat{\boldsymbol{\sigma}} = \boldsymbol{M}(\bar{\boldsymbol{\sigma}}). \tag{2}$$

The bounding surface is constructed in the same way as a yield surface; thus the bounding surface and the flow rule are generally described, respectively as

$$F = 0, \quad \dot{\hat{L}} = \dot{\hat{\lambda}} \frac{\partial F}{\partial \hat{\boldsymbol{\sigma}}} \tag{3}$$

where $\dot{\hat{\lambda}}$ is the rate of the plastic multiplier. The identity condition, $\bar{\boldsymbol{\sigma}}$ on $F = 0$ so that

$\bar{\boldsymbol{\sigma}} = \hat{\boldsymbol{\sigma}}$ and $\frac{\partial f}{\partial \bar{\boldsymbol{\sigma}}} = \frac{\partial F}{\partial \hat{\boldsymbol{\sigma}}}$, introduces restrictions on the relative evolution of the surfaces due to the fact that they can never intersect with each other.

Bounding surface models make it possible for the plastic response to evolve depending on the distance from the actual stress state $\bar{\boldsymbol{\sigma}}$ to the bounding surface itself. An evolution law K_{pf} for the plastic modulus K_{p} can be stated as

$$K_{\mathrm{p}} = K_{\mathrm{pf}}(\delta). \tag{4}$$

Equation (4) expresses the main feature of the bounding surface, i.e. the plastic deformation is calculated by K_{p}, with a magnitude based on δ.

3 THE PLASTICITY-DAMAGE MODEL

Experimental observation of concrete subjected to cyclic loading reveals a non-linear stress-strain response with increasing plastic deformation during loading, as well as a degradation of the material due to damage. Therefore, it is convenient when developing a constitutive model to use the theory of plasticity to describe the plastic deformation and at the same time describe the evolution of damage with damage mechanics.

The model presented here is a combination of plasticity and damage with a kinematic hardening rule based on the theory of bounding surface. The damage is determined by the accumulated plastic strain and a fracture energy consumption law. To deal with localization the deformation in the softening regime, the crack width w_{c}, is smeared over the element length. The stress-strain relationship is given as

$$\boldsymbol{\sigma} = (1-\omega)\bar{\boldsymbol{\sigma}} = (1-\omega)\boldsymbol{E}_{\mathrm{e}} : (\boldsymbol{\varepsilon} - \boldsymbol{\varepsilon}_{\mathrm{p}} + \boldsymbol{\varepsilon}_{\mathrm{p},\emptyset}) \tag{5}$$

where: $\boldsymbol{\sigma}$ is the nominal stress,
ω is the isotropic damage parameter,
$\bar{\boldsymbol{\sigma}}$ is the effective stress,
$\boldsymbol{E}_{\mathrm{e}}$ is the isotropic elastic stiffness,
$\boldsymbol{\varepsilon}$ is the total strain,
$\boldsymbol{\varepsilon}_{\mathrm{p}}$ is the plastic strain at loading and
$\boldsymbol{\varepsilon}_{\mathrm{p},\emptyset}$ is the plastic strain at unloading.

3.1 Plasticity model

The plasticity model is based on the effective stress and consists of: a yield function based on the Rankine criterion, a flow rule, a hardening rule, an evolution law for the elastic domain and the loading-unloading conditions.

The elastic domain is a crucial issue for concrete subjected to cyclic loading. In experimental observations it is observed that during cyclic loading a non-linear state is exhibited during loading as well as unloading. In between these non-linear states the response is elastic

with a stiffness that corresponds to the level of damage. This can be understood as the elastic domain moves with the non-linear response without changing shape. This rigid body movement is described by the hardening function of the model presented below. At the same time, energy is released by the completion of a hysteresis loop, which can be observed in experiments as an increase of the non-linear response. This increase of non-linearity is done at the cost of the elastic domain, i.e. the elastic domain decreases in size during cyclic loading. This is considered in the model by the evolution law for the elastic domain that is based on the energy balance equation stated below.

3.1.1 Loading

For loading in plane stress the yield function becomes

$$f(\bar{\sigma}_1, \delta) = \bar{\sigma}_1 - \sigma_{\mathrm{y},1}^{N,n}(\delta) \tag{6}$$

where $\bar{\sigma}_1$ is the maximum principal value of the effective stress tensor $\bar{\boldsymbol{\sigma}}$, $\sigma_{\mathrm{y},1}^{N,n} = \sigma_{\mathrm{y},1}^{N,(n-1)} + H(\delta)$ is the yield stress, updated from the previous step $(n-1)$ and $H(\delta)$ is the hardening rule.

When the stress state violates the yield condition $f = 0$, plastic flow is initiated. The flow rule is associated and given as

$$\dot{\boldsymbol{\varepsilon}}_{\mathrm{p}} = \dot{\lambda}\frac{\partial f}{\partial \bar{\boldsymbol{\sigma}}} \tag{7}$$

where $\dot{\lambda}$ is the rate of the plastic multiplier.

The evolution of the yield surface during plastic flow, Figure 3, is controlled by the hardening rule. The hardening rule $H(\delta)$ is linearly dependent on the maximum principal effective stress ($\delta = \hat{\sigma}_1 - \bar{\sigma}_1$) and to achieve a practical hardening rule, δ is normalized with $\hat{\sigma}_1 - \sigma_{\mathrm{y},1}^{N,n}$. $\sigma_{\mathrm{y},1}^{N,n}$ is the yield stress at the initiation of plastic flow for the actual cycle N, which initially is set at input with the parameter σ_{yin}. Then, the hardening rule yields

$$H(\delta) = E\frac{\hat{\sigma}_1 - \bar{\sigma}_1}{\hat{\sigma}_1 - \sigma_{\mathrm{y},1}^{N,n}} \tag{8}$$

where $\hat{\sigma}_1$ is the mirror stress of the actual stress.

For loading the elastic domain is constant, though it translates in stress space during plastic flow. Therefore, the lower yield surface $\sigma_{\mathrm{y},\emptyset,1}^{N,n}$ must be updated for $\delta \geq 0$ (Figure 4). The updating is done according to

$$\sigma_{\mathrm{y},\emptyset,1}^{N,n} = \sigma_{\mathrm{y},\emptyset,1}^{N,(n-1)} + H(\delta). \tag{9}$$

3.1.2 Unloading

For unloading the equations differ slightly.

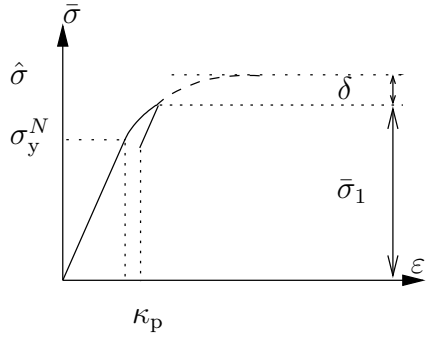

Figure 3: Evolution of the yield surface due to plastic loading.

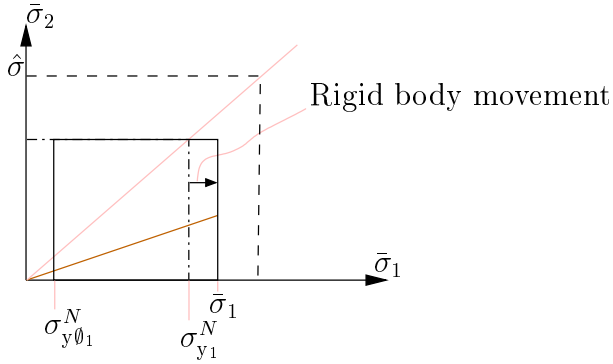

Figure 4: The hardening is kinematic which represents a rigid body movement of the elastic domain.

The yield function is stated as

$$f_{\emptyset}(\bar{\sigma}_1, \delta_{\emptyset}) = -\bar{\sigma}_1 + \sigma_{\mathrm{y},\emptyset,1}^{N,n}(\delta_{\emptyset}) \tag{10}$$

where $\bar{\sigma}_1$ is the maximum principal value of the effective stress $\bar{\boldsymbol{\sigma}}$ and

$$\sigma_{\mathrm{y},\emptyset,1}^{N,n} = \sigma_{\mathrm{y},\emptyset,1}^{N,(n-1)} - H_{\emptyset}(\delta_{\emptyset}) \tag{11}$$

is the yield stress, updated from the previous step $(n-1)$, for the lower bound and $H_{\emptyset}(\delta_{\emptyset})$ is the unloading hardening rule.

The flow rule is

$$\dot{\boldsymbol{\varepsilon}}_{\mathrm{p},\emptyset} = \dot{\lambda}_{\emptyset} \frac{\partial f_{\emptyset}}{\partial \bar{\boldsymbol{\sigma}}} \tag{12}$$

where $\dot{\lambda}_{\emptyset}$ is the rate of the plastic multiplier for unloading.

The evolution law for the unloading plastic multiplier is calculated as

$$\dot{\kappa}_{\mathrm{p},\emptyset} = \|\dot{\boldsymbol{\varepsilon}}_{\mathrm{p},\emptyset}\| = \dot{\lambda}_{\emptyset}. \tag{13}$$

The hardening rule together with the normalization of $\delta_{\emptyset}$ ($\delta_{\emptyset} = \bar{\sigma}_1 - \hat{\sigma}_{\emptyset,1}$) give the unloading hardening rule

$$H_{\emptyset}(\delta_{\emptyset}) = E \frac{\bar{\sigma}_1 - \hat{\sigma}_{\emptyset,1}}{\sigma_{\mathrm{y},\emptyset,1}^{N,n} - \hat{\sigma}_{\emptyset,1}} \tag{14}$$

where $\hat{\sigma}_{\emptyset,1}$ is the unloading mirror stress, considered as a material parameter.

According to the rigid body movement of the elastic domain the upper yield surface is updated during plastic flow. This is considered by the consistent equation for the elastic domain at unloading and is defined according to

$$\sigma_{\mathrm{y},1}^{N,n} = \sigma_{\mathrm{y},1}^{N,(n-1)} - H_{\emptyset}(\delta_{\emptyset}). \tag{15}$$

3.1.3 Loading-unloading conditions

The loading-unloading conditions conclude the plasticity part. The yield function must remain negative in the elastic regime at the same time as the rate of the plastic multiplier initially must be zero, or remain constant at reloading. In the plastic regime the yield function must be zero and the rate of the plastic multiplier must be positive. The conditions are stated as follows:

- Loading:

$$f \leq 0 \quad \dot{\lambda} \geq 0 \quad \dot{\lambda} f = 0 \tag{16}$$

- Unloading:

$$f_{\emptyset} \leq 0 \quad \dot{\lambda}_{\emptyset} \geq 0 \quad \dot{\lambda}_{\emptyset} f_{\emptyset} = 0 \tag{17}$$

These last conditions in Equations 16 and 17 are the conditions that separate the elastic regime from the plastic regime. The conditions state that when $f = 0$ then $\dot{\lambda} \geq 0$, and if $f \leq 0$ then $\dot{\lambda} = 0$ (for loading and unloading).

3.2 Damage model

The damage model consists of a fracture surface determined by the damage function and an isotropic damage variable $\omega(\kappa_{\mathrm{D}})$. The damage variable is determined so that the resulting stress-strain relation for monotonic loading will be an exponential function for loading in the softening region. Damage evolves with two different cases:

1. When the maximum principal value of the effective stress reaches the bounding surface: this is checked by the damage function.

$$f_{\mathrm{D}} = \bar{\sigma}_1 - \hat{\sigma}_1 \tag{18}$$

2. When the damage history variable increases the damage history variable is computed by the current plastic strain $\varepsilon_{\mathrm{p},1}$ and the plastic strain at initiation of damage $\varepsilon_{0,\mathrm{p}}$.

$$\kappa_{\mathrm{D}} = max(\varepsilon_{\mathrm{p},1} - \varepsilon_{0,\mathrm{p}}). \tag{19}$$

If damage is present the isotropic damage parameter is calculated according to

$$\omega(\kappa_{\mathrm{D}}) = \frac{1 - \frac{\varepsilon_0}{\kappa_{\mathrm{D}}}}{1 - \frac{\varepsilon_0}{\varepsilon_{\mathrm{f}}}} \tag{20}$$

where $\varepsilon_0 = f_{\mathrm{u}}/E$ is the strain that corresponds to the initiation of damage, ε_{f} is the final strain and f_{u} is the ultimate strength given at input.

Because the yield surface initially is separated from the bounding surface, strain hardening of the effective stress $\bar{\boldsymbol{\sigma}}$ is present after yielding has been initiated; but only to some extent as the effective stress converges rapidly with the bounding surface. In addition, the amount of strain hardening is small compared to the total crack strain.

3.3 Energy dissipation

In cyclic loading the loading pattern produces hysteresis loops which make energy dissipate. There are three main mechanisms that dissipate energy: temperature, the cohesive zone, and shear friction. In the biaxial tension region, crack sliding is a minor issue. Thus, the energy dissipation in the cohesive zone and the temperature increase are in main focus. Based on the discussions about energy dissipation at cyclic loading found in [37], [24], [38], and [14], there should be an energy dissipation when a load cycle is completed, considering the total energy that should be released as constant regardless of the loading history. From this statement it is possible to set up a balance equation: between the energy inside a loop E_1 and the dissipated fracture energy E_2 so that the fracture energy G_{f} remains constant (Figure 5). If plasticity is initiated while unloading, energy is released; this dissipation of energy appears for pre-peak- as well as post-peak unloading. In the model the energy release for post-peak hysteresis loops is accounted for by reducing the softening branch, related to the energy dissipated by the cyclic loop E_1. The energy released by the cyclic loop can be estimated in a simplified way by computing the area that is bound by the current loading yield stress and the actual effective stress during unloading-plastic flow

$$E_1 = (\sigma_{\mathrm{y},1}^N - \bar{\sigma}_1)\kappa_{\mathrm{p},\emptyset}. \tag{21}$$

In Equation 21 and the following equations equilibrium is assumed and therefore n is omitted.

The fracture energy is depending on the current yield surface as the fracture energy is known as the area under the softening curve. Therefore, the decrease in fracture energy can be calculated as an evolution of the elastic domain, i.e. the yield surfaces are adjusted with E_1 and a factor B. The material parameter B reflects the fact that the two areas are not equal due to temperature release, i.e. $E_2 = B\,E_1$ $(0 \leq B \leq 1)$. The reason for dealing with this in the effective stress space is related to the hypothesis that the energy release due to hysteresis loops is related to plastic flow. Even though this is done in the effective-stress space, a corresponding response in the nominal-stress space is achieved.

$$\sigma_{\mathrm{y},1}^{N+1} = \sigma_{\mathrm{y},1}^N - B\,\frac{E_1}{G_{\mathrm{f}}}\sigma_{\mathrm{y},1}^N \tag{22}$$

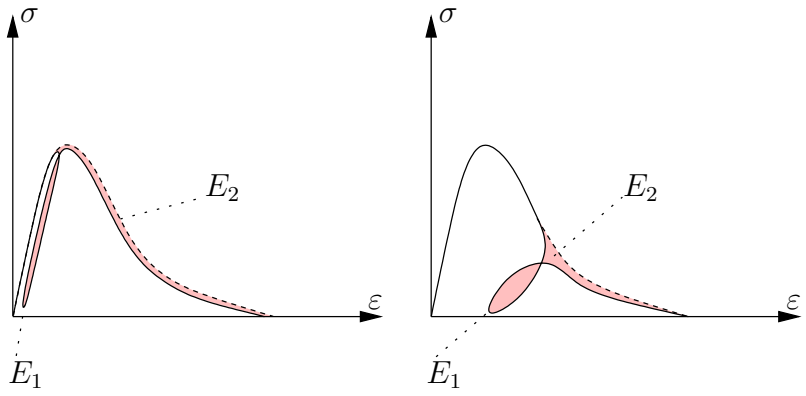

Figure 5: Illustration of the energy balance between a produced hysteresis loop and the released energy.

$$\sigma_{\mathrm{y},\emptyset,1}^{N+1} = \sigma_{\mathrm{y},\emptyset,1}^{N} + B\,\frac{E_1}{G_\mathrm{f}}\sigma_{\mathrm{y},1}^{N} \tag{23}$$

To consider energy release for pre-peak cyclic loading the bounding surface is decreased during unloading plastic flow:

$$\hat{\sigma}^{N+1} = \hat{\sigma}^{N} - A\frac{E_1}{G_\mathrm{f}}\sigma_{\mathrm{y},1}^{N} \tag{24}$$

where $\hat{\sigma}^N$ is the mirror stress related to the previous cycle ($\hat{\sigma}^N$ is initially set to f_u). The bounding surface is updated for every loading cycle N. The material parameter A is similar to B, besides that it controls the energy balance of pre-peak cyclic loading.

4 ANALYSIS OF DIRECT TENSION TEST

A finite element simulation of a tension test is described in the present section. The example is a tension test of a double-edge-notched plate, conducted by [12], shown in Figure 6. The specimen is discretized by a fine mesh of triangular three-node elements, Figure 7, assuming plane stress. For simplicity, the specimen is modelled as a quarter of the real specimen, fixing the boundaries of symmetry in the normal direction. The deformation of the specimen is applied along the edge at the right hand side in Figure 7. Until the first unloading, the deformation is applied by controlling the deformation over the notch. Thereafter, deformation is controlled at the same point where it is applied. The crack band approach is used to obtain a mesh independent description of the dissipated energy. For the element row at the notch, the smearing distance is chosen as the width of the notch, 3mm, and for the rest of the elements as the size of the elements. The given material parameters, from the experiment, are presented in Table 1 and the chosen material parameters for the model are presented in Table 2.

Table 1: Material parameters given from experiment by [12].

E	30 GPa	ν	0.18
G_f	58 Nm/m^2	f_u	3.7 MPa

Table 2: Material parameters chosen for the model.

$\sigma_{\mathrm{y_{in}}}$	3.7 MPa
A	0.05
B	0.05

4.1 Discussion of the results

The result from the analysis is compared to test results by [12] in Figure 8. The simulation shows a loading pattern of three cycles in the post-peak regime. The general response of the experiment is well described by the numerical simulation. The important hysteresis loops are well represented, as is the reduction of the softening branch. However, the simulated hysteresis loops show a slightly increasing deviation in unloading-reloading stiffness with increasing damage, which can be explained as a limitation of the chosen localization model, explained in the following.

By looking at the unloading stiffness of a bar of length L the limitation can be identified (see Figure 9). The decrease of the deformation is defined as

$$\Delta u = (L - L_\mathrm{e})\Delta\varepsilon_\mathrm{unloc} + L_\mathrm{e}\Delta\varepsilon_\mathrm{loc} \tag{25}$$

where $\Delta\varepsilon_\mathrm{unloc}$ is the strain decrement in the zones without strain localization and $\Delta\varepsilon_\mathrm{loc}$ is the strain decrement in the zone with localized deformation. The localization zone is for the chosen localization model chosen as the element length L_e.

The corresponding stress decrements can be expressed as

$$\Delta\sigma_\mathrm{unloc} = E\Delta\varepsilon_\mathrm{unloc} \tag{26}$$

$$\Delta\sigma_\mathrm{loc} = E(1-\omega)\Delta\varepsilon_\mathrm{loc} \tag{27}$$

where $\Delta\sigma_\mathrm{unloc}$ is the stress decrement in the zone without localization and $\Delta\sigma_\mathrm{loc}$ is the stress decrement in the zone with localization (Figure 9). As equilibrium applies, these stresses

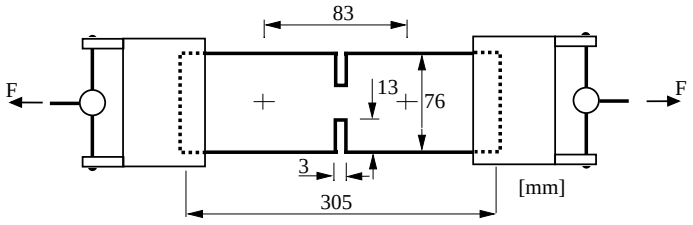

Figure 6: Experimental setup for the direct tension test. The thickness of the specimen is 19mm.

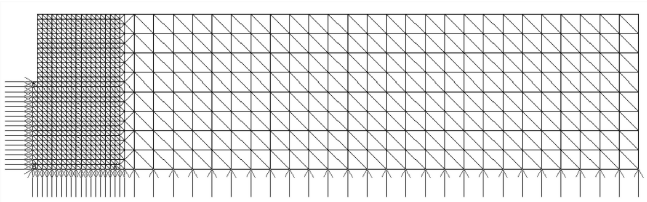

Figure 7: Finite element mesh and boundary conditions of the specimen.

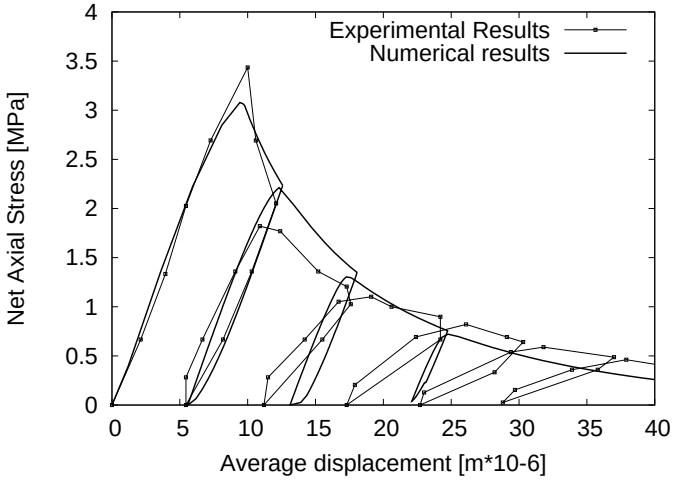

Figure 8: Simulated result of the direct tension test by [12]. The net axial stress, i.e. the load over the net area in the notch plane, is plotted over an average displacement over the notch by a length of 83 mm.

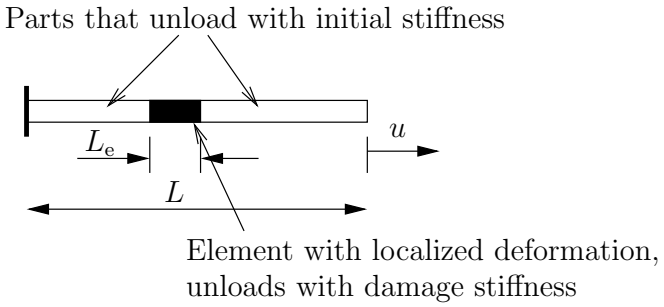

Figure 9: Definition of the stresses outside and inside the element with localized deformation.

shall be equal. Thus, the decrease of deformation, Equation 25, can be expressed as

$$\begin{aligned} \Delta u &= (L - L_{\mathrm{e}})\frac{\Delta\sigma}{E} + L_{\mathrm{e}}\frac{\Delta\sigma}{E(1-\omega)} \\ &= \frac{\Delta\sigma}{E}\frac{L(1-\omega)+\omega L_{\mathrm{e}}}{1-\omega} \end{aligned} \tag{28}$$

The unloading stiffness is identified as

$$K_{\mathrm{u}} = \frac{\Delta\sigma}{\Delta u} = \frac{(1-\omega)E}{(1-\omega)L + \omega L_{\mathrm{e}}}. \tag{29}$$

Therefore, the unloading stiffness depends on the element length. Furthermore, from Equation 29 it can be seen that if L_{e} approaches zero, the unloading stiffness approaches the initial stiffness

$$K_{\mathrm{u}} = \frac{E}{L} \tag{30}$$

which concludes the problem.

5 CONCLUSIONS

A model for concrete subjected to cyclic loading in tension was presented. The model combines plasticity theory and damage mechanics and uses the concept of bounding surface to describe the hardening, making it possible to produce hysteresis loops representing loading and unloading. The model was tested with a direct tension test conducted by [12] and shows possibilities of simulating a series of unloadings and reloadings. The numerical result represents the experiment well; the important hysteresis loops are reproduced as well as the decrease in the softening branch, although the numerical result shows larger unloading-reloading stiffness than experimental results. A drawback in the used localization model is identified: the unloading stiffness is depending on the length of the element in which the deformations localize.

ACKNOWLEDGEMENT

This work was supported by the Swedish Research Council for Environment, Agricultural Science and Spatial Planning. The simulations were made with the object-oriented finite element package OOFEM ([39], [40]) extended by the present authors.

NOTATIONS

$\dot{}$	Superscript: Denoting the rate form of a variable
δ	Euclidean distance
$\Delta\varepsilon$	Strain increment
$\varepsilon_{0,\mathrm{p}}$	Plastic strain at the initiation of damage
ε_0	Strain at initiation of damage
ε_f	Final strain at a fully opened crack
$\boldsymbol{\varepsilon}$	Strain
$\boldsymbol{\varepsilon}_{\mathrm{p}\emptyset}$	Plastic strain lower bound
$\boldsymbol{\varepsilon}_\mathrm{p}$	Plastic strain
$\emptyset$	Subscript: unloading variables
κ_D	Damage history variable
κ_p	Plastic hardening parameter
λ	Plastic multiplier
$\hat{\lambda}$	Plastic multiplier, bounding surface
ν	Poisson ratio
ω	Damage parameter
$_1$	Subscript: Maximum value of the principal directions
$\bar{\boldsymbol{\sigma}}$	Effective stress
$\Delta\sigma$	Stress increment
$\hat{\boldsymbol{\sigma}}$	Stress on boundary surface
σ_yin	Initial yield stress
σ_y	Yield stress
$\boldsymbol{\sigma}$	Nominal stress
A	Material parameter
B	Material parameter
$\boldsymbol{E}_\mathrm{e}$	Elastic stiffness tensor
E	Youngs modulus

E_1	Energy inside a hysteresis loop
E_2	Consumed energy by a hysteresis loop
F	Bounding surface function
f	Yield function
f_D	Damage function
f_u	Ultimate tensile stress
G_f	Fracture energy
H	Hardening function
K_pf	Plastic modulus function
K_p	Plastic modulus
K_u	Decrease of deformation
$\hat{L}$	Flow rule, bounding surface
$_\mathrm{loc}$	Subscript: Zone with localization of deformation
L	Length of a bar
L_e	Element length
$\boldsymbol{M}$	Mapping function
^{N}	Superscript: Number of cycles
^{n}	Superscript: Number of iterations
Δu	Decrease of deformation
$_\mathrm{unloc}$	Subscript: Zone without localization of deformation
w	Deformation

REFERENCES

1. Papa, E., & Taliercio, A., "Anisotropic damage model for the multiaxial static and fatigue behaviour of plain concrete", *Engineering Fracture Mechanics*, Vol. 55, 1996, pp. 163–179.
2. Ragueneau, F., Norderie, C. L., & Mazars, J., "Damage model for concrete-like materials coupling cracking and friction, contribution towards structural damping: first uniaxial applications", *Mechanics of Cohesive-Frictional Materials*, Vol. 5, 2000, pp. 607–625.
3. Desmorat, R., Ragueneau, F., & Pham, H., "Continuum damage mechanics for hysterisis and fatigue of quasi-brittle materials and structures", *International Journal for Analytical and Numerical Methods in Geomechanics*, Vol. 31, 2007, pp. 307–329.
4. Dafalias, Y., "Bounding surface plasticity. i: Mathematical foundation and hypoplasticity", *Journal of Engineering Mechanics*, Vol. 112, No. 9, 1986, pp. 966–987.
5. Voyiadjis, G. Z., & Abulebdeh, T. M., "Damage model for concrete using bounding surface concept", *Journal of Engineering Mechanics-ASCE*, Vol. 119, No. 9,, 1993, pp. 1865–1885.
6. Voyiadjis, G. Z., & Abulebdeh, T. M., "Plasticity model for concrete using the bounding surface concept", *International Journal of Plasticity*, Vol. 10, No. 1,, 1994, pp. 1–21.
7. Yang, B.-L., Dafalias, Y. F., & Herrmann, L. R., "Bounding surface plasticity model for concrete", *Journal of Engineering Mechanics*, Vol. 111, No. 3, 1985, p. 359.
8. Winnicki, A., & Cichon, C., "Plastic model for concrete in plane stress state. i.: Theory", *Journal of Engineering Mechanics*, Vol. 124, 1998, pp. 591–602.
9. Pandolfi, A., & Talercio, A., "Bounding surface models applied to fatigue of plain concrete", *Journal of engineering Mechanics*, Vol. 124, 1998, pp. 556–564.
10. Abulebdeh, T. M., & Voyiadjis, G. Z., "Plasticity-damage model for concrete under cyclic multiaxial loading", *Journal of Engineering Mechanics-ASCE*, Vol. 119, 1993, pp. 1465–1484.
11. Reinhardt, H. W., Cornelissen, H. A. W., & Hordijk, D. A., "Tensile tests and failure analysis of concrete", *Journal of Structural Engineering*, Vol. 112, No. 11,, 1986, pp. 2462–2477.
12. Gopalaratnam, V., & Shah, S., "Softening response of plain concrete in direct tension", *Journal of the American Concrete Institute*, Vol. 82, No. 3, 1985, pp. 310–323.
13. Plizzari, G., Cangiano, S., & Alleruzzo, S., "The fatigue behaviour of cracked concrete", *Fatigue and Fracture of Engineering Materials and Structures*, Vol. 20, No. 8, 1997, pp. 1195–1206.
14. Gylltoft, K., Fracture mechanics models for fatigue in concrete structures, Doctoral thesis, Luleå University of Technology, Luleå, Sweden, No. 1983:25D, 1983.
15. Karsan, I. D., & Jirsa, J. O., "Behaviour of concrete under compressive loadings", *Journal of Structural Division-ASCE*, Vol. 95, 1969, pp. 2543–2563.
16. Sinha, B. P., Gerstle, K. H., & Tulin, L. G., "Stress-strain relations for concrete under cyclic loading", *American Concrete Institute – Journal*, Vol. 61, No. 2, 1964, p. 195.
17. Holmen, J., Fatigue of concrete by constant and variable amplitude loading, Doctoral thesis, The Norwegian Institute of Technology, Trondheim, Norway, No. 79-1, 1979.
18. Petkovic, G., Properties of concrete related to fatigue damage with emphasis in high strength concrete, Doctoral thesis, Universitetet i Trondheim, Norges tekniske hogskole, 1991.
19. Tepfers, R., "En undersökning av betongens utmattningshållfashet", Tech. Rep. R86:1978, Avdelningen för husbyggnadsteknik, Chalmers University of Technology, Swe-

den,, 1978.
20. CEB, Fatigue of concrete structures, state of the art report, Technical Report 188, 1988, 300 pp.
21. van Mier, J., Strain-softening of concrete under multiaxial loading conditions., Doctoral thesis, Technische hogeschool Eindhoven, The Netherlands, 1984.
22. van Mier, J. G. M., "Fracture of concrete under complex stress", Tech. Rep. 31, Heron, 1986.
23. Hai-cheng, L., Wei, C., & Yu-pu, S., "Fatigue properties of plain concrete under triaxial compressive cyclic loading", *China Ocean Engineering*, Vol. 18, No. 3, 2004, pp. 457–468.
24. Spooner, D., & Dougill, J., "Quantitative assessment of damage sustained in concrete during compressive loading", *Magazine of Concrete Research*, Vol. 27, No. 92, 1975, pp. 151–160.
25. Cornelissen, H. A. W., Hordijk, D. A., & Reinhardt, H. W., "Experimental determination of crack softening characteristics of normalweight and lightweight concrete", *Heron*, Vol. 31, No. 2, 1986, pp. 45–56.
26. Baluch, M., Qureshy, A., & Azad, A., Fatigue crack propagation in plain concrete, SEM-RILEM International Conference., 1987, 112-119 pp.
27. Thun, H., Assessment of Fatigue Resistance and Strength in Existing Concrete Structures, Doctoral thesis, Luleå University of Technology, 2006.
28. Holmberg, G., Fatigue of Concrete Piles of High Strength Concrete Exposed to Impact Load, Licentiate thesis, Chalmers University of Technology, 2001.
29. Svahn, P.-O., Dynamic Behaviour of Reinforced Concrete Structures: Analyses with a strong discontinuity approach, Doctoral thesis, Chalmers University of Technology, 2005.
30. Johansson, U., Fatigue tests and analysis of reinforced concrete bridge deck models, Licentiate thesis, Royal Institute of Tecjnology, 2004.
31. Simo, J., & Ju, J., "Strain-based and stress-based continuum damage models 1. formulation", *International Journal of Solids And Structures*, Vol. 23, No. 7, 1987, pp. 821–840.
32. Lee, J., & Fenves, G., "Plastic-damage model for cyclic loading of concrete structures", *Journal of Engineering Mechanics-Asce*, Vol. 124, No. 8, 1998, pp. 892–900.
33. Grassl, P., & Rempling, R., "Influence of volumetric-deviatoric coupling on crack prediction in concrete fracture tests", *Engineering Fracture Mechanics*, Vol. 74, No. 10, 2007, pp. 1683–1693.
34. Jason, L., Pijaudier-Cabot, G., Huerta, A., Crouch, R., & Ghavamian, S., "An elastic plastic damage formulation for the behavior of concrete", in V. Li, C. Leung, K. Willam, & S. Billington, eds., Fracture mechanics of concrete structures, 2004, pp. 549–556.
35. Bažant, Z., & Oh, B., "Crack band theory for fracture of concrete", *Materiaux et Constructions*, Vol. 16, No. 93, 1983, pp. 155–177.
36. Dafalias, Y., & Popov, E., "Model of nonlinearly hardening materials for complex loading", *Acta Mechanica*, Vol. 21, No. 3, 1975, pp. 173–192.
37. Spooner, D., Pomeroy, C., & Dougill, J., "Damage and energy-dissipation in cement pastes in compression", *Magazine of Concrete Research*, Vol. 28, No. 94, 1976, pp. 21–29.
38. Bažant, Z., & Shieh, C., "Hysteretic fracturing endochronic theory for concrete", *Journal of the Engineering Mechanics Division-Asce*, Vol. 106, No. 5, 1980, pp. 929–950.
39. Patzák, B., "Object oriented finite element modeling", *Acta Polytechnica*, Vol. 39, No. 1,

1999, pp. 99–113.
40. Patzák, B., & Bittnar, Z., "Design of object oriented finite element code", *Advances in Engineering Software*, Vol. 32, No. 1, 2001, pp. 759–767.

This page intentionally contains only this sentence.

Grassl, P.; Rempling, R. (2008).
A damage-plasticity interface approach to the meso-scale modelling of concrete subjected to cyclic compressive loading.
Engineering Fracture Mechanics. 75 (16) pp. 4804–4818.

This page intentionally contains only this sentence.

Engineering Fracture Mechanics 75 (2008) 4804–4818

Contents lists available at ScienceDirect

Engineering Fracture Mechanics

journal homepage: www.elsevier.com/locate/engfracmech

A damage-plasticity interface approach to the meso-scale modelling of concrete subjected to cyclic compressive loading

Peter Grassl [a,*], Rasmus Rempling [b]

[a] University of Glasgow, Department of Civil Engineering, Glasgow, UK
[b] Chalmers University of Technology, Department of Civil and Environmental Engineering, Göteborg, Sweden

ARTICLE INFO

Article history:
Received 9 March 2008
Received in revised form 10 June 2008
Accepted 19 June 2008
Available online 1 July 2008

Keywords:
Concrete
Fracture
Cyclic loading
Compression
Damage mechanics
Plasticity
Meso-scale

ABSTRACT

Concrete is characterised by stiff inclusions in a soft matrix separated by weak interfacial transition zones (ITZs). Subjected to cyclic loading, this material exhibits a strongly nonlinear response, which is characterised by the occurrence of hysteresis loops. Furthermore, for cyclic loading, failure may occur before the equivalent strength for monotonic loading is reached. The present work investigates, whether the occurrence of permanent displacements in different phases of the meso-structure of quasi-brittle heterogeneous materials, such as concrete, leads to damage evolution during repeated loading.

A new three-dimensional interface model based on a combination of damage mechanics and the theory of plasticity is proposed, which allows one to control the ratio of permanent and total inelastic displacements. The model is based on only a few material parameters, which can be directly determined by experiments.

The interface model is applied to the plane-stress analysis of an idealised heterogeneous material with cylindrical inclusions and ITZs subjected to cyclic compressive stresses.

1. Introduction

The mechanical response of quasibrittle heterogeneous materials, such as concrete, is complex and strongly nonlinear. Many of the nonlinearities are caused by the heterogeneity of the material characterised by stiff inclusions in a soft matrix separated by weak interfacial transition zones (ITZ). Debonding and slip between inclusions and matrix, as well as cracks and shear bands in the matrix and inclusions can contribute to the nonlinear fracture process of these heterogeneous materials. For repeated mechanical loading, the stress–strain curves exhibit hysteresis loops and failure may occur before the equivalent strength for monotonic loading is reached [1–14].

Over the last 30 years many phenomenological macroscopic constitutive models for the mechanical response of concrete subjected to cyclic and repeated loading have been developed. Selected examples are bounding surface models [15–20], models with viscosity [21] and specially designed damage and damage-plasticity models [22–25]. Although many of these macroscopic approaches can describe the hysteresis loops and the fatigue of concrete, our knowledge of the mechanisms of hysteresis loops and concrete fatigue is still limited, since the models are phenomenological.

A better understanding of the mechanics of concrete subjected to cyclic loading might be obtained by studying the meso-scale behaviour of the material. The meso-scale of concrete can be idealised by stiff inclusions and a soft matrix separated by weak ITZs. Each of the three phases has a complex heterogeneous microstructure, which again requires numerical modelling by means of phenomenological models or multiscale analysis in which the mechanical response of the three phases is determined by their microstructure [26–28]. Meso-scale approaches to modelling fracture of heterogeneous quasi-brittle

* Corresponding author. Tel.: +44 141 330 5208; fax: +44 141 330 4557.
E-mail address: grassl@civil.gla.ac.uk (P. Grassl).

0013-7944/$ - see front matter © 2008 Elsevier Ltd. All rights reserved.
doi:10.1016/j.engfracmech.2008.06.005

materials can be divided into continuum models, discrete models and combinations of the two. In previous decades, many discrete and continuum/discrete hybrid models were proposed for the modelling of fracture [29–42], with only a few studies focused on the damage evolution under repeated loading.

The present study investigates, whether the occurrence of permanent displacements in different phases of the meso-structure of quasi-brittle heterogeneous materials leads to damage evolution during repeated loading. For this, an interface model is required which allows one to control the ratio of permanent and total inelastic displacements in the different phases. A suitable framework for such a model is the combination of damage mechanics and the theory of plasticity [43–45]. Thus, the aim of the present work is to develop a damage-plasticity interface constitutive model, which permits one to describe accurately the ratio of permanent and total inelastic displacements. The model should be based on only few material parameters, which could be directly determined by experiments. Furthermore, it is intended to demonstrate the influence of localised permanent displacements on the damage evolution for repeated loading of heterogeneous materials. The interface model itself does not exhibit any hysteresis loops for unloading and reloading. Instead the hysteresis loops and the damage evolution should be modelled as a structural effect caused by localised permanent displacements.

2. Damage-plasticity interface model

In the present section the new interface model based on a combination of damage mechanics and the theory of plasticity is presented. The model is discussed in detail in Section 3.

A three-dimensional displacement jump $\mathbf{u}_c = (u_n, u_s, u_t)^T$ at an interface is considered, which is transformed into strains $\boldsymbol{\varepsilon} = (\varepsilon_n, \varepsilon_s, \varepsilon_t)^T$ by means of the length h as

$$\boldsymbol{\varepsilon} = \frac{\mathbf{u}_c}{h} \tag{1}$$

The three subscripts n, s and t denote the normal and two tangential directions in the local coordinate system of the interface (Fig. 1a). The length h is the thickness of the interface (Fig. 1b).

The strains are related to the nominal stress $\boldsymbol{\sigma} = (\sigma_n, \sigma_s, \sigma_t)^T$ as

$$\boldsymbol{\sigma} = (1-\omega)\mathbf{D}_e(\boldsymbol{\varepsilon} - \boldsymbol{\varepsilon}_p) = (1-\omega)\bar{\boldsymbol{\sigma}} \tag{2}$$

where ω is the damage variable, $\mathbf{D}_e$ is the elastic stiffness, $\boldsymbol{\varepsilon}_p = (\varepsilon_{pn}, \varepsilon_{ps}, \varepsilon_{pt})^T$ is the plastic strain and $\bar{\boldsymbol{\sigma}}$ is the effective stress. The elastic stiffness is

$$\mathbf{D}_e = \begin{Bmatrix} E & 0 & 0 \\ 0 & \gamma E & 0 \\ 0 & 0 & \gamma E \end{Bmatrix} \tag{3}$$

where E and γ are model parameters controlling both Young's modulus and Poisson's ratio of the material.

The plasticity model is based on the effective stress and thus independent of damage. The model is described by the yield function (Eq. (4)), the flow rule (Eq. (5)), the evolution law for the hardening variable (Eq. (6)) and the loading unloading conditions (Eq. (7)):

$$f = F(\bar{\boldsymbol{\sigma}}, \kappa) \tag{4}$$

$$\dot{\boldsymbol{\varepsilon}}_p = \dot{\lambda}\frac{\partial g}{\partial \bar{\boldsymbol{\sigma}}} \tag{5}$$

$$\dot{\kappa} = \dot{\lambda} h_\kappa \tag{6}$$

$$f \leqslant 0, \quad \dot{\lambda} \geqslant 0, \quad \dot{\lambda} f = 0 \tag{7}$$

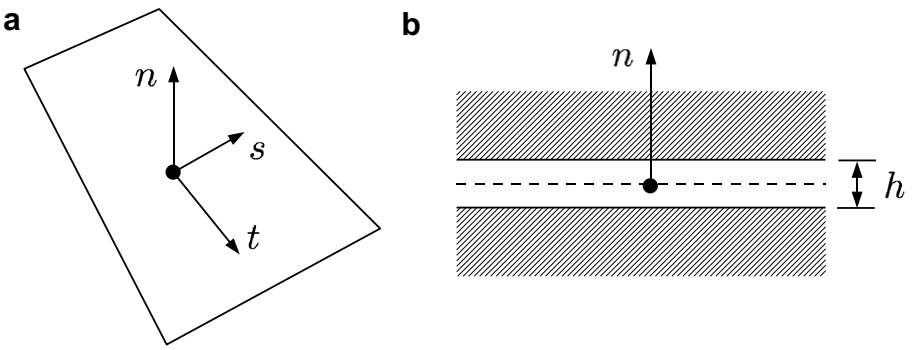

Fig. 1. Interface. (a) Tangential plane of interface. (b) Cross-section of interface.

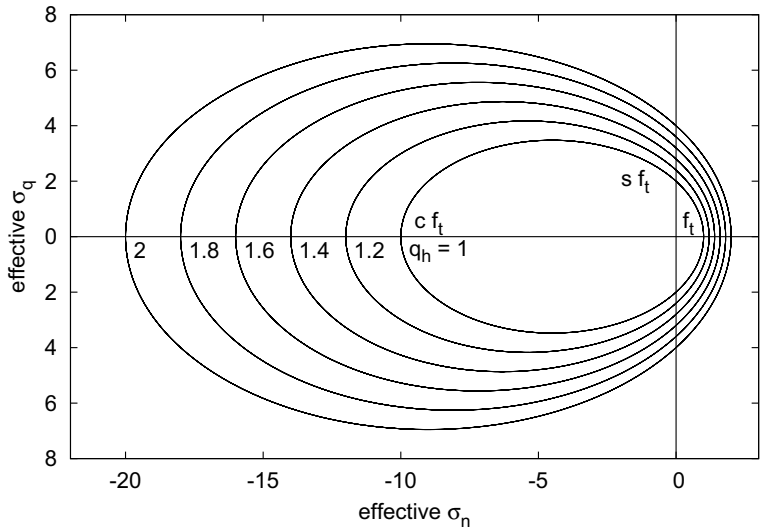

Fig. 2. Evolution of the yield surface. Yield surfaces for q_h = 1, 1.2, 1.4, 1.6, 1.8 and 2 formulated in the effective stress space are shown. For q_h = 1 the three parameters are f_t = 1, sf_t = 2f_t and cf_t = 10f_t.

Here, f is the yield function, κ is the plastic hardening variable, g is the plastic potential, h_κ is the evolution law for the hardening parameter and $\dot{\lambda}$ is the rate of the plastic multiplier. The yield surface ($f = 0$), shown in Fig. 2, which is a function of two stress variables σ_n and $\sigma_q = \sqrt{\sigma_s^2 + \sigma_t^2}$, is defined as

$$f = \sigma_n^2 + \sigma_n q(c-1) f_t + \sigma_q^2 \frac{c}{s} - c f_t^2 q^2 = 0 \tag{8}$$

where f_t is the interfacial tensile strength, and s and c are the ratios of shear and tensile, and compressive and tensile strength, respectively. Furthermore, q is the hardening law defined as

$$q = 1 + H_p \kappa \tag{9}$$

where

$$H_p = \frac{E(1-\mu) - \frac{f_t^2}{2G_{ft}} h}{\mu f_t} \tag{10}$$

The model parameter μ controls the ratio of permanent and total inelastic strains, and G_{ft} is the fracture energy in uniaxial tension defined as the area under the linear stress-crack opening curve (Fig. 3).

The function h_κ in the evolution law of the plastic hardening parameter in Eq. (6) is chosen, for reasons described below, as

$$h_\kappa = \sqrt{\langle m_1 \rangle^2 + \left(\frac{m_2}{\psi}\right)^2 + \left\langle -\frac{m_1}{\psi} \right\rangle^2} \tag{11}$$

where $m_1 = \frac{\partial g}{\partial \sigma_n}$, $m_2 = \sqrt{\frac{\partial g}{\partial \sigma_s}^2 + \frac{\partial g}{\partial \sigma_t}^2}$ and

$$\psi = \frac{c G_{fc}(f_t^2 h + 2E G_{ft}(\mu - 1))}{G_{ft}(c^2 f_t^2 h + 2E G_{fc}(\mu - 1))} \tag{12}$$

The parameter G_{fc} in Eq. (12) is the fracture energy under compression.

Finally, the damage parameter

$$\omega = \frac{f_t h \kappa_{d1} + 2G_{ft}(q-1)}{2G_{ft} q - f_t h \kappa_{d2}} \tag{13}$$

in Eq. (2) is defined by the two history variables κ_{d1} and κ_{d2}.

The history variable κ_{d1} is defined incrementally by the rate equation

$$\dot{\kappa}_{d1} = \sqrt{\langle \dot{\varepsilon}_{pn} \rangle^2 + \frac{\dot{\varepsilon}_{ps}^2 + \dot{\varepsilon}_{pt}^2}{\xi_1^2} + \frac{\langle -\dot{\varepsilon}_{pn} \rangle^2}{\xi_1^2}} \tag{14}$$

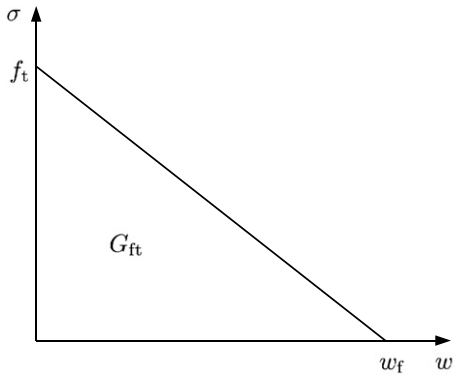

Fig. 3. Linear softening law: nominal stress σ versus inelastic displacement w for uniaxial tension. The stress is reduced to zero at the critical crack opening w_f.

where

$$\xi_1 = \frac{G_{fc}}{G_{ft} c} \tag{15}$$

The second history variable is defined as

$$\dot{\kappa}_{d2} = \dot{q} \frac{f_t}{E \xi_2} \tag{16}$$

with the initial condition

$$\kappa_{d2} = \frac{f_t}{E \xi_2} \tag{17}$$

and

$$\xi_2 = \frac{\sqrt{\langle \dot{\varepsilon}_{pn} \rangle^2 + \frac{\xi_1^2 \left(\dot{\varepsilon}_{ps}^2 + \dot{\varepsilon}_{pt}^2 \right)}{c^2} + \frac{\xi_1^2 \langle -\dot{\varepsilon}_{pn} \rangle^2}{c^2}}}{\| \dot{\boldsymbol{\varepsilon}}_p \|} \tag{18}$$

The implementation and thermodynamical validity of the proposed model is described in Appendices A and B.

3. Discussion of the interface model

The proposed damage-plasticity interface model is calibrated by 8 input parameters. The elastic response is determined by the parameters E and γ, which are explicitly related to the elastic macroscopic Young's modulus E_m and Poisson's ratio ν for regular arrangements of lattice elements [46]. The strength envelope is defined by the tensile strength f_t, shear strength sf_t and compressive strength cf_t. The inelastic deformations are controlled by the fracture energies G_{ft} and G_{fc} for uniaxial tension and uniaxial compression, respectively. Furthermore, the amount of permanent inelastic strains is controlled by the factor μ. These parameters are determined from tensile, shear and compressive tests of the material phases.

In the following, the meaning of the model parameters μ is illustrated for the case of pure tension and compression. For $\sigma_q = 0$, the yield surface in Eq. (8) has the form

$$\sigma_n^2 + \sigma_n q (c - 1) f_t - c f_t^2 q^2 = 0 \tag{19}$$

For pure tension ($\sigma_n > 0$), this quadratic equation gives

$$f = \sigma_n - f_t q = 0 \tag{20}$$

According to Eqs. (5) and (6), the rates of the only non-zero plastic strain rate component $\dot{\varepsilon}_{pn}$ and the rate of the hardening parameter $\dot{\kappa}$ are

$$\dot{\varepsilon}_{pn} = \dot{\kappa} = \dot{\lambda} \tag{21}$$

The consistency conditions ($\dot{f} = 0$) has the form

$$\dot{f} = \dot{\sigma}_n - f_t \dot{q} = E \left(\dot{\varepsilon}_n - \dot{\lambda} \right) - f_t H_p \dot{\lambda} = 0 \tag{22}$$

which gives with H_p in Eq. (10) the rate of the plastic multiplier

$$\dot{\lambda} = \frac{2\dot{\varepsilon}_n E G_{ft} \mu}{2EG_{ft} - f_t^2 h} \tag{23}$$

Hence, the total plastic strain for a monotonic increase of $\varepsilon_n > f_t/E$ is

$$\varepsilon_{pn} = \frac{2(\varepsilon_n E - f_t) G_{ft} \mu}{2EG_{ft} - f_t^2 h} \tag{24}$$

The first history variable κ_{d1} is equal to the plastic strain ε_{pn}, since $\varepsilon_{ps} = \varepsilon_{pt} = 0$ (Eq (14)). The second history variable κ_{d2} in Eq. (16) is

$$\kappa_{d2} = \frac{f_t}{E}(1 + H_p \varepsilon_{pn}) = \varepsilon_n - \varepsilon_{pn} \tag{25}$$

For $\omega = 1$, Eq. (13) gives

$$\frac{2G_{ft}}{f_t h} = \kappa_{d1} + \kappa_{d2} \tag{26}$$

With $\kappa_{d1} = \varepsilon_{pn}$ and $\kappa_{d2} = \varepsilon_n - \varepsilon_{pn}$, this reduces to

$$\frac{2G_{ft}}{f_t h} = \varepsilon_n \tag{27}$$

Hence, the ratio of the plastic strain in Eq. (24) and the total inelastic strain for $\omega = 1$ in Eq. (27) is

$$\frac{\varepsilon_{pn}}{\varepsilon_n} = \mu \tag{28}$$

Thus, the parameter μ determines the ratio of the plastic strain and total inelastic strain in uniaxial tension, which can be determined from a tensile experiment with unloading close to complete failure ($\omega \approx 1$). The parameter μ is independent of the interface thickness h, which is achieved by introducing h in the expression of H_p in Eq. (10).

Now, the case of pure compression ($\sigma_n < 0$ and $\sigma_q = 0$) is considered. The yield surface in Eq. (8) gives

$$f = \sigma_n + c f_t q = 0 \tag{29}$$

The plastic strain rate is

$$\dot{\varepsilon}_{pn} = -\dot{\lambda} \tag{30}$$

The hardening parameter, according to Eqs. (6) and (11), is equal to

$$\dot{\kappa} = \dot{\lambda} h_\kappa = \frac{\dot{\lambda}}{\psi} \tag{31}$$

The consistency condition $\dot{f} = 0$ has the form

$$\dot{f} = \dot{\sigma}_n + c f_t \dot{q} = E(\dot{\varepsilon}_n + \dot{\lambda}) + c f_t H_p \frac{\dot{\lambda}}{\psi} = 0 \tag{32}$$

which gives with H_p in Eq. (10) and ψ in Eq. (12)

$$\dot{\lambda} = -\frac{E\dot{\varepsilon}_n}{E + \frac{c f_t H_p}{\psi}} = -\frac{2\dot{\varepsilon}_n E G_{fc} \mu}{2EG_{fc} - c^2 f_t^2 h} \tag{33}$$

The total plastic strain for a monotonic decrease of $\varepsilon_n < -c f_t/E$ is

$$\varepsilon_{pn} = \frac{2(\varepsilon_n E + c f_t) G_{fc} \mu}{2EG_{fc} - c^2 f_t^2 h} \tag{34}$$

The history variables κ_{d1} and κ_{d2} have the form

$$\kappa_{d1} = -\frac{\varepsilon_{pn}}{\xi_1} = -\frac{2c(\varepsilon_n E + c f_t) G_{ft} \mu}{2EG_{fc} - c^2 f_t^2 h} \tag{35}$$

and

$$\kappa_{d2} = \frac{f_t}{E\xi_2}\left(1 + H_p \frac{(-\varepsilon_{pn})}{\psi}\right) = -\frac{c G_{ft} \varepsilon_n}{G_{fc}} + \frac{2c G_{ft} \mu (\varepsilon_n E + c f_t)}{2EG_{fc} - c^2 f_t^2 h} \tag{36}$$

For the compression case, Eq. (13) reduces to

$$\frac{2G_{ft}}{f_t h} = \kappa_{d1} + \kappa_{d2} = -\frac{c\varepsilon_n G_{ft}}{G_{fc}} \tag{37}$$

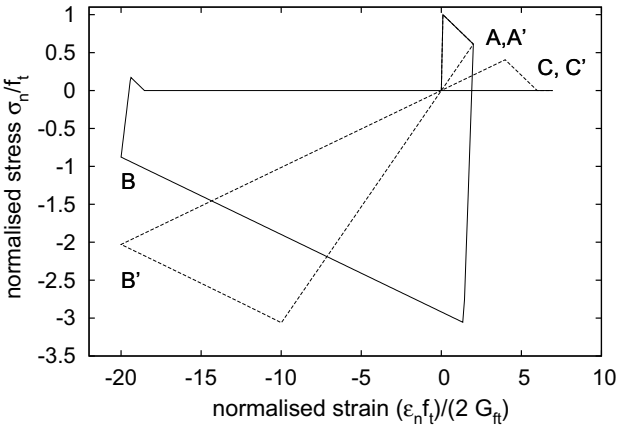

Fig. 4. Stress–strain response for fluctuating normal strains for $\mu = 1$ (solid line) and $\mu = 0$ (dashed line).

Hence, for $\omega = 1$ the inelastic strain is equal to the total strain

$$\varepsilon_n = -\frac{2G_{fc}}{cf_t h} \tag{38}$$

The ratio of plastic strain in Eq. (34) and inelastic strain in Eq. (38) is

$$\frac{\varepsilon_p}{\varepsilon_n} = \mu \tag{39}$$

Again, the model parameter μ controls the ratio of plastic and total inelastic strain. For compression this ratio is more difficult to determine experimentally, since the post-peak response in uniaxial compression in experiments is strongly influenced by the boundary conditions. Therefore, the model was constructed so that this ratio is the same for uniaxial tension and compression. Combinations of normal and shear loading are modelled by Eqs. (12), (15) and (18).

The constitutive response of the interface model is demonstrated by the stress–strain response for fluctuating normal strains for $\mu = 1$ and $\mu = 0$ (Fig. 4). The normal strain is increased to point A (A'). Then the strain is reduced to point B (B') and again increased to point C (C'). The parameter μ controls the amount of plastic strains. For $\mu = 0$ a pure damage-mechanics response is obtained and the stress–strain curve is unloaded to the origin. For $\mu = 1$, on the other hand, a pure plasticity model is obtained. The unloading is elastic and the compressive strength is reached sooner than for $\mu = 0$. However, the magnitude of the compressive strength is similar for $\mu = 1$ and $\mu = 0$, since the plasticity model is based on the effective stress.

4. Two-dimensional analysis of heterogeneous materials subjected to cyclic loading

The interface model is applied to the two-dimensional plane stress analysis of an idealised heterogeneous material, which consists of inclusions, matrix and interfacial transition zones separating the inclusions and the matrix. The present analyses should be extended to 3D analysis in future work, since the two-dimensional analysis is a strong idealisation of the response of concrete subjected to compression. A special lattice-type model developed by Refs. [29,47,33] is used to discretise the domain. The domain is decomposed into polygons by means of the Voronoi tesselation [48] (Fig. 5a). The lattice elements connect the nodes of the polygons.

Each node possesses two translations and one rotation shown in the local coordinate system in Fig. 6. The degrees of freedom $\mathbf{u}_e = \{u_1, v_1, \phi_1, u_2, v_2, \phi_2\}^T$ of the two nodes of the lattice element are related to the displacement discontinuities $\mathbf{u}_c = \{u_c, v_c\}^T$ at the mid-point C of the interface by

$$\mathbf{u}_c = \mathbf{B}\mathbf{u}_e \tag{40}$$

where

$$\mathbf{B} = \begin{bmatrix} -1 & 0 & e & 1 & 0 & -e \\ 0 & -1 & -h_e/2 & 0 & 1 & -h_e/2 \end{bmatrix} \tag{41}$$

In Eq. (41), the variable h_e is the element length and e is the eccentricity, defined as the distance between the mid-points of the lattice element and the corresponding polygon facet (Fig. 5).

In the present work, the element length h_e was chosen to be equal to the interface thickness h introduced in Eq. (1).

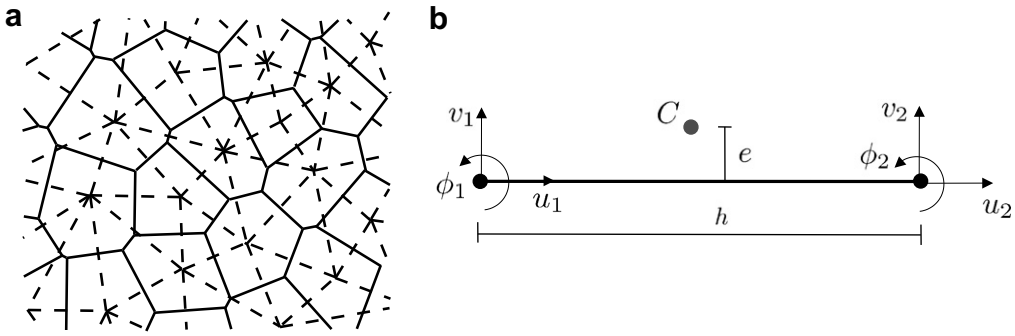

Fig. 5. Discretisation: (a) Lattice elements (dashed lines) connecting nodes within Voronoi cells (solid lines). (b) Degrees of freedom μ_1, v_1, ϕ_1, μ_2, v_2 and ϕ_2 of the lattice element of length h in the local coordinate system. The point C at which the interface model is evaluated is in the center of the polygon facet at a distance e from the center of the lattice element.

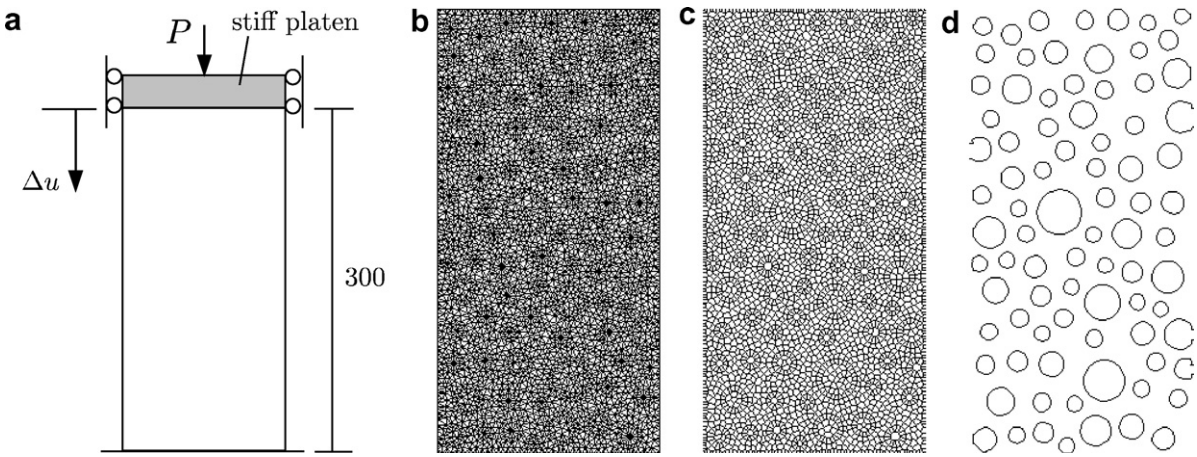

Fig. 6. Test specimens. (a) Geometry and loading setup, (b) lattice, (c) Voronoi polygons and (d) boundaries of the inclusions.

The displacements $\mathbf{u}_c$ at the point C are transformed into strains $\boldsymbol{\varepsilon} = \{\varepsilon_n, \varepsilon_s\}^T = \mathbf{u}_c / h_e$ (Fig. 5b). The strain $\boldsymbol{\varepsilon}$ is related to the stress $\boldsymbol{\sigma} = \{\sigma_n, \sigma_s\}^T$ by means of the two-dimensional version ($\sigma_t = 0$) of the damage-plasticity interface model presented earlier. The element stiffness is

$$\mathbf{K}_e = \frac{A}{h_e} \mathbf{B}^T \mathbf{D} \mathbf{B} \tag{42}$$

where A is the length of the facet.

The nodes of the lattice elements are placed sequentially in the domain to be analysed. The coordinates of each node are determined randomly and a minimum distance $d_m = 3$ mm is enforced iteratively between the nodes [30]. For this iterative process, the number of nodes n for a chosen domain A_d and the minimum distance d_m determine the distribution of lengths of lattice elements. This relationship can be expressed in the form of a density

$$\rho = \frac{n d_m^2}{A_d} \tag{43}$$

For a regular arrangement of lattice elements resulting in equilateral triangles, the density results in $\rho = \sqrt{3}/2$. In the present study a smaller density of $\rho = 0.6$ was used.

The resulting irregular arrangement of lattice elements is more suitable for fracture analysis, since the fracture patterns obtained are less sensitive to the arrangement of the lattice elements [49,50]. This is also known from continuum models [51,52].

Table 1
Model parameters

	E (GPa)	γ	f_t (MPa)	q	c	G_{ft} (J/m^2)	G_{fc}
Matrix	30	0.33	5	2	20	400	400000
ITZ	48	0.33	1	2	20	80	80000
Inclusion	120	0.33	–	–	–	–	–

The meso-structure of the heterogeneous material is discretised by lattice elements perpendicular to the boundary between the cylindrical inclusions and the matrix. The diameters of the inclusions are determined randomly from a cumulative distribution function of the occurrence of the inclusion diameter d. A pseudo-random number generator is used to generate

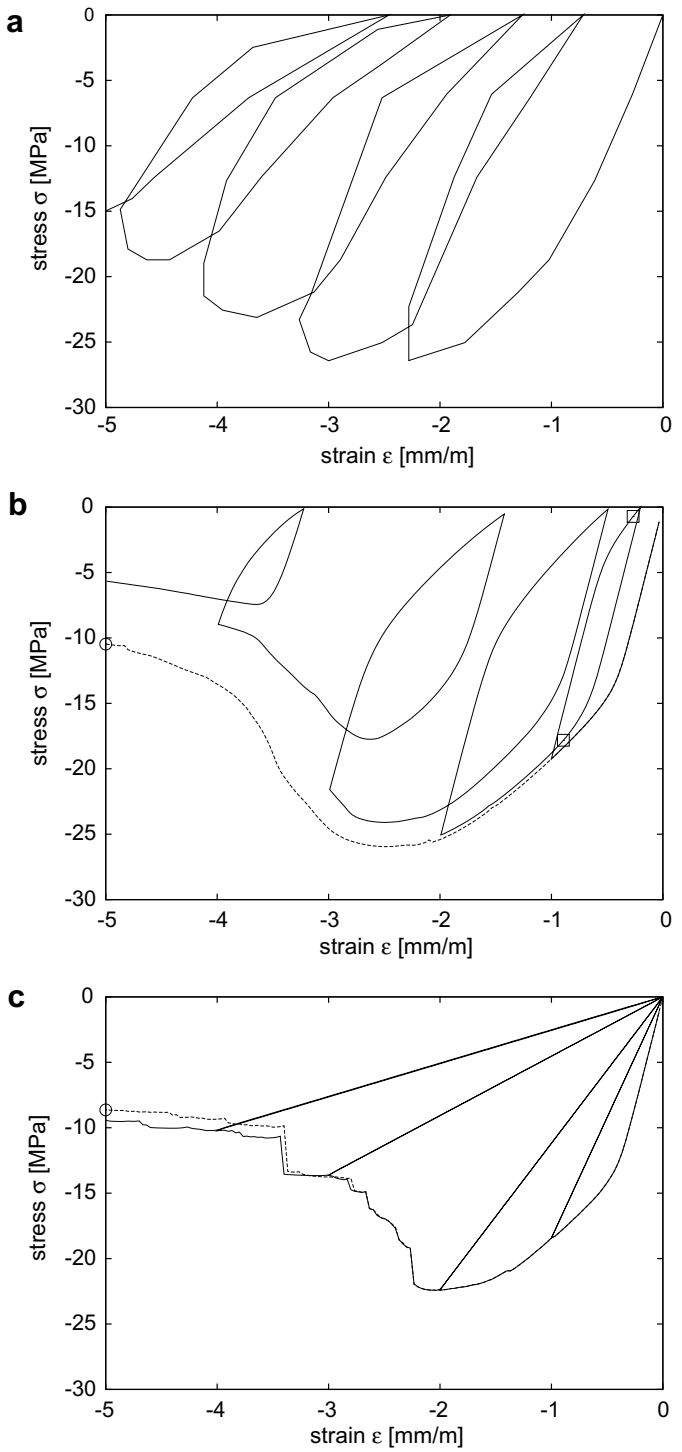

Fig. 7. (a) Experimental results reported in [2]. Stress–strain response obtained from the analysis for (b) $\mu = 1$ and (c) $\mu = 0$ for monotonic (dashed line) and cyclic loading (solid line). Open circles in (b) and (c) mark the stages of the loading process for which the deformation patterns are shown in Fig. 8. Open squares in (b) mark the stages in the first hysteresis loops for which the crack patterns are shown in Fig. 9.

probabilities from which the diameter d is determined. This procedure is repeated until the chosen volume fraction ρ_a of circular inclusions is reached. The inclusions are placed sequentially by means of randomly generated coordinates within the area of the specimen. For each set of generated coordinates, it is checked that no overlap with previously placed inclusions occurs. However, overlap with boundaries is permitted, i.e. no boundary effect is considered. In the present analysis, the inclusion distribution was obtained with a maximum and minimum diameter $d_{max} = 32$ mm, $d_{min} = 10$ mm, respectively, and a aggregate volume fraction $\rho_a = 0.3$.

The geometry, loading setup and the mesh of the plane stress analyses are shown in Fig. 6. The analyses were controlled by the top displacement Δu_m. The strain in the axial direction is defined as $\varepsilon_m = \Delta u_m/L$, where L is the height of the specimen. The axial stress is defined as $\sigma_m = P/A_m$, where P is the axial force and A_m is the cross-section of the specimen. Furthermore, the lateral expansion and rotation of the specimen ends was chosen to be restrained.

Three different types of analyses were performed. Firstly, the specimen was subjected to a uniform compressive load controlled by the top displacement Δu_m. Secondly, the strain was increased in steps to $\varepsilon_m = 1\%, 2\%, 3\%, 4\%$, with the strain being reversed after each step so that $\sigma_m = 0$. Finally, the specimen was subjected to a fluctuating compressive stress σ_m with a mean compressive strength of $0.5\, f_{cm}$ and an amplitude of $0.3 f_{cm}$, where f_{cm} is the macroscopic compressive strength of the material. The values $\mu = 1$ and $\mu = 0$ were used to simulate materials with different ratios of permanent and total inelastic displacements. For simplicity, the plastic potential was chosen to be equal to the yield surface $f = g$. All other material parameters were kept constant according to Table 1. The stiffness of the elastic inclusions was chosen to be four times greater than the stiffness of the matrix. The stiffness of the lattice elements crossing the ITZ is the mean of the stiffness of the matrix and the inclusions assuming that the size of the ITZ is significantly smaller than the size of the lattice elements. Furthermore, the

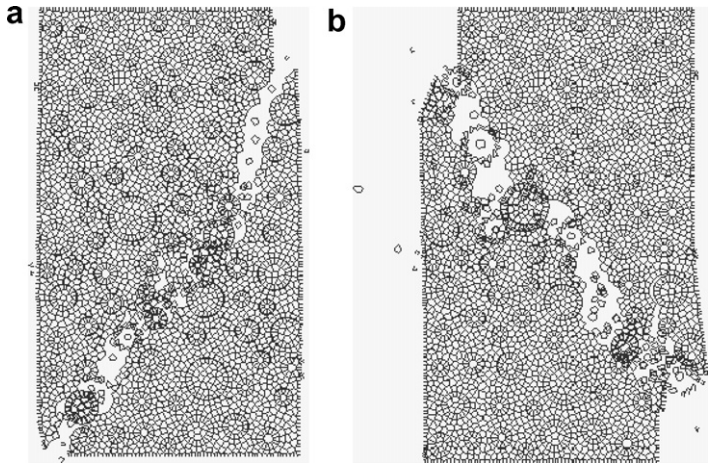

Fig. 8. Deformations magnified by a factor of five shown in the form of Voronoi polygons for (a) $\mu = 1$ and (b) $\mu = 0$ for the monotonic loading marked by open circles in Fig. 7a and b.

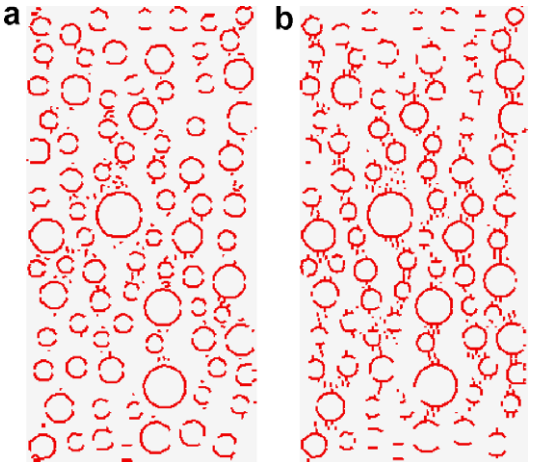

Fig. 9. Active cracks for an (a) unloading and (b) reloading stage in the first hysteresis loop marked in Fig. 7a by open squares for $\mu = 1$. Black lines mark polygon facets at which the damage variable increases at this stage of the analysis. For $\mu = 0$ no active cracks are visible.

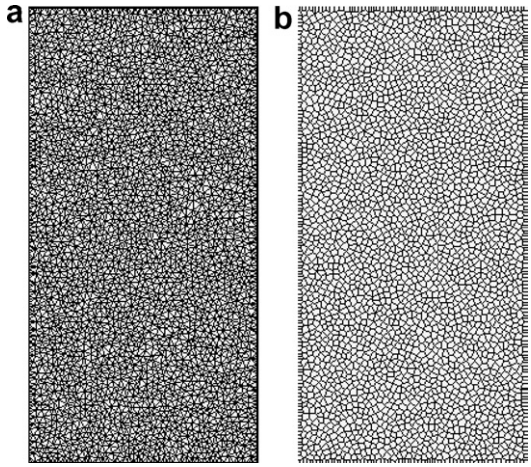

Fig. 10. (a) Lattice and (b) Voronoi polygons for the test specimen without inclusions.

strength and fracture energy of the ITZ are five times less than of the matrix. The parameter $\gamma = 0.33$ corresponds to a Poisson's ratio of $\nu = 0.25$ for the case of a regular lattice [46]. The tensile fracture energy of the matrix G_{ft} is greater than normally used for concrete, since the two-dimensional analysis results in a less ductile response than a 3D analysis [40].

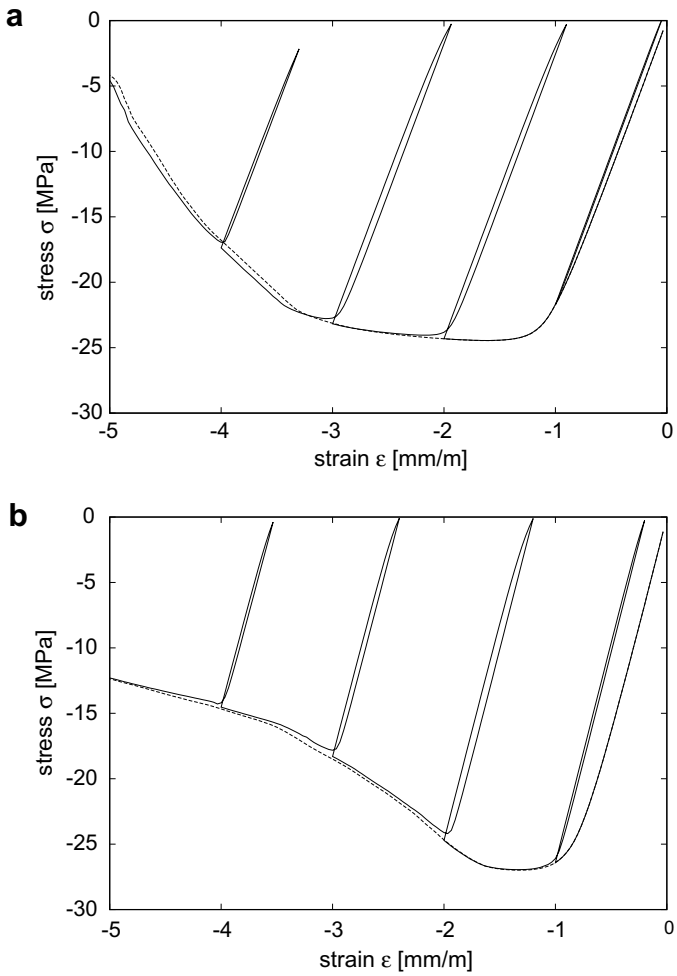

Fig. 11. Stress–strain response without (a) inclusions and (b) ITZs for monotonic (dashed line) and cyclic loading (solid line) for $\mu = 1$. The tensile strength of the matrix was reduced to 2.1 MPa.

Experimental results reported in [2] are shown in Fig. 7a. The stress–strain responses for monotonic and cyclic loading for $\mu = 1$ and $\mu = 0$ are presented in Fig. 7b and c. The deformation patterns for the post-peak stage for the monotonic loading marked in Fig. 7 are shown in Fig. 8. Furthermore, crack patterns are shown in Fig. 9 for the unloading and reloading in the first loop of the cyclic analysis in Fig. 7.

The monotonic response for $\mu = 1$ exhibits a greater strength and peak strain than the monotonic response for $\mu = 0$. This difference is caused by the presence of volumetric–deviatoric coupling provided by the plasticity part of the present damage-plasticity interface model [51]. Plastic flow in the shear direction leads to normal plastic strains, which, if restrained, activate normal compressive stresses. These normal compressive stresses increase the shear capacity.

For $\mu = 1$, the stress–strain response shows strong hysteresis loops during unloading and reloading (Fig. 7a). The cyclic loading leads to a reduction of the capacity of the structure so that the strength envelope obtained from the monotonic compression test cannot be reached. The crack patterns in Fig. 9a show that the fracture process evolves during unloading and reloading.

On the other hand, for $\mu = 0$, no hysteresis loops are visible in Fig. 7b and the unloading occurs to the origin. No active cracks are visible during unloading and reloading. These results indicate that the hysteresis loops obtained with $\mu = 1$ are caused by localised permanent displacements.

Two additional analyses were carried out to strengthen this hypothesis. Firstly, a specimen of the geometry shown in Fig. 6a without inclusions and ITZs was analysed with $\mu = 1$. Secondly, an analysis with inclusions (Fig. 6d), but without ITZs, was analysed with $\mu = 1$.

The materials without ITZs are expected to be stronger but more brittle than the three-phase material. Hence, the tensile strength of the matrix material was reduced to $f_t = 2.1$ MPa to reduce the elastic energy stored in the material and to avoid numerical problems in the post-peak regime of the analyses. All other parameters are the same as in Table 1. The mesh for the first analysis is shown in Fig. 10. For the analysis with inclusions, the mesh shown in Fig. 6b was used. The stress–strain

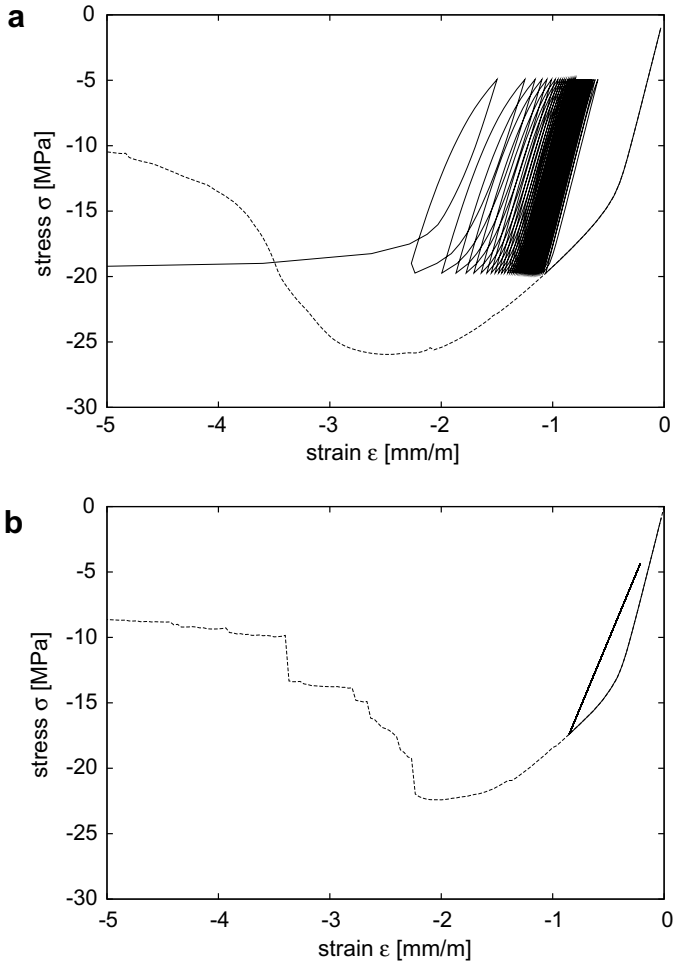

Fig. 12. Stress–strain response obtained from fatigue analysis compared to monotonic analysis for (a) $\mu = 1$ and (b) $\mu = 0$.

responses for cyclic loading (Fig. 11) exhibits significant permanent displacements, but no hysteresis loops. Hence, the hysteresis loops for the case with inclusions in Fig. 7a are caused by localised permanent displacements.

In addition, a fluctuating compressive stress was applied with a mean compressive stress of $0.5f_{cm}$ and an amplitude of $0.3f_{cm}$, where f_{cm} is the macroscopic compressive strength obtained from the monotonic analysis. The material parameters in Table 1 were used. The stress–strain responses $\mu = 1$ and $\mu = 0$ are compared to the monotonic responses in Fig. 12. For $\mu = 1$, failure of the specimen is obtained after 45 fluctuations. On the other hand, for $\mu = 0$ no fracture evolution is visible after 90 fluctuations.

5. Conclusions

In the present work, a new damage-plasticity interface model was proposed which enables one to control the ratio of permanent and reversible inelastic displacement occurring during the fracture process. The eight model parameters are directly related to physical quantities.

The interface model was applied to the plane-stress analysis of an idealised heterogeneous material with cylindrical inclusions and ITZ subjected to cyclic compressive stresses. The meso-scale approach with the new interface model results in realistic failure patterns in the form of shear bands, as it is known from materials such as concrete. The amount of localised permanent displacements has a strong influence on the material response for repeated loading. With localised permanent displacements, the stress–strain curves are characterised by hysteresis loops and damage evolves during repeated loading. Without ITZs the permanent displacements do not localise. Thus, for this case no hysteresis loops and no damage evolution during repeated loading is obtained. Furthermore, without permanent displacement, unloading occurs to the origin and neither hysteresis loops nor damage evolution during repeated loading can be obtained.

Hence, the proposed interface model has the potential to model the cyclic response of heterogeneous materials by means of a meso-scale approach, since the interface model permits one to control the ratio of permanent and total inelastic displacements. Current work focuses on a detailed study of the influences of the other model parameters on the response of concrete subjected to cyclic loading [53] and an extension of the meso-scale analysis to triaxial stress states.

Acknowledgement

The simulations were performed with the object-oriented finite elementpackage OOFEM [54,55] extended by the present authors. The mesh has been prepared with the mesh generator Triangle [56].

Appendix A. Thermodynamical aspects

The response of concrete in cyclic compression is characterised by hysteresis loops that occur during repeated unloading and reloading. During these loading cycles, energy is dissipated. Macroscopic models, which describe these loops phenomenologically have to be carefully designed to ensure thermodynamical admissibility. The present modelling approach is different since the loops are a structural result of localised irreversible strains on the constitutive level. Therefore, the unloading and reloading path on the constitutive level is identical, i.e. no hysteresis loops are prescribed. Nevertheless, it is useful to check whether the model satisfies the dissipation inequality.

The free energy of the present damage-plastic model is chosen to be

$$\rho\psi(\boldsymbol{\varepsilon}, \boldsymbol{\varepsilon}_p, \omega) = \frac{1}{2}(1-\omega)(\boldsymbol{\varepsilon} - \boldsymbol{\varepsilon}_p)\mathbf{D}_e(\boldsymbol{\varepsilon} - \boldsymbol{\varepsilon}_p) \tag{44}$$

Here, ρ is the density (specific mass) and ψ is the Helmholtz free energy per unit mass. Furthermore, isothermal processes are considered, so that the temperature remains constant and is not explicitly listed among the state variables.

The dissipation rate per unit volume is defined as

$$\dot{D} = \boldsymbol{\sigma}\dot{\boldsymbol{\varepsilon}} - \rho\dot{\psi} = \boldsymbol{\sigma}\dot{\boldsymbol{\varepsilon}} - \left(\frac{\partial\rho\psi}{\partial\boldsymbol{\varepsilon}}\dot{\boldsymbol{\varepsilon}} + \frac{\partial\rho\psi}{\partial\boldsymbol{\varepsilon}_p}\dot{\boldsymbol{\varepsilon}}_p + \frac{\partial\rho\psi}{\partial\omega}\dot{\omega}\right) \tag{45}$$

The derivative of the free energy with respect to the strain results in the stress–strain relation

$$\frac{\partial\rho\psi}{\partial\boldsymbol{\varepsilon}}\dot{\boldsymbol{\varepsilon}} = (1-\omega)(\boldsymbol{\varepsilon} - \boldsymbol{\varepsilon}_p)\mathbf{D}_e\dot{\boldsymbol{\varepsilon}} = \boldsymbol{\sigma}\dot{\boldsymbol{\varepsilon}} \tag{46}$$

Therefore, the dissipation rate in Eq. (45) reduces to

$$\dot{D} = \dot{D}^p + \dot{D}^d = \frac{\partial\rho\psi}{\partial\boldsymbol{\varepsilon}_p}\dot{\boldsymbol{\varepsilon}}_p + \frac{\partial\rho\psi}{\partial\omega}\dot{\omega} \tag{47}$$

where the term

$$\dot{D}^p = \frac{\partial\rho\psi}{\partial\boldsymbol{\varepsilon}_p}\dot{\boldsymbol{\varepsilon}}_p = (1-\omega)(\boldsymbol{\varepsilon} - \boldsymbol{\varepsilon}_p)\mathbf{D}_e\dot{\boldsymbol{\varepsilon}}_p \tag{48}$$

and

$$\dot{D}^{\mathrm{d}} = \frac{\partial \rho\psi}{\partial\omega}\dot{\omega} = \frac{1}{2}(\boldsymbol{\varepsilon} - \boldsymbol{\varepsilon}_{\mathrm{p}})\mathbf{D}_{\mathrm{e}}(\boldsymbol{\varepsilon} - \boldsymbol{\varepsilon}_{\mathrm{p}})\dot{\omega} \tag{49}$$

are the plastic and damage dissipation, respectively. The damage dissipation in Eq. (49) is always positive, since the rate of the damage parameter ω is defined to be positive. For $f = g$, the plastic dissipation

$$\dot{D}^{\mathrm{p}} = (1-\omega)(\boldsymbol{\varepsilon} - \boldsymbol{\varepsilon}_{\mathrm{p}})\,\mathbf{D}_{\mathrm{e}}\,\dot{\boldsymbol{\varepsilon}}_{\mathrm{p}} = \dot{\lambda}(1-\omega)\bar{\boldsymbol{\sigma}}\frac{\partial f}{\partial \bar{\boldsymbol{\sigma}}} \tag{50}$$

fulfils Drucker's postulate and is guaranteed to be positive as well.

Appendix B. Implementation

The constitutive model has been implemented within the lattice framework. The continuous loading process is replaced by incremental time steps. In each step, the boundary value problem (global level) and integration of the constitutive laws (local level) are solved. For the boundary value problem on the global level, the usual incremental-iterative solution strategy is used, either in the form of the standard Newton–Raphson iteration with the algorithmic tangent stiffness, or in the modified form with the tangent stiffness replaced by the secant stiffness

$$\mathbf{D}_{\mathrm{s}} = (1-\omega)\mathbf{D}_{\mathrm{e}} \tag{51}$$

In the former case, the convergence rate is quadratic, but divergence may occur in steps, during which localisation of the inelastic deformation occurs. On the other hand, the secant stiffness is more robust. However, the convergence rate is only linear.

For the local problem, the updated values of the stress and the internal variables at the end of the step are obtained by a fully implicit integration of the rate form of the constitutive equations, starting from their known values are the beginning of the step and applying the given strain increment $\Delta\boldsymbol{\varepsilon} = \boldsymbol{\varepsilon}^{n+1} - \boldsymbol{\varepsilon}^{n}$. The integration scheme is divided into two sequential steps, corresponding to the plastic and damage parts of the model. In the plastic part, the plastic strain $\boldsymbol{\varepsilon}_{\mathrm{p}}$ and the effective stress $\boldsymbol{\sigma}$ at the end of step are obtained.

The plasticity part of the integration scheme is based on an elastic trial and a plastic corrector step. At the end of the step the following residuals should vanish

$$\mathbf{R}_1 = -\boldsymbol{\varepsilon}_{\mathrm{p}}^{(n+1)} + \boldsymbol{\varepsilon}_{\mathrm{p}}^{(n)} + \Delta\lambda\frac{\partial g}{\partial \bar{\boldsymbol{\sigma}}} \tag{52}$$

$$R_2 = -\kappa^{(n+1)} + \kappa^{(n)} + \Delta\lambda h_{\kappa}^{(n+1)} \tag{53}$$

$$f^{(n+1)} = f(\bar{\boldsymbol{\sigma}}^{(n+1)}, \Delta\lambda, \kappa^{(n+1)}) \tag{54}$$

The iterative change of the plastic strain is related to the iterative change of the stress by the linear relation

$$-\delta\boldsymbol{\varepsilon}_{\mathrm{p}} = \mathbf{D}_{\mathrm{e}}^{-1}\delta\bar{\boldsymbol{\sigma}} \tag{55}$$

The linearisation of the residuals in Eqs. (52)–(54) around the state $(n+1)$ leads to the following set of linear equations for the unknown iterative corrections $\delta\bar{\boldsymbol{\sigma}}$ and $\delta\kappa$:

$$\mathbf{R}_1 + \mathbf{D}_{\mathrm{e}}^{-1}\delta\bar{\boldsymbol{\sigma}} + \delta\lambda\frac{\partial g}{\partial\bar{\boldsymbol{\sigma}}} + \Delta\lambda\left(\frac{\partial^2 g}{\partial\bar{\boldsymbol{\sigma}}^2} + \frac{\partial^2 g}{\partial\bar{\boldsymbol{\sigma}}\partial\kappa}\right) = 0 \tag{56}$$

$$R_2 - \delta\kappa + \delta\lambda h_{\kappa} + \Delta\lambda\left(\frac{\partial h_{\kappa}}{\partial\bar{\boldsymbol{\sigma}}} + \frac{\partial h_{\kappa}}{\partial\kappa}\right) = 0 \tag{57}$$

$$f + \frac{\partial f}{\partial\bar{\boldsymbol{\sigma}}}\delta\bar{\boldsymbol{\sigma}} + \frac{\partial f}{\partial\kappa}\delta\kappa = 0 \tag{58}$$

Using the first two equations, the iterative correction $\delta\bar{\boldsymbol{\sigma}}$ and $\delta\kappa$ can be expressed in terms of the correction of the plastic multiplier, $\delta\lambda$:

$$\begin{Bmatrix}\delta\bar{\boldsymbol{\sigma}}\\ \delta\kappa\end{Bmatrix} = -\boldsymbol{\Xi}\left(\begin{Bmatrix}\mathbf{R}_1\\ R_2\end{Bmatrix} + \delta\lambda\begin{Bmatrix}\frac{\partial g}{\partial\bar{\boldsymbol{\sigma}}}\\ h_{\kappa}\end{Bmatrix}\right) \tag{59}$$

where the matrix $\boldsymbol{\Xi}$ is defined as

$$\boldsymbol{\Xi} = \begin{pmatrix}\mathbf{D}_{\mathrm{e}}^{-1} + \Delta\lambda\frac{\partial^2 g}{\partial\bar{\boldsymbol{\sigma}}^2} & \Delta\lambda\frac{\partial^2 g}{\partial\bar{\boldsymbol{\sigma}}\partial\kappa}\\ \Delta\lambda\frac{\partial h_{\kappa}}{\partial\bar{\boldsymbol{\sigma}}} & -1 + \Delta\lambda\frac{\partial h_{\kappa}}{\partial\kappa}\end{pmatrix}^{-1} \tag{60}$$

Substituting Eq. (59) into Eq. (58) and solving for the correction of the plastic multiplier, we obtain

$$\delta\lambda = \frac{f - \left\{ \frac{\partial f}{\partial \bar{\boldsymbol{\sigma}}} \quad h_\kappa \right\} \boldsymbol{\Xi} \left\{ \begin{matrix} \mathbf{R}_1 \\ R_2 \end{matrix} \right\}}{\left\{ \frac{\partial f}{\partial \bar{\boldsymbol{\sigma}}} \quad \frac{\partial f}{\partial \kappa} \right\} \boldsymbol{\Xi} \left\{ \begin{matrix} \frac{\partial f}{\partial \bar{\boldsymbol{\sigma}}} \\ h_\kappa \end{matrix} \right\}} \tag{61}$$

In Eqs. (56)–(61) the superscript $(n+1)$ was omitted since all terms in question are evaluated at $(n+1)$. The corrections $\delta\ldots$ in Eq. (59) are used to update the cumulative increments $\Delta\ldots$ and the final values at the end of the step. The iteration is repeated until the residuals $\mathbf{R}_1^{(n+1)}$, $R_2^{(n+1)}$ and $f^{(n+1)}$ vanish.

The integration of the damage part is very efficient since the rate forms of the two history variables κ_{d1} and κ_{d2} are evaluated without an iterative procedure. Once the history variables are determined, the damage parameter ω is evaluated and the nominal stress is computed as

$$\boldsymbol{\sigma} = (1-\omega)\bar{\boldsymbol{\sigma}} \tag{62}$$

The algorithmic stiffness is determined by differentiating the stress-return algorithm with respect to the strain increment [57]. We consider an incremental step from the initial strain $\boldsymbol{\varepsilon}^n$ to the final strain $\boldsymbol{\varepsilon} = \boldsymbol{\varepsilon}^n + \Delta\boldsymbol{\varepsilon}$, for which the stress-evaluation procedure provides the final stress $\boldsymbol{\sigma}$. If the strain increment is changed by $\delta\boldsymbol{\varepsilon}$, the step from $\boldsymbol{\varepsilon}^{(n)}$ to $\boldsymbol{\varepsilon}^{(n)} + \Delta\boldsymbol{\varepsilon} + \delta\boldsymbol{\varepsilon}$ leads to the final stress $\boldsymbol{\sigma}$. The aim is to find $\delta\boldsymbol{\sigma}$ on $\delta\boldsymbol{\varepsilon}$ provided that $\delta\boldsymbol{\varepsilon}$ is infinitesimal but $\Delta\boldsymbol{\varepsilon}$ is finite. The change of the nominal stress

$$\delta\boldsymbol{\sigma} = (1-\omega)\delta\bar{\boldsymbol{\sigma}} - \bar{\boldsymbol{\sigma}}\delta\omega \tag{63}$$

follows from the linearised form of Eq. (2).

The change $\delta\bar{\boldsymbol{\sigma}}$ is determined from Eq. (59) and the change of of the damage parameter $\omega = g_d(\kappa_{d1}, \kappa_{d2})$ results in

$$\delta\omega = \frac{\mathrm{d}g_d}{\mathrm{d}\kappa_{d1}} \frac{\mathrm{d}\kappa_{d1}}{\mathrm{d}\boldsymbol{\varepsilon}_p} \delta\boldsymbol{\varepsilon}_p + \frac{\mathrm{d}g_d}{\mathrm{d}\kappa_{d2}} \left(\frac{\mathrm{d}\kappa_{d2}}{\mathrm{d}\boldsymbol{\varepsilon}} \delta\boldsymbol{\varepsilon} + \frac{\mathrm{d}\kappa_{d2}}{\mathrm{d}\kappa} \delta\boldsymbol{\kappa} \right) \tag{64}$$

where $\delta\kappa$ is determined from Eq. (59) and $\delta\boldsymbol{\varepsilon}_p$ is obtained from Eq. (55).

References

[1] Karsan ID, Jirsa JO. Behavior of concrete under compressive loadings. J Struct Div – ASCE 1969;95:2543–63.
[2] Sinha BP, Gerstle KH, Tulin LG. Stress–strain relations for concrete under cyclic loading. J Am Concrete Institute 1964;61:195–211.
[3] Buyukozturk O, Teng T. Concrete in biaxial cyclic compression. J Struct Eng 1984;110(3):461–76.
[4] Gopalaratnam VS, Shah SP. Softening response of plain concrete in direct tension. ACI J Proc 1985;82(3).
[5] Mier JGM van. Fracture of concrete under complex stress. HERON 1986;31(3):1–90.
[6] Cornelissen HAW, Hordijk DA, Reinhardt HW. Experimental determination of crack softening characteristics of normalweight and lightweight concrete. HERON 1986;31(2):45–56.
[7] Yankelevsky DZ, Reinhardt HW. Response of plain concrete to cyclic tension. ACI Mater J 1987;84(5).
[8] Zhen-Hai G, Xiu-Qin Z. Investigation of complete stress–deformation curves for concrete in tension. ACI Mater J 1987;84(4).
[9] Hordijk DA, Reinhardt HW. Numerical and experimental investigation into the fatigue behavior of plain concrete. Exp Mech 1993;33(4):278–85.
[10] Gao L, Hsu CTT. Fatigue of concrete under uniaxial compression cyclic loading. ACI Mater J 1998;95(5).
[11] Gettu R, Aguado A. Damage in high-strength concrete due to monotonic and cyclic compression – a study based on splitting tensile strength. ACI Mater J 1996;93(6).
[12] Lee YH, William K. Mechanical properties of concrete in uniaxial compression. ACI Mater J 1997;94(6).
[13] Subramaniam KV, Popovics JS, Shah SP. Fatigue response of concrete subjected to biaxial stresses in the compression–tension region. ACI Mater J 1999;96(6).
[14] Lee MK, Barr BIG. An overview of the fatigue behaviour of plain and fibre reinforced concrete. Cement Concrete Composites 2004;26(4):299–305.
[15] Yang BL, Dafalias YF, Herrmann LP. A bounding surface plasticity model for concrete. J Engng Mech – ASCE 1985;111:359–80.
[16] Voyiadjis GZ, Abu-Lebdeh TM. Damage model for concrete using bounding surface concept. J Engng Mech – ASCE 1993;119:865–1885.
[17] Abu-Lebdeh TM, Voyiadjis GZ. Plasticity-damage model for concrete under cyclic multiaxial loading. J Engng Mech – ASCE 1993;119:1465–84.
[18] Voyiadjis GZ, Abu-Lebdeh TM. Plasticity model for concrete using the bounding surface concept. Int J Plasticity 1994;10:1–24.
[19] Winnicki A, Cichon C. Plastic model for concrete in plane stress state. I.: theory. J Engng Mech – ASCE 1998;124:591–602.
[20] Pandolfi A, Taliercio A. Bounding surface models applied to fatigue of plain concrete. J Engng Mech – ASCE 1998;124:556–64.
[21] Lee HJ, Kim YR. Viscoelastic constitutive mode for asphalt concrete under cyclic loading. J Engng Mech – ASCE 1998;124:32–40.
[22] Papa E, Taliercio A. Anisotropic damage model for the multiaxial static and fatigue behaviour of plain concrete. Engng Fract Mech 1996;55(2):63–179.
[23] Ragueneau F, La Norderie C, Mazars J. Damage model for concrete-like materials coupling cracking and friction, contribution towards structural damping: first uniaxial applications. Mech Cohesive-Frictional Mater 2000;5:607–25.
[24] Nguyen O, Repetto EA, Ortiz M, Radovitzky RA. A cohesive model of fatigue crack growth. Int J Fract 2001;110(4):351–69.
[25] Desmorat R, Ragueneau F, Pham H. Continuum damage mechanics for hysteresis and fatigue of quasi-brittle materials and structures. Int J Anal Numer Meth Geomech 2007;31:307–29.
[26] Budiansky B, O'Connell RJ. Elastic moduli of a cracked solid. Int J Solid Struct 1976;12(2):81–97.
[27] Heukamp FH, Lemarchand E, Ulm FJ. The effect of interfacial properties on the cohesion of highly filled composite materials. Int J Solid Struct 2005;42(1):287–305.
[28] Dormieux L, Kondo D, Ulm FJ. Microporomechanics. Wiley; 2006.
[29] Kawai T. New element models in discrete structural analysis. J Soc Naval Arch Jpn 1977;141:187–93.
[30] Zubelewicz A, Bažant ZP. Interface modeling of fracture in aggregate composites. J Engng Mech – ASCE 1987;113:1619–30.
[31] Schlangen E, van Mier JGM. Simple lattice model for numerical simulation of fracture of concrete materials and structures. Mater Struct 1992;25:534–42.
[32] Laurenco PB, Rots JG. Multisurface interface model for analysis of masonry structures. J Engng Mech – ASCE 1997;123:660–8.
[33] Bolander JE, Saito S. Fracture analysis using spring networks with random geometry. Engng Fract Mech 1998;61:569–91.
[34] Ueda T, Sato Y, Kakuta Y, Tadokoro T. A study on crack propagation in concrete under cyclic loading. Fract Mech Concrete Struct 1998;1:655–63.

[35] Ortiz M, Pandolfi A. Finite-deformation irreversible cohesive elements for three-dimensional crack-propagation analysis. Int J Numer Meth Eng 1999;44:1267–82.
[36] Bolander JE, Hong GS, Yoshitake K. Structural concrete analysis using rigid-body-spring networks. J Comp Aided Civil Infrastruct Eng 2000;15:120–33.
[37] Carol I, Lopez CM, Roa O. Micromechanical analysis of quasi-brittle materials using fracture-based interface elements. Int J Numer Meth Eng 2001;52:193–215.
[38] de Borst R. Some recent issues in computational failure mechanics. Int J Numer Meth Eng 2001;52(1/2):63–96.
[39] Han T, Ural A, Chen C, Zehnder AT, Ingraffea AR, Billington SL. Delamination buckling and propagation analysis of honeycomb panels using a cohesive element approach. Int J Fract 2002;115:101–23.
[40] Lilliu G, van Mier JGM. 3D lattice type fracture model for concrete. Engng Fract Mech 2003;70:927–41.
[41] Willam K, Rhee I, Shing B. Interface damage model for thermomechanical degradation of heterogeneous materials. Comput Meth Appl Mech Eng 2004;193(30-32):3327–50.
[42] van Mier JGM. Multi-scale interaction potentials (F- r) for describing fracture of brittle disordered materials like cement and concrete. Int J Fract 2007;143(1):41–78.
[43] Grassl P, Jirásek M. Damage-plastic model for concrete failure. Int J Solid Struct 2006;43(22-23):7166–96.
[44] Jason L, Huerta A, Pijaudier-Cabot G, Ghavamian S. An elastic plastic damage formulation for concrete: application to elementary tests and comparison with an isotropic damage model. Comput Meth Appl Mech Eng 2006;195(52):7077–92.
[45] Einav I, Houlsby GT, Nguyen GD. Coupled damage and plasticity models derived from energy and dissipation potentials. Int J Solid Struct 2007;44(7-8):2487–508.
[46] Griffiths DV, Mustoe GGW. Modelling of elastic continua using a grillage of structural elements based on discrete element concepts. Int J Numer Meth Eng 2001;50:1759–75.
[47] Morikawa O, Sawamota Y, Kobayashi N. Local fracture analysis of a reinforced concrete slab by the discrete element method. In: Proceedings of the 2nd international conference on discrete element methods. Cambridge, MA, USA: MIT Press; 1993. p. 275–86.
[48] Aurenhammer F. Voronoi diagrams – a survey of a fundamental geometric data structure. ACM Comput Survey 1991;23:345–405.
[49] Jirásek M, Bažant ZP. Particle model for quasibrittle fracture and application to sea ice. J Engng Mech – ASCE 1995;121:1016–25.
[50] Schlangen E, Garboczi EJ. New method for simulating fracture using an elastically uniform random geometry lattice. Int J Engng Sci 1996;34(10):1131–44.
[51] Grassl P, Rempling R. Influence of volumetric–deviatoric coupling on crack prediction in concrete fracture tests. Engng Fract Mech 2007;74:1683–93.
[52] Jirásek M, Grassl P. Evaluation of directional mesh bias in concrete fracture simulations using continuum damage models. Engng Fract Mech 2008;39:1921–43.
[53] Rempling R, Grassl P. Parametric study of the meso-scale modelling of concrete subjected to cyclic compression. Concrete Comput, in press.
[54] Patzák B. Object oriented finite element modeling. Acta Polytechnica 1999;39:99–113.
[55] Patzák B, Bittnar Z. Design of object oriented finite element code. Adv Engng Software 2001;32:759–67.
[56] Shewchuk JR. Triangle: engineering a 2D quality mesh generator and Delaunay triangulator. In: Lin MC, Manocha D, editors. Applied computational geometry: towards geometric engineering. Lecture notes in computer science, vol. 1148. Springer-Verlag; 1996. p. 203–22 [From the First ACM workshop on applied computational geometry].
[57] Jirásek M, Bažant ZP. Inelastic analysis of structures. Chichester: John Wiley and Sons; 2002.

This page intentionally contains only this sentence.

Rempling, R.; Grassl, P. (2008).
A parametric study of the meso-scale modelling of concrete
subjected to cyclic compression.
Computers and concrete. 5 (4) pp. 359–373.

This page intentionally contains only this sentence.

A parametric study of the meso-scale modelling of concrete subjected to cyclic compression

Rasmus Rempling[1] and Peter Grassl[2*]
[1] Chalmers University of Technology, Göteborg, Sweden
[2] University of Glasgow, UK

* Corresponding author.
Address: Department of Civil Engineering, University of Glasgow, United Kingdom
Email: grassl@civil.gla.ac.uk
Phone: +44 141 330 5208
Fax: +44 141 330 4557

Preprint of Computers and Concrete, Vol. 5, Issue 4, pp. 359-373, 2008

Keywords: Concrete, Fracture, Cyclic loading, Compression, Damage mechanics, Plasticity, Meso-scale

Abstract

The present parametric study deals with the meso-scale modelling of concrete subjected to cyclic compression, which exhibits hysteresis loops during unloading and reloading. Concrete is idealised as a two-dimensional three-phase composite made of aggregates, mortar and interfacial transition zones (ITZs). The meso-scale modelling approach relies on the hypothesis that the hysteresis loops are caused by localised permanent displacements, which result in nonlinear fracture processes during unloading and reloading. A parametric study is carried out to investigate how aggregate density and size, amount of permanent displacements in the ITZ and the mortar, and the ITZ strength influence the hysteresis loops obtained with the meso-scale modelling approach.

1 Introduction

Concrete subjected to cyclic compressive loading is characterised by a strongly nonlinear response. Unloading and reloading is accompanied by nonlinear fracture processes on the meso-scale, such as debonding and slip between inclusion and matrix, which result in hysteresis loops [1, 2, 3, 4]. Furthermore, repeated loading of concrete subjected to cyclic loading may lead to failure although the stress applied is below the strength obtained for monotonic loading.

Many phenomenological constitutive models were developed over the last 30 years, which can describe the hysteresis loops and the fatigue strength observed in experiments. Examples are constitutive models based on bounding surface models [5, 6, 7] or special combinations of damage and plasticity [8]. These phenomenological constitutive models have only limited predictive capabilities since they are based on curve fitting and not on the mechanics of the underlying physical processes. Therefore, they cannot predict reliably the response of concrete outside the range of experimental results available.

Recently, the present authors have proposed a damage-plasticity interface model to describe the response

of concrete subjected to cyclic loading [9]. In this approach concrete was idealised as a three phase-composite consisting of aggregates, mortar and interfacial transition zones (ITZs). A special lattice model was used to descretise the different phases [10, 11]. The meso-scale modelling of hysteresis loops and fatigue strength was based on the assumption that the nonlinear fracture processes during unloading and reloading are caused by localised permanent displacements. The amount of permanent displacements was controlled by a damage-plasticity interface model which was applied to the mortar and ITZ phase. Aggregates were assumed to respond elastically. This meso-scale modelling approach may have better predictive qualities than macroscopic phenomenological models, since the macroscopic response can be designed by changing the response of the meso-scale constituents. Nevertheless, each of the three phases has a complex heterogeneous microstructure, which again requires numerical modelling by means of phenomenological models or multiscale analysis in which the mechanical response of the three phases is determined by their micro-structures [12, 13, 14].

In the present work, this meso-scale modelling direction is further pursued and a parametric study is performed to investigate the influence of several model parameters on the description of hysteresis loops. The first two parameters are the volume fraction of aggregates and the aggregate size, which are related to the random discretisation of the composite. Furthermore, three material parameters, which influence the amount of permanent displacements in the mortar and the ITZ and control the ratio of the strength of mortar and interfacial transition zone, are investigated. This parametric study is similar to other parametric studies presented in the literature on the modelling of concrete [15, 16]. Nevertheless, the present work is focused on the meso-scale modelling of concrete subjected to cyclic loading. This is a direction which has not been pursued before to the authors knowledge.

2 Modelling approach

In the present study the response of concrete subjected to cyclic loading is analysed with a damage-plasticity interface model, which was developed in [9]. In the following paragraphs, the modelling approach is briefly reviewed to introduce the parameters, which are investigated in the present study. The interface model relies on a combination of a plasticity model formulated in the effective stress space and isotropic damage mechanics. For the two-dimensional version of the model, the displacement jump $\mathbf{u}_\mathrm{c} = (u_\mathrm{n}, u_\mathrm{s})^T$ at an interface is considered, which is transferred into strains $\boldsymbol{\varepsilon} = (\varepsilon_\mathrm{n}, \varepsilon_\mathrm{s})^T$ by means of the length h as

$$\boldsymbol{\varepsilon} = \frac{\mathbf{u}_\mathrm{c}}{h} \tag{1}$$

The strains are related to the nominal stress $\boldsymbol{\sigma} = (\sigma_\mathrm{n}, \sigma_\mathrm{s})^T$ as

$$\boldsymbol{\sigma} = (1-\omega)\,\mathbf{D}_\mathrm{e}\,(\boldsymbol{\varepsilon} - \boldsymbol{\varepsilon}_\mathrm{p}) = (1-\omega)\,\bar{\boldsymbol{\sigma}} \tag{2}$$

ω is the damage variable, $\mathbf{D}_\mathrm{e}$ is the elastic stiffness, $\boldsymbol{\varepsilon}_\mathrm{p} = (\varepsilon_\mathrm{pn}, \varepsilon_\mathrm{ps})^T$ is the plastic strain and $\bar{\boldsymbol{\sigma}} = (\bar{\sigma}_\mathrm{n}, \bar{\sigma}_\mathrm{s})^T$ is the effective stress. The elastic stiffness is

$$\mathbf{D}_\mathrm{e} = \begin{Bmatrix} E & 0 \\ 0 & \gamma E \end{Bmatrix} \tag{3}$$

where E and γ are model parameters controlling both the Young's modulus and Poisson's ratio of the material.

The small strain plasticity model is based on the effective stress $\bar{\boldsymbol{\sigma}}$ and consists of the yield surface, flow rule, evolution law for the hardening parameter and loading and unloading conditions. A detailed description of the components of the plasticity model is presented in [9]. The initial yield surface is

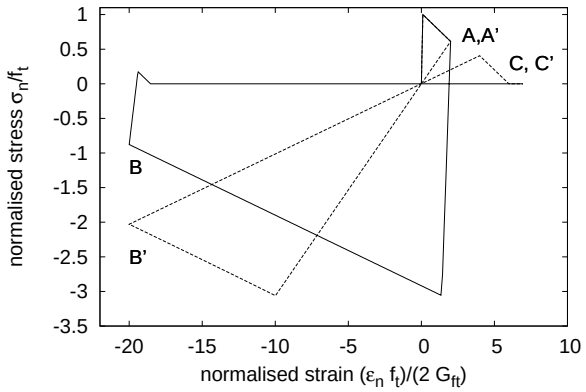

Figure 1: Stress-strain response for fluctuating normal strains for $\mu = 1$ (solid line) and $\mu = 0$ (dashed line).

determined by the tensile strength f_t, by the ratio s of the shear and tensile strength, and the ratio c of the compressive and tensile strength. The evolution of the yield surface during hardening is controlled by the model parameter μ, which is defined as the ratio of permanent and reversible inelastic displacements. The scalar damage part is chosen so that linear stress inelastic displacement laws for pure tension and compression are obtained, which are characterised by the fracture energies G_ft and G_fc.

The eight model parameters E, γ, f_t, s, c, G_ft, G_fc and μ can be determined from a tensile, shear and compressive test of the material phase.

The constitutive response of the interface model is demonstrated by the stress-strain response for fluctuating normal strains for $\mu = 1$ and $\mu = 0$ (Figure 1). The normal strain is increased to point A ($A^{'}$). Then the strain is reduced to point B ($B^{'}$) and again increased to point C ($C^{'}$). The parameter μ controls the amount of plastic strains. For $\mu = 0$ a pure damage-mechanics response is obtained and the stress-strain curve is unloaded to the origin. For $\mu = 1$, on the other hand, a pure plasticity model is obtained. The unloading is elastic and the compressive strength is reached sooner than for $\mu = 0$. However, the magnitude of the compressive strength is similar for $\mu = 1$ and $\mu = 0$, since the plasticity model is based on the effective stress. The constitutive model describes the loss of stiffness and permanent strains, but it does not represent the hysteresis loops for unloading and reloading. Instead, these loops are obtained from the structural analysis, which is discussed in the following section.

The interface model is applied to the two-dimensional plane stress meso-scale analysis of concrete. A special lattice-type model developed by [17, 18, 10] is used to discretise the domain. The domain is decomposed into polygons by means of the Voronoi tessellation [19] (Figure 2a). The lattice elements connect the centroids of the polygons. Each node possesses two translations and one rotation shown in the local coordinate system in Figure 2b. The degrees of freedom $\mathbf{u}_\mathrm{e} = \{u_1, v_1, \phi_1, u_2, v_2, \phi_2\}^\mathrm{T}$ of the two nodes of the lattice element are related to the displacement discontinuities $\mathbf{u}_\mathrm{c} = \{u_\mathrm{c}, v_\mathrm{c}\}^\mathrm{T}$ at the mid-point C of the interface by

$$\mathbf{u}_\mathrm{c} = \mathbf{B}\mathbf{u}_\mathrm{e} \tag{4}$$

where

$$\mathbf{B} = \begin{bmatrix} -1 & 0 & e & 1 & 0 & -e \\ 0 & -1 & -h/2 & 0 & 1 & -h/2 \end{bmatrix} \tag{5}$$

In Eq. (5), the variable h is the element length and e is the eccentricity, defined as the distance between the mid-points of the lattice element and the corresponding polygon facet, respectively (Figure 2). The

displacements $\mathbf{u}_\mathrm{c}$ at the point C are transformed into strains $\boldsymbol{\varepsilon} = \{\varepsilon_\mathrm{n}, \varepsilon_\mathrm{s}\}^T = \mathbf{u}_\mathrm{c}/h$ (Figure 2b). The strain $\boldsymbol{\varepsilon}$ is related to the stress $\boldsymbol{\sigma} = \{\sigma_\mathrm{n}, \sigma_\mathrm{s}\}^T$ by means of the two-dimensional version ($\sigma_\mathrm{t} = 0$) of the damage-plasticity interface model presented earlier. The element stiffness is

$$\mathbf{K}_\mathrm{e} = \frac{A}{h}\mathbf{B}^\mathrm{T}\mathbf{D}\mathbf{B} \tag{6}$$

where A is the length of the facet.

The nodes of the lattice elements are placed sequentially in the domain to be analysed. The coordinates of each node are determined randomly and a minimum distance $d_\mathrm{m} = 3$ mm is enforced iteratively between the nodes [20]. For this iterative process, the number of vertices n for a chosen domain A_d and the minimum distance d_m determine the distribution of lengths of lattice elements. This relationship can be expressed in the form of a density

$$\rho = \frac{n d_\mathrm{m}^2}{A_\mathrm{d}} \tag{7}$$

The resulting irregular arrangement of lattice elements is more suitable for fracture analysis, since the fracture patterns obtained are less sensitive to the arrangement of the lattice elements.

The meso-structure of the heterogeneous material is discretised by lattice elements perpendicular to the boundary between the cylindrical inclusions and the matrix. The diameters of the inclusions are determined randomly from the cumulative distribution function

$$P_\mathrm{f} = \frac{1 - \left(\dfrac{\phi_\mathrm{min}}{d}\right)^{2.5}}{1 - \alpha^{-2.5}} \tag{8}$$

where P_f is the probability of the occurrence of the inclusion diameter d. Furthermore, $\alpha = \phi_\mathrm{max}/\phi_\mathrm{min}$, where ϕ_min and ϕ_max are the minimum and maximum diameters, respectively [21]. A pseudo-random number generator is used to generate probabilities from which the diameter d is determined by means of the inverse of Eq. (8). This procedure is repeated until the chosen volume fraction ρ_a of circular inclusions is reached. The inclusions are placed sequentially by means of randomly generated coordinates within the area of the specimen. For each set of generated coordinates, it is checked that no overlap with previously placed inclusions occurs. However, overlap with boundaries is permitted, i.e. no boundary effect is considered.

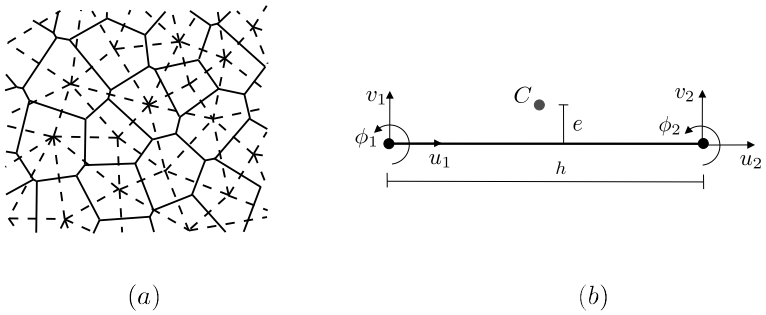

(a) (b)

Figure 2: Discretisation: (a) Lattice elements (dashed lines) connecting centroids obtained with the Voronoi tesselation (solid lines). (b) Degrees of freedom u_1, v_1, ϕ_1, u_2, v_2 and ϕ_2 of the lattice element of length h in the local coordinate system. The point C at which the interface model is evaluated is in the center of the polygon facet at a distance e from the center of the lattice element.

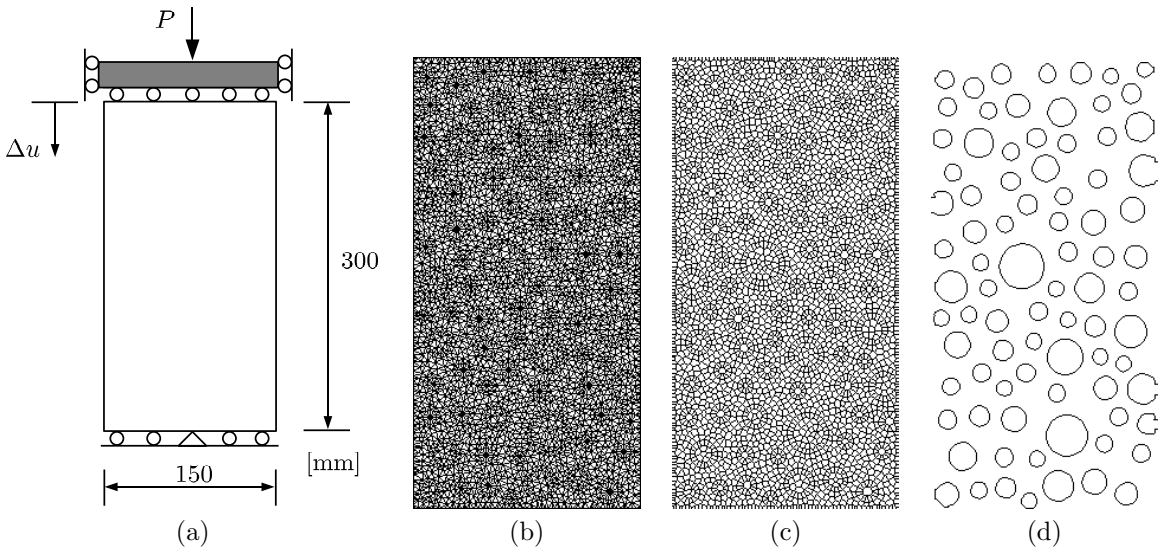

Figure 3: Concrete in uniaxial compression: a) Geometry and loading setup, (b) Lattice (c) Voronoi polygons (d) Boundaries of the inclusions.

Table 1: Model parameters.

Phase	E [GPa]	γ	f_t [MPa]	s	c	G_{ft} [J/mm^2]	G_{fc} [J/mm^2]	μ
Mortar	30	0.33	5	2	20	400	40000	1
Interface	48	0.33	1	2	20	80	8000	1
Aggregate	120	0.33	-	-	-	-	-	-

3 Parametric study

The present parametric study deals with the modelling of concrete subjected to cyclic loading. A three-dimensional concrete cylinder subjected to cyclic uniaxial compression tested by Sinha, Gerstle and Tulin [1] was idealised by means of a two-dimensional meso-scale plane stress model. Concrete was represented by a three-phase composite consisting of mortar, aggregates and interfacial transition zones between the two phases.

The meso-structure was discretised by means of a random lattice based on the Voronoi tesselation of the domain. The mesh was generated with a vertex density of $\rho = 0.6$ and a minimum distance of $d_m = 3$ mm. This vertex density is close to the saturated vertex density which was determined by Bolander and Saito in [10] as $\rho = 0.68$. The aggregate distribution was obtained with $d_{max} = 32$ mm, $d_{min} = 10$ mm and $\rho_a = 0.3$. The geometry, loading setup and one exemplary mesh are shown in Figure 3.

The concrete specimen subjected to monotonic and cyclic compression was analysed with the model parameters shown in Table 1. The axial average stress was determined as $\sigma = P/d$, where P is the axial force, Δu is the axial displacement and d is the width of the specimen. Correspondingly, the axial average strain was defined as $\varepsilon = \Delta u/L$, where L is the height of the specimen. The analysis results in the form of the average stress-strain curves for monotonic and cyclic loading are compared to the experimental results in Figure 4. A reasonable qualitative agreement between the modelling response and the experimental results is obtained. The deformation pattern in the post-peak regime are presented in Figure 5.

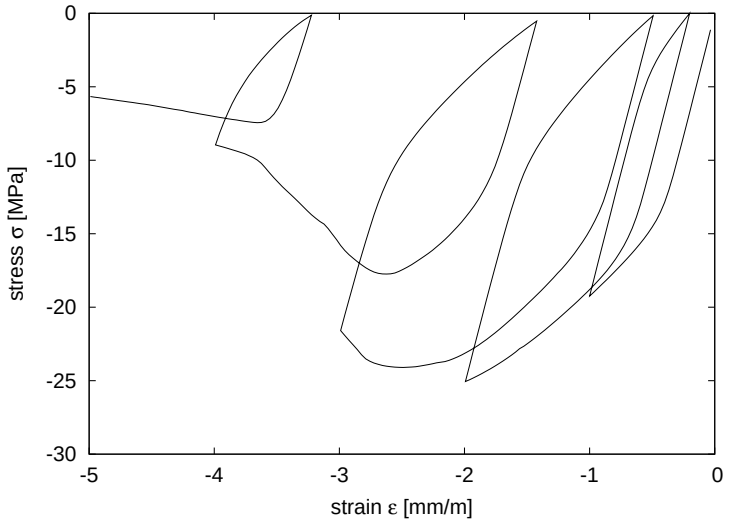

(a)

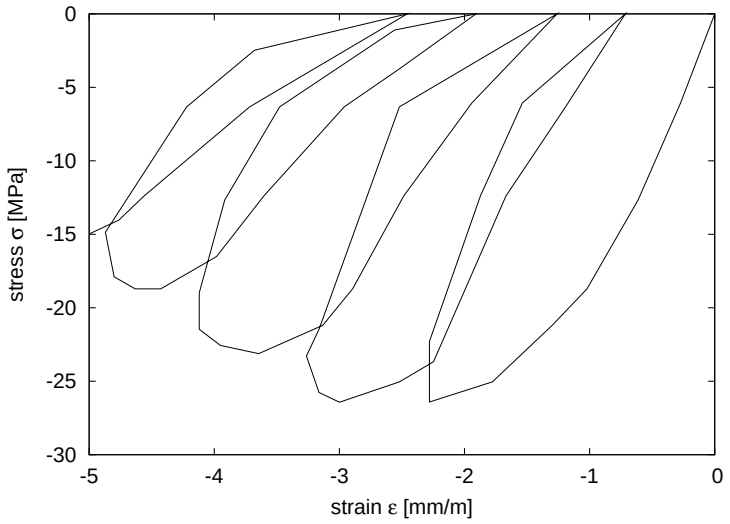

(b)

Figure 4: Stress-strain responses obtained from (a) the meso-scale analysis and from (b) experiments reported in [1].

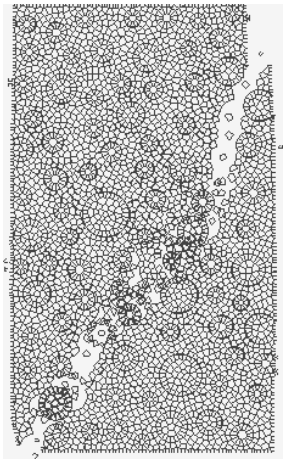

Figure 5: Deformations magnified by a factor of five shown for the monotonic loading.

Five parameters, which are likely to have a strong influence on the modelling of concrete subjected to cyclic loading, are studied:

1. Volume fraction of aggregates.
2. Aggregate size.
3. Ratio of permanent and total inelastic displacements in the ITZ phase.
4. Ratio of permanent and total inelastic displacements in the mortar phase.
5. Ratio of the mortar and interface strength.

The first two parameters, which are related to the aggregate distribution, require random lattice generations. Random meshes and the random positions of the aggregates influence the average stress-strain response. Therefore, the influence of different discretisations on the response of monotonic and cyclic compressive loading is initially analysed by means of five analyses with the same aggregate size and distribution, but with random geometry. The five different meshes are presented in Figure 6.

The response for both monotonic and cyclic compressive loading was analysed. For cyclic loading, the specimens were subjected to four cycles. The strain was increased in steps to $\varepsilon_{\mathrm{m}} = 0.5\%$, 1%, 1.5%, 2%, with the strain being reversed after each step so that $\sigma_{\mathrm{m}} = 0$. The same loading history was applied for all the analyses in the present parametric study. The results for the influence of the random positions of the aggregates and the random orientation of the lattice elements are presented in Figure 7 for monotonic and in Figure 8 for cyclic loading in the form of average stress-strain relations. The random discretisation has a small influence on the pre-peak regime, whereby the peak and post-peak regime is strongly influenced. Nevertheless, the scatter of the simulations is reasonable compared to the one obtained experimentally by van Mier in [3].

The first of the five parameters is the volume fraction ρ_{a}. The response for three volume fractions $\rho_{\mathrm{a}} = 0.3$, 0.15 and 0 were analysed. For $\rho_{\mathrm{a}} = 0$ the resulting, stress-strain curves exhibit snap-back in the post-peak regime. To avoid numerical problems, the tensile strength of the mortar phase was reduced to $f_{\mathrm{t}} = 2.1$ MPa. The other model parameters are the same as in Table 1. The distribution of the randomly placed aggregates is presented in Figure 9.

The average stress-strain response for the different aggregate volume fractions is presented in Figures 10 and 11 for monotonic and cyclic loading, respectively. For the monotonic response, a decrease

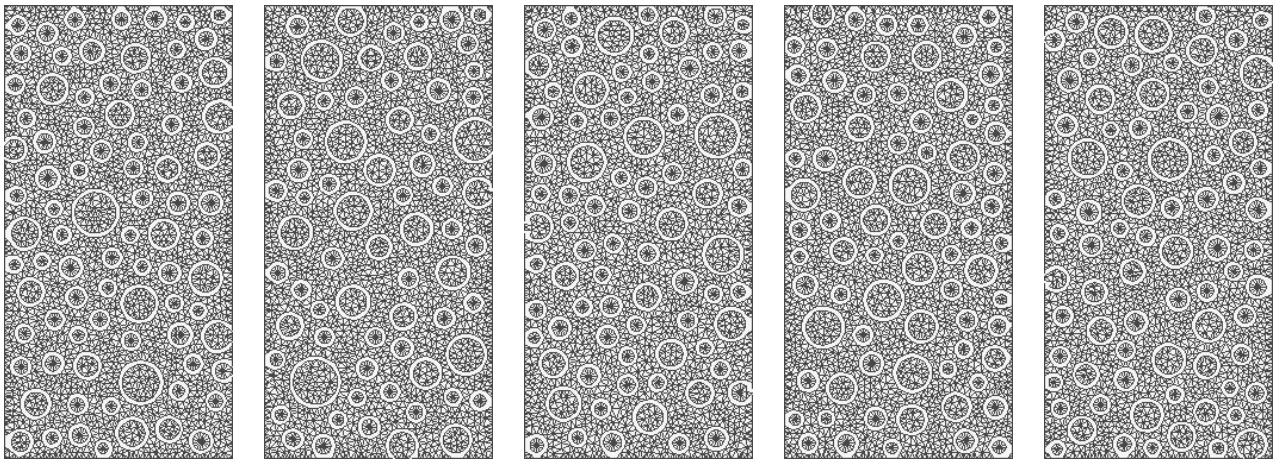

Figure 6: Five random meshes with the same aggregate density and size distribution. Lattice elements which describe the ITZs between aggregates and mortar are not shown to improve the clarity of the illustration.

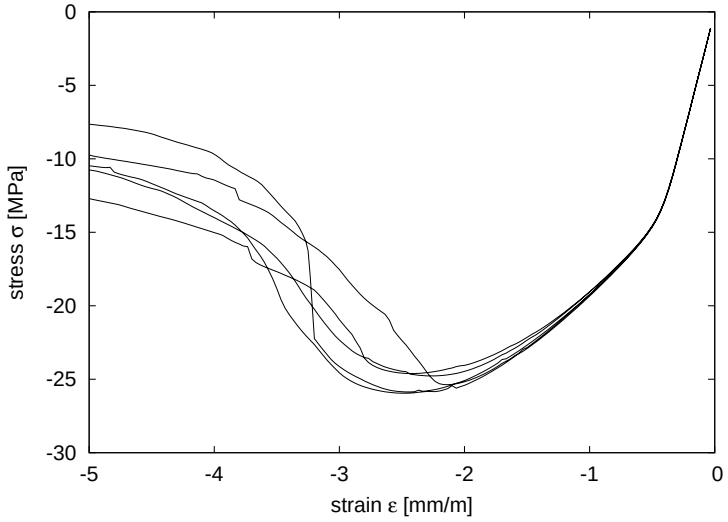

Figure 7: Stress-strain responses obtained for monotonic loading for five meshes with different aggregate arrangements and discretisations.

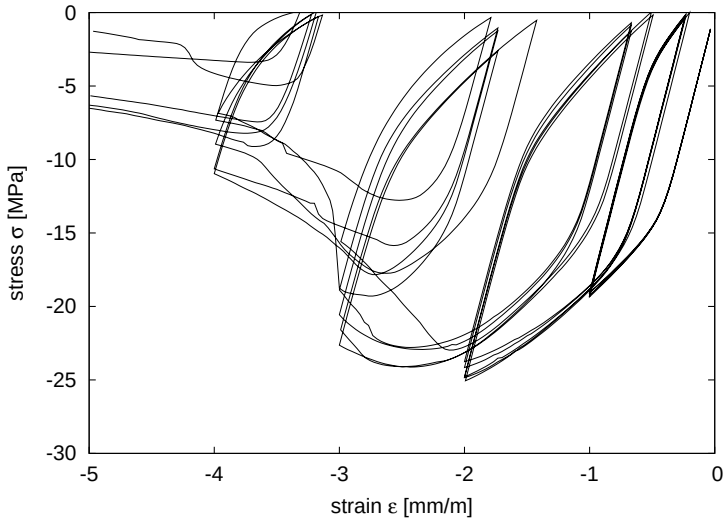

Figure 8: Stress-strain responses obtained for cyclic loading for five meshes with different aggregate arrangements and discretisations.

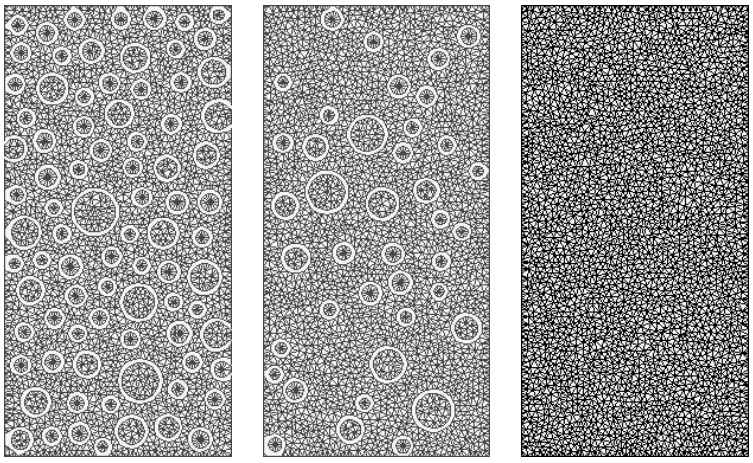

Figure 9: Lattices for aggregate densities of (a) $\rho_{\mathrm{a}} = 0.3$, (b) $\rho_{\mathrm{a}} = 0.15$, (c) $\rho_{\mathrm{a}} = 0$. Lattice elements which describe the interface between aggregates and mortar are not shown to improve the clarity of the illustration.

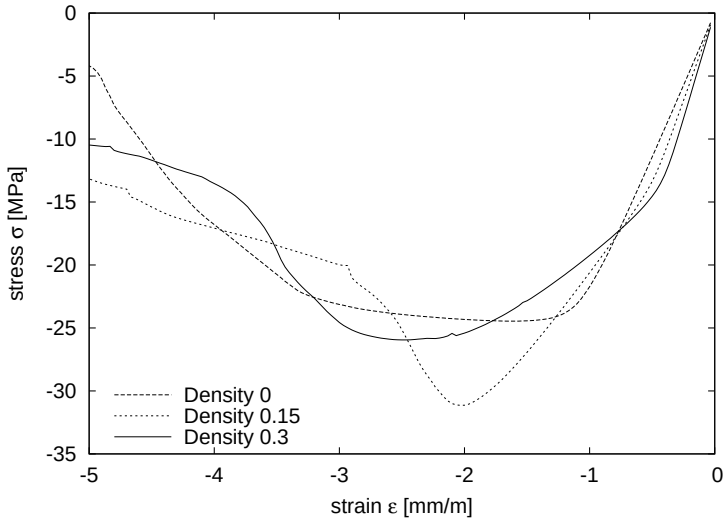

Figure 10: Stress-strain responses for monotonic loading for three aggregate densities of $\rho_{\mathrm{a}} = 0.3$, 0.15 and 0. The tensile strength of the mortar phase for the specimen with $\rho_{\mathrm{a}} = 0$ was reduced to $f_{\mathrm{t}} = 2.1$ MPa to avoid snap-back in the post-peak regime.

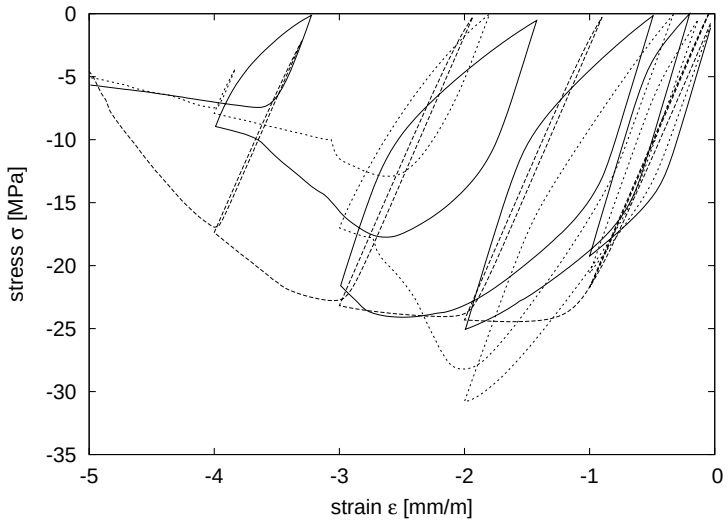

Figure 11: Stress-strain responses for cyclic loading for three aggregates densities $\rho_{\mathrm{a}} = 0.3$, 0.15 and 0. The tensile strength of the mortar phase for the specimen with ρ_{a} was reduced to $f_{\mathrm{t}} = 2.1$ MPa to avoid snap-back in the post-peak regime.

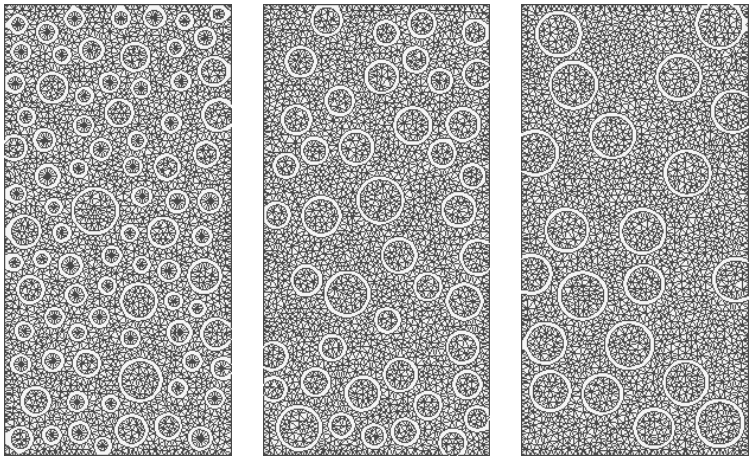

(a) (b) (c)

Figure 12: Lattice elements for the size range of (a) $d_{\max}/d_{\min} = 3.2$, (b) $d_{\max}/d_{\min} = 2.1$, (c) $d_{\max}/d_{\min} = 1.3$.

of the aggregate fraction results in an increase of the compressive strength. This strong influence of the aggregate fraction is explained by the weak interfaces. With an increasing number of interfaces, the strength of the composite is reduced. For the cyclic response, a decrease of the aggregate volume fraction leads to a decrease of the size of the hysteresis loops. The occurrence of hysteresis loops is based on the existence of weak zones, in which permanent displacements localise. If the number of these localised zones of permanent displacements is reduced, the nonlinear fracture processes during unloading and reloading is decreased and the resulting hysteresis loops are smaller.

The second parameter studied is the ratio of the maximum and minimum aggregate size $d_{\max}/d_{\min}$. Three size ratios of $d_{\max}/d_{\min} = 3.2$, 2.1 and 1.3 were chosen. For all three cases, the maximum aggregate size was $d_{\max} = 32$ mm. The meshes are displayed in Figure 12.

The average stress-strain curves for monotonic and cyclic compressive loading for the different aggregate size ratios is shown in Figures 13 and 14. The difference between the curves is small and falls in the range of scatters obtained by the initial study of the influence of the discretisation. Thus, the size ratio does not influence the monotonic and cyclic response strongly. The remaining three parameters are related to the material response and are independent of the discretisation used. Therefore, the results for these parameters are obtained with the same discretisation.

The next two parameters studied are related to the ratio of permanent and total inelastic displacements in the ITZ and mortar phase. This ratio is equal to the model parameter μ. The present meso-scale approach for cyclic loading is based on the hypothesis that the occurrence of localised permanent displacements is the main cause for the presence of the hysteresis loops. Consequently, a reduction of the permanent displacements (decrease of μ) should result in smaller hysteresis loops. The ratios $\mu = 1$, 0.95 and 0.9 were used. The monotonic and cyclic stress-strain curves for the three ratios of the ITZ phase are shown in Figure 15 and Figure 16, respectively. The size of the hysteresis loops decreases with increasing ratio of permanent and total inelastic displacements. This corresponds to the hypothesis that the hysteresis loops are caused by localised permanent displacement.

Furthermore, the influence of the permanent displacements in the mortar phase is studied. Again, the same values of $\mu = 1$, 0.95, 0.9 were used. The average stress-strain relations for monotonic and cyclic loading are presented in Figures 17 and 18. The ratio of the mortar phase has almost no influence on the pre-peak regime, since almost all nonlinearities result from the nonlinearities at the ITZs. However,

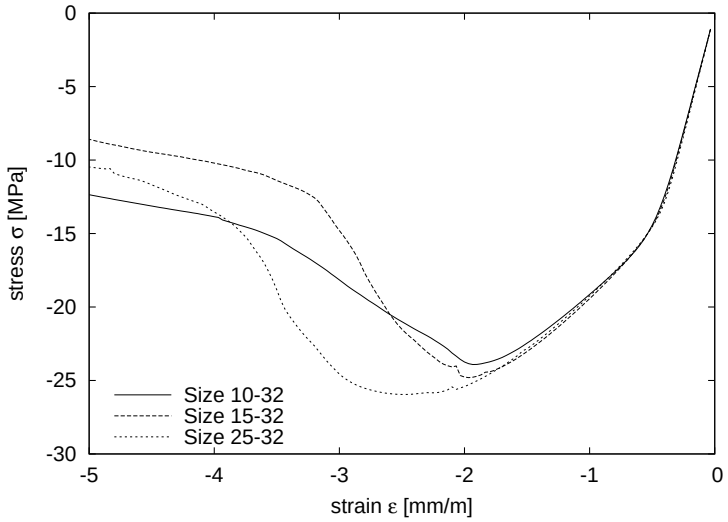

Figure 13: Stress-strain responses for monotonic loading for three aggregate-size ranges of $d_{\max}/d_{\min} = 3.2$, $d_{\max}/d_{\min} = 2.1$ and $d_{\max}/d_{\min} = 1.3$.

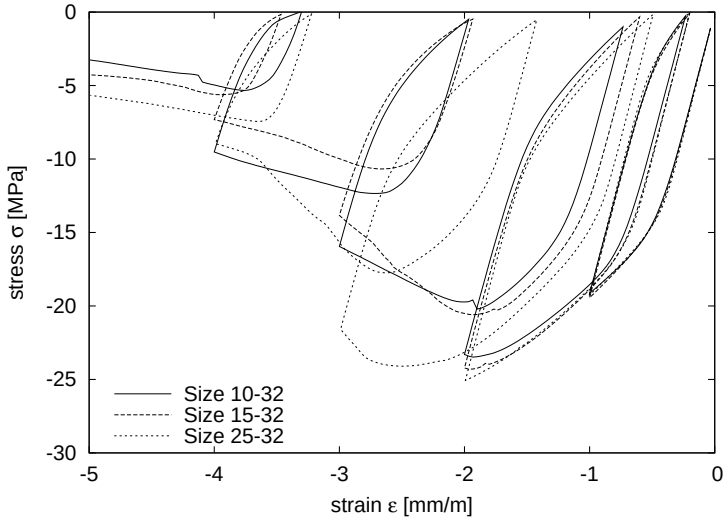

Figure 14: Stress-strain responses for cyclic loading for three aggregate-size ranges of $d_{\max}/d_{\min} = 3.2$, $d_{\max}/d_{\min} = 2.1$ and $d_{\max}/d_{\min} = 1.3$.

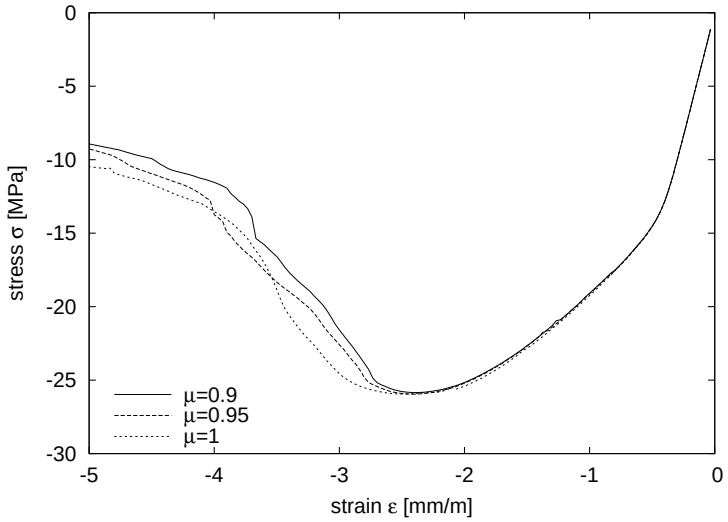

Figure 15: Stress-strain responses for monotonic loading for $\mu = 1$, 0.95 and 0.9 of the ITZ phase.

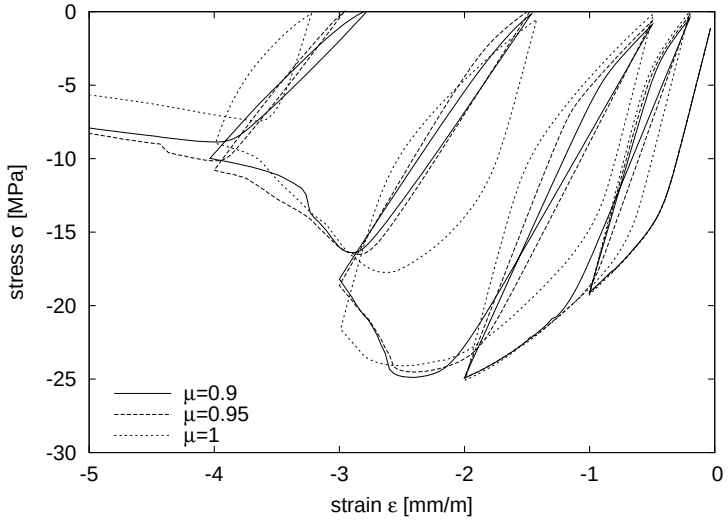

Figure 16: Stress-strain responses for cyclic loading for $\mu = 1$, 0.95 and 0.9 of the ITZ phase.

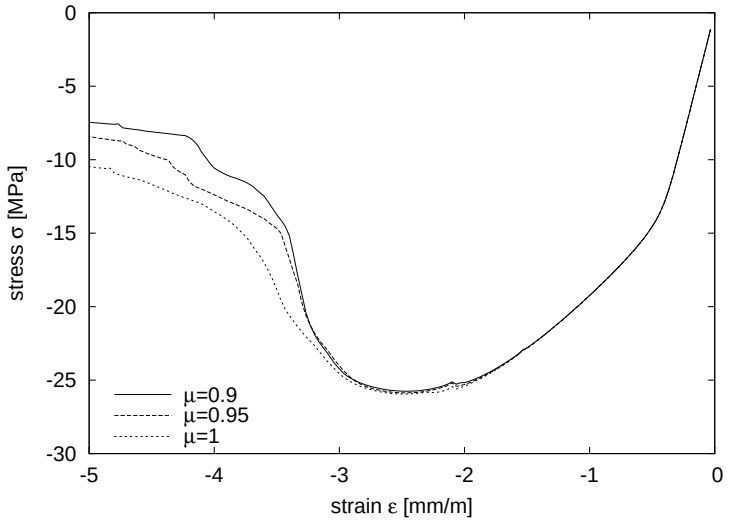

Figure 17: Stress-strain responses for monotonic loading for $\mu = 1$, 0.95 and 0.9 of the mortar phase.

in the post-peak regime nonlinear displacements occur in the mortar phase.

Finally, the influence of the ratio of the strength of ITZ and mortar was investigated. Three strength ratios of $f_{\mathrm{i}}/f_{\mathrm{m}} = 0.1$, $f_{\mathrm{i}}/f_{\mathrm{m}} = 0.2$ and $f_{\mathrm{i}}/f_{\mathrm{m}} = 0.3$ were considered. The average stress-strain relations for monotonic and cyclic loading are shown in Figures 19 and 20.

The strength ratio of ITZ and mortar has a strong influence on the monotonic and cyclic response. The compressive strength increases with an increased ITZ/mortar strength ratio, since the strength of the weak zones (ITZs) is increased. For the cyclic response, the size of the hysteresis loops decreases with increasing interface strength, since less permanent displacements take place at the interfaces between mortar and aggregates.

4 Conclusions

In the present work a meso-scale modelling approach developed in [9] was used for a parametric study of the modelling of concrete subjected to cyclic compression. Concrete was idealised by a three-phase composite consisting of mortar, aggregates and interfacial transition zones. Five parameters were investigated: aggregate volume fraction, aggregate size, ratio of the permanent and total inelastic displacements in the ITZ and mortar phase ,and the ratio of the strength of the interfacial transition zone and the mortar phase. The influences of the different parameters are summarised as following:

- A decrease of the volume fraction of aggregate increases the ultimate strength of concrete, since fewer aggregates correspond to a reduction of ITZs, which weaken the material. A decrease of volume fraction reduces also the size of the hysteresis loops, since the number of ITZs, at which permanent displacements take place, are reduced. Localised permanent displacements are the main reason for the occurrence of hysteresis loops in the present meso-scale modelling approach.
- The size range of aggregates does not strongly influence the response of concrete subjected to monotonic and cyclic loading.

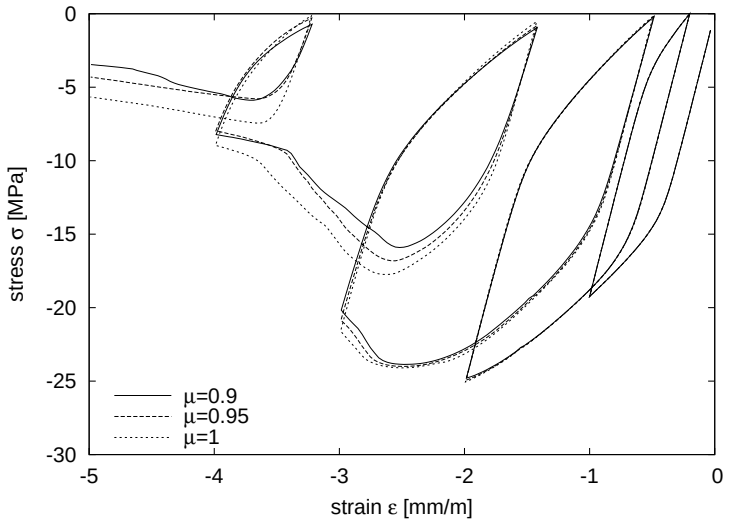

Figure 18: Stress-strain responses for cyclic loading for $\mu = 1$, 0.95 and 0.9 of the mortar phase.

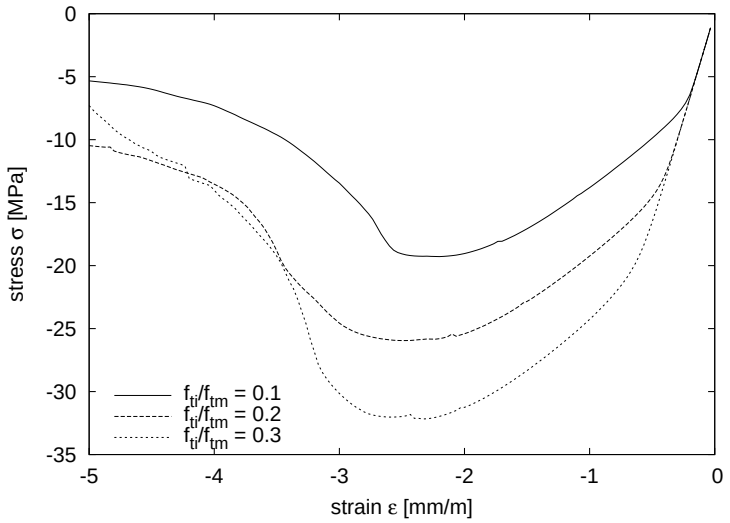

Figure 19: Stress-strain responses for monotonic loading for interface-mortar strength ratios of $f_{\mathrm{ti}}/f_{\mathrm{tm}} = 0.1$, 0.2 and 0.3.

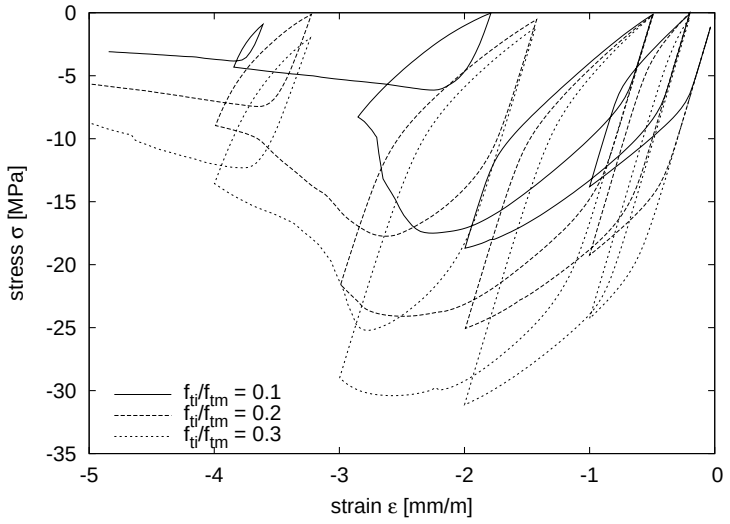

Figure 20: Stress-strain responses for cyclic loading for interface-mortar strength ratios of $f_{\mathrm{ti}}/f_{\mathrm{tm}} = 0.1$, 0.2 and 0.3.

- A decrease of the amount of permanent displacements in the ITZ phase results in a reduction of the size of the hysteresis loops.
- A decrease of the amount of permanent displacements in the mortar phase results in a decrease of the size of the loops in the post-peak regime, in which localised permanent displacements occur in the mortar phase.
- Finally, the ratio of the strength of the interfacial transition zone and the mortar has a strong influence on both the monotonic and cyclic response. An increase of the strength of ITZ leads to an increase of the compressive strength, since the amount of permanent displacements in the ITZs is reduced. Furthermore, the size of the hysteresis loops is decreased as well.

Acknowledgements

The simulations were performed with the object-oriented finite element package OOFEM [22, 23] extended by the present authors. The mesh has been prepared with the mesh generator Triangle [24].

References

[1] B. P. Sinha, K. H. Gerstle, and L. G. Tulin. Stress-strain relations for concrete under cyclic loading. *Journal of the American Concrete Institute*, 61:195–211, 1964.

[2] I. D. Karsan and J. O. Jirsa. Behavior of concrete under compressive loadings. *Journal of the Structural Division, ASCE*, 95:2543–2563, 1969.

[3] J. G. M. van Mier. *Strain-softening of concrete under multiaxial loading conditions*. PhD thesis, Technical University of Eindhoven, Eindhoven, The Netherlands, 1984.

[4] HAW Cornelissen, DA Hordijk, and HW Reinhardt. Experimental determination of crack softening characteristics of normalweight and lightweight concrete. *HERON*, 31(2):45–56, 1986.

[5] B. L. Yang, Y. F. Dafalias, and L. P. Herrmann. A bounding surface plasticity model for concrete. *Journal of Engineering Mechanics-ASCE*, 111:359–380, 1985.

[6] G. Z. Voyiadjis and T. M. Abu-Lebdeh. Plasticity model for concrete using the bounding surface concept. *International Journal of Plasticity*, 10:1–24, 1994.

[7] A. Pandolfi, P. Krysl, and M. Ortiz. Finite element simulation of ring expansion and fragmentation: The capturing of length and time scales through cohesive models of fracture. *International Journal of Fracture*, 95:279–297, 1999.

[8] F. Ragueneau, C. La Norderie, and J. Mazars. Damage model for concrete-like materials coupling cracking and friction, contribution towards structural damping: first uniaxial applications. *Mechanics of Cohesive-Frictional Materials*, 5:607–625, 2000.

[9] P. Grassl and R. Rempling. A damage-plasticity interface approach to the meso-scale modelling of concrete subjected to cyclic compressive loading. *Engineering Fracture Mechanics*, 75:4804–4818, 2008.

[10] J. E. Bolander and S. Saito. Fracture analysis using spring networks with random geometry. *Engineering Fracture Mechanics*, 61:569–591, 1998.

[11] J. E. Bolander and N. Sukumar. Irregular lattice model for quasistatic crack propagation. *Physical Review B*, 71, 2005.

[12] B. Budiansky and RJ O'Connell. Elastic moduli of a cracked solid. *International Journal of Solids and Structures*, 12(2):81–97, 1976.

[13] F. H. Heukamp, E. Lemarchand, and F. J. Ulm. The effect of interfacial properties on the cohesion of highly filled composite materials. *International Journal of Solids and Structures*, 42(1):287–305, 2005.

[14] L. Dormieux, D. Kondo, and F.J. Ulm. *Microporomechanics*. Wiley, 2006.

[15] E. P. Prado and J. G. M. van Mier. Effect of particle structure on mode i fracture process in concrete. *Engineering Fracture Mechanics*, 70:927–941, 2007.

[16] G. Lilliu and J. G. M. van Mier. 3d lattice type fracture model for concrete. *Engineering Fracture Mechanics*, 70:927–941, 2003.

[17] T. Kawai. New element models in discrete structural analysis. *Journal of Society of Naval Architecture in Japan*, 141:187–193, 1977.

[18] O. Morikawa, Y. Sawamota, and N. Kobayashi. Local fracture analysis of a reinforced concrete slab by the discrete element method. In MIT Press, editor, *Proceedings of the 2nd International Conf. on Discrete element methods*, pages 275–286, 1993. held in Cambridge, MA, USA.

[19] F. Aurenhammer. Voronoi diagrams - a survey of a fundamental geometric data structure. *ACM Computing Surveys*, 23:345–405, 1991.

[20] A. Zubelewicz and Z. P. Bažant. Interface modeling of fracture in aggregate composites. *Journal of Engineering Mechanics, ASCE*, 113:1619–1630, 1987.

[21] A. Carpinteri, P. Cornetti, and S. Puzzi. A stereological analysis of aggregate grading and size effect on concrete tensile strength. *International Journal of Fracture*, 128:233–242, 2004.

[22] B. Patzák. Object oriented finite element modeling. *Acta Polytechnica*, 39:99–113, 1999.

[23] B. Patzák and Z. Bittnar. Design of object oriented finite element code. *Advances in Engineering Software*, 32:759–767, 2001.

[24] Jonathan Richard Shewchuk. Triangle: Engineering a 2D Quality Mesh Generator and Delaunay Triangulator. In Ming C. Lin and Dinesh Manocha, editors, *Applied Computational Geometry: Towards Geometric Engineering*, volume 1148 of *Lecture Notes in Computer Science*, pages 203–222. Springer-Verlag, May 1996. From the First ACM Workshop on Applied Computational Geometry.

Rempling, R.; Svahn, P-O.; Lundgren, K.; Gylltoft, K. (2008).
Constitutive modelling of concrete subjected to cyclic loading,
including stress reversal.
Submitted to *Int. Journal of Fatigue*.

This page intentionally contains only this sentence.

Constitutive modelling of concrete subjected to cyclic loading, including stress reversal

Rasmus Rempling[1*], Per-Ola Svahn[2], Karin Lundgren[1] and Kent Gylltoft[1]
[1] Chalmers University of Technology, Göteborg, Sweden
[2] Skanska

Department of Civil and Environmental Engineering
Structural Engineering, Concrete Structures
Chalmers University of Technology, Gothenburg, Sweden

Submitted to Int. Journal of Fatigue on the 9th of February, 2009

* Corresponding author. Email: rasmus.rempling@chalmers.se

Abstract

Lately, it has become important to analyse existing concrete structures subjected to cyclic loading. A structures designed lifetime is often based on cyclic loads. Therefore, it is of importance to develop analysing methods that are accurate and reliable. The purpose of this report is to increase the understanding of the response of concrete subjected to cyclic loading. The model is a dual-model based on two sub-models: a damage sub-model and a plasticity sub-model. Their individual responses are rationed by a material parameter. The resulting constitutive response describes mechanisms observed in experimental results: hysteresis loops, non-linear unloading, low-stiffness unloading and energy dissipation due to hysteresis loops.

Key words: cyclic loading, fatigue, concrete, damage, plasticity, energy dissipation.

1 Introduction

Cyclic loading of concrete is one of many deterioration mechanisms that cause large economical costs for the society. With an increased understanding these costs can be cut. To reach better knowledge it is of importance to study the complex phenomenon of underlying mechanisms that generate the response of concrete subjected to cyclic loading, i.e. low cycle fatigue and normal state of confinement. In addition, the complexity increases if the cycles exhibit stress reversal, meaning that the stress is reversed during a cycle. In applications including reinforcement, the concrete is often cracked already in working conditions. Therefore, it is of interest to study the behaviour of cracked concrete. The response of concrete subjected to cyclic loading is highly non-linear after cracking as well as during crack closure of cyclic unloading. In addition, the increased damage of a softened concrete decreases the cyclic unloading- and cyclic loading stiffness. However, the characteristic hysteresis loops related to cyclic loading remain and exists in all stages for tension and compression.

Research that identifies these characteristic hysteresis loops has been done (among others, (Gopalaratnam and Shah, 1985; Plizzari et al., 1997; Gylltoft, 1983; Karsan and Jirsa, 1969; Sinha et al., 1964; Holmen, 1979; Reinhardt et al., 1986)) and models based on the concept of bounding surface, introduced by (Dafalias, 1986), have been used to model the phenomenon on macro-level: (Voyiadjis and Abulebdeh, 1993, 1994; Yang et al., 1985; Winnicki and Cichon, 1998; Pandolfi and Talercio, 1998; Abu-Lebdeh and Voyiadjis, 1993). Some models use plasticity, damage mechanics, and the combination of both to describe the non-linear response of concrete, e.g. models (Papa and Taliercio, 1996; Ragueneau et al., 2000; Desmorat et al., 2007). The knowledge about concrete subjected to fluctuating load is not extensive, though some attempts have been made (Reinhardt et al., 1986; Gylltoft, 1983; Tepfers, 1978; Clemmer, 1922; Crepps, 1923; Murdock and Kesler, 1958; Murdock, 1965; Reinhardt, 1984). (Grassl and Rempling, 2008) and (Rempling and Grassl, 2008) gave an interpretation of the mechanisms involved in cyclic loading of concrete by means of a meso-scale study. This investigation adds to these findings by reaching for larger structures on macro-level. The purpose of this study is to develop a model that is based on the physical understandings of concrete subjected to cyclic loading in the post-peak region. Moreover, mechanisms of cyclic loading are identified and investigated to present their contribution to the characteristic response.

2 Physical background of proposed model

Next, the response of cyclic loading is discussed to motivate the development and choices made during the development of the proposed model.

From experiments of concrete subjected to cyclic loading it is observed that the response is highly non-linear in compression as well as in tension for loading and unloading. The non-linear response stems from plastic sliding deformation in the

weak zones around the aggregates, see (Grassl and Rempling, 2008) and (Rempling and Grassl, 2008). In the continuation of the loading, micro-cracks form in the cement paste. These micro-crack bands bridge the aggregate-weak zones causing larger continuous damage zones. The damage zones cause the plastic deformation to increase. Finally, macro-cracks develop from the damage zones that generate irregular crack surfaces. These irregular surfaces are an important factor for the non-linear response of loaded concrete when observed at the unloading state. At unloading, the response is initially elastic, but as the irregular surfaces of the macro-crack meet, the fit of the surfaces is not perfect and sliding of the surfaces is forced to recover the plastic deformations of the loaded concrete.

Also, from deformation controlled uniaxial test of concrete in tension (Reinhardt et al., 1986; Gopalaratnam and Shah, 1985; Gylltoft, 1983; Tepfers, 1978; Reinhardt, 1984; Hordijk, 1991), a highly non-linear response is observed that exhibit increased level of damage after peak-load with increasing deformation. The same process as for cyclic loading is identified: plastic deformation increases in the localised zone with increased deformation. These two characteristic parts of the response call for a model that is based on damage mechanics and the theory of plasticity. Damage and plasticity have earlier been coupled, e.g. (Simo and Ju, 1987; Lee and Fenves, 1998; Grassl and Rempling, 2006; Jason et al., 2004), to describe concrete. In this study a dual-model is proposed which is a parallel combination of damage mechanics and the theory of plasticity (Figure 1). Furthermore, a material parameter is introduced that controls their relative contribution to the stiffness of the modell. The purpose of the

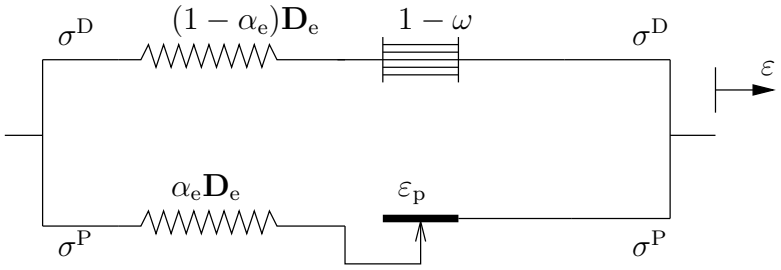

Figure 1: Rheological model of the dual-model.

parallel combination is that the plastic part should reflect the plastic deformation between aggregate and mortar; while, the damage part should reflect the overall softening response. This parallel combination calls for a softening of both parts as no residual stress can be transferred over a localised crack. Therefore, the plastic part softens with a softening modulus after peak-load while the damage part softens by an isotropic damage parameter.

The sliding of crack surfaces of concrete subjected to cyclic loading motivates the choice of a plastic part that consists of two yield surfaces: one outer-yield surface and one inner-yield surface. The outer-yield surface bounds the admissible stress state and is a yield surface of standard fashion. When violated, plastic flow is present, which increases the plastic deformations in the localised zones. On the contrary, at unloading, the stress is bound close to zero to represent the closure of the irregular crack surfaces. A hypothesis is presented that suggests that this sliding of crack surfaces is related to an energy that is released due to the change of shape, but not the change in volume.

This paper also investigates the concrete subjected to stress reversal and a variable that determines the state of stress is proposed. When a loaded state in tension unloads the initial unloading response is elastic. The response is elastic until a stress state close to zero is reached. This response is understood as the closure of micro-cracks. When the crack surfaces meet, sliding of the irregular crack surfaces is initiated. This sliding continues until the crack surfaces are completely closed. Then, the stiffness is recovered and the stress state is considered as compression.

3 Thermodynamic configuration

According to Clasius-Duheim Inequality, for an isotermic system ($\nabla T = 0$, where T is the temperature) with the mass density ρ_ψ and the free energy ψ, the dissipation rate of energy is

$$\dot{D} = \boldsymbol{\sigma} : \dot{\boldsymbol{\varepsilon}} - \rho_\psi \dot{\psi} \geq 0 \tag{1}$$

in which $\boldsymbol{\sigma} : \dot{\boldsymbol{\varepsilon}}$ is the external work due to the stress $\boldsymbol{\sigma}$ and the strain $\boldsymbol{\varepsilon}$.

The free energy depends on the reversible elastic strains $\boldsymbol{\varepsilon}_{\mathrm{e}}^{\mathrm{D}}$ and $\boldsymbol{\varepsilon}_{\mathrm{e}}^{\mathrm{P}}$. In addition, the free energy depends on the irreversible damage ω and the plastic hardening parameter κ_{p}

$$\psi(\boldsymbol{\varepsilon}_{\mathrm{e}}^{\mathrm{D}}, \boldsymbol{\varepsilon}_{\mathrm{e}}^{\mathrm{P}}, \omega, \kappa_{\mathrm{p}}). \tag{2}$$

Hence, the rate of the free energy is obtained as

$$\dot{\psi} = \frac{\partial \psi}{\partial \boldsymbol{\varepsilon}_{\mathrm{e}}^{\mathrm{D}}} : \dot{\boldsymbol{\varepsilon}}_{\mathrm{e}}^{\mathrm{D}} + \frac{\partial \psi}{\partial \boldsymbol{\varepsilon}_{\mathrm{e}}^{\mathrm{P}}} : \dot{\boldsymbol{\varepsilon}}_{\mathrm{e}}^{\mathrm{P}} + \frac{\partial \psi}{\partial \omega}\dot{\omega} + \frac{\partial \psi}{\partial \kappa_{\mathrm{p}}}\dot{\kappa}_{\mathrm{p}}. \tag{3}$$

In the proposed model the reversible strain for the damage part of the dual-model is identical to the total strain

$$\boldsymbol{\varepsilon}_{\mathrm{e}}^{\mathrm{D}} = \boldsymbol{\varepsilon}. \tag{4}$$

However, for the plastic part of the dual-model the reversible strain is obtained in standard fashion according to

$$\boldsymbol{\varepsilon}_{\mathrm{e}}^{\mathrm{P}} = \boldsymbol{\varepsilon} - \boldsymbol{\varepsilon}_{\mathrm{p}}. \tag{5}$$

By using Equations 1, 3, 4 and 5, the dissipated energy rate can be derived as

$$\left(\boldsymbol{\sigma} - \rho_\psi \frac{\partial \psi}{\partial \boldsymbol{\varepsilon}_{\mathrm{e}}^{\mathrm{D}}} - \rho_\psi \frac{\partial \psi}{\partial \boldsymbol{\varepsilon}_{\mathrm{e}}^{\mathrm{P}}}\right) : \dot{\boldsymbol{\varepsilon}} + \rho_\psi \frac{\partial \psi}{\partial \boldsymbol{\varepsilon}_{\mathrm{e}}^{\mathrm{P}}} : \dot{\boldsymbol{\varepsilon}}_{\mathrm{p}}^{\mathrm{P}} - \rho_\psi \frac{\partial \psi}{\partial \omega}\dot{\omega} - \rho_\psi \frac{\partial \psi}{\partial \kappa_{\mathrm{p}}}\dot{\kappa}_{\mathrm{p}} \geq 0. \tag{6}$$

This relation should always be valid even if the inelastic strain or damage have not evolved; thereby, the nominal stress $\boldsymbol{\sigma}$ is defined as (Figure 1)

$$\boldsymbol{\sigma} = \boldsymbol{\sigma}^{\mathrm{D}} + \boldsymbol{\sigma}^{\mathrm{P}} = \rho_\psi \frac{\partial \psi}{\partial \boldsymbol{\varepsilon}_{\mathrm{e}}^{\mathrm{D}}} + \rho_\psi \frac{\partial \psi}{\partial \boldsymbol{\varepsilon}_{\mathrm{e}}^{\mathrm{P}}}. \tag{7}$$

Using Equation 7 in Equation 6 the Clasius-Duheim-Inequality can be rewritten to

$$D_\omega \dot{\omega} + \left(\boldsymbol{\sigma}^{\mathrm{P}} : \dot{\boldsymbol{\varepsilon}}_{\mathrm{p}} + D_\kappa \dot{\kappa}_{\mathrm{p}}\right) \geq 0 \tag{8}$$

where the energy conjugates D_ω and D_κ are introduced

$$D_\omega = -\rho_\psi \frac{\partial \psi}{\partial \omega} \tag{9}$$

and

$$D_\kappa = -\rho_\psi \frac{\partial \psi}{\partial \kappa_{\mathrm{p}}}. \tag{10}$$

In the proposed model the free energy can be split in a damage- and a plastic part as

$$\psi(\boldsymbol{\varepsilon}_{\mathrm{e}}^{\mathrm{D}}, \boldsymbol{\varepsilon}_{\mathrm{e}}^{\mathrm{P}}, \omega, \kappa_{\mathrm{p}}) = \psi^{\mathrm{D}}(\boldsymbol{\varepsilon}_{\mathrm{e}}^{\mathrm{D}}, \omega) + \psi^{\mathrm{P}}(\boldsymbol{\varepsilon}_{\mathrm{e}}^{\mathrm{P}}, \kappa_{\mathrm{p}}). \tag{11}$$

The proposed damage part has a scalar damage

$$\rho_\psi \psi^{\mathrm{D}}(\boldsymbol{\varepsilon}_{\mathrm{e}}^{\mathrm{D}}, \omega) = \frac{1}{2}(1-\alpha_{\mathrm{e}})(1-\omega)\boldsymbol{\varepsilon}_{\mathrm{e}}^{\mathrm{D}} : \boldsymbol{D}_{\mathrm{e}} : \boldsymbol{\varepsilon}_{\mathrm{e}}^{\mathrm{D}} \tag{12}$$

where $\boldsymbol{D}_{\mathrm{e}}$ is the elastic stiffness tensor and α_{e} is a material parameter that defines the distribution of free energy between the damage- and the plastic part. The free energy of the plastic part can be defined by the elastic response together with linear hardening, assuming rate-independent inelastic stress-strain behaviour of the plastic part:

$$\rho_\psi \psi^{\mathrm{P}}\left(\boldsymbol{\varepsilon}_{\mathrm{e}}^{\mathrm{P}}, \kappa_{\mathrm{p}}\right) = \frac{1}{2}\alpha_{\mathrm{e}}\boldsymbol{\varepsilon}_{\mathrm{e}}^{\mathrm{P}} : \boldsymbol{D}_{\mathrm{e}} : \boldsymbol{\varepsilon}_{\mathrm{e}}^{\mathrm{P}} + \frac{1}{2}\kappa_{\mathrm{p}} H \kappa_{\mathrm{p}} \tag{13}$$

where H is the hardening modulus for yielding.

The stress in Equation 7 can now be determined as

$$\boldsymbol{\sigma}^{\mathrm{D}} = \rho_\psi \frac{\partial \psi}{\partial \boldsymbol{\varepsilon}_{\mathrm{e}}^{\mathrm{D}}} = \rho_\psi \frac{\partial \psi^{\mathrm{D}}}{\partial \boldsymbol{\varepsilon}_{\mathrm{e}}^{\mathrm{D}}} = (1-\alpha_{\mathrm{e}})(1-\omega)\boldsymbol{D}_{\mathrm{e}} : \boldsymbol{\varepsilon}_{\mathrm{e}}^{\mathrm{D}} = (1-\alpha_{\mathrm{e}})(1-\omega)\boldsymbol{D}_{\mathrm{e}} : \boldsymbol{\varepsilon} \tag{14}$$

and

$$\boldsymbol{\sigma}^{\mathrm{P}} = \rho_\psi \frac{\partial \psi}{\partial \boldsymbol{\varepsilon}_{\mathrm{e}}^{\mathrm{P}}} = \rho_\psi \frac{\partial \psi^{\mathrm{P}}}{\partial \boldsymbol{\varepsilon}_{\mathrm{e}}^{\mathrm{P}}} = \alpha_{\mathrm{e}} \boldsymbol{D}_{\mathrm{e}} : \boldsymbol{\varepsilon}_{\mathrm{e}}^{\mathrm{P}}. \tag{15}$$

Now, consider the dissipation of energy by expanding the terms of the rewritten dissipation equation (Equation 8), which gives the following:

- For the plastic term assuming a non-associated flow rule

$$\boldsymbol{\sigma}^{\mathrm{P}} : \dot{\boldsymbol{\varepsilon}}_{\mathrm{p}} + D_{\kappa}\dot{\kappa}_{\mathrm{p}} = \boldsymbol{\sigma}^{\mathrm{P}} : \dot{\lambda}\frac{\partial g}{\partial \boldsymbol{\sigma}^{\mathrm{P}}} + H\kappa_{\mathrm{p}}\dot{\lambda}\frac{\partial q_{\mathrm{h}}}{\partial \kappa_{\mathrm{p}}} \geq 0 \tag{16}$$

  where $\dot{\lambda}$ is the rate of the plastic multiplier and q_{h} is the hardening function;

- while, for the damage term

$$D_{\omega}\dot{\omega} = \frac{1}{2}\dot{\omega}(1-\alpha_{\mathrm{e}})\boldsymbol{\varepsilon} : \boldsymbol{D}_{\mathrm{e}} : \boldsymbol{\varepsilon} \geq 0. \tag{17}$$

To assure a thermodynamic admissibility Equations 16 and 17 can conservatively be evaluated separately, so that each one is assured to dissipate energy from the system.

3.1 Dissipation of energy in the damage part

First, consider loading of the inequality that regards the damage variable, Equation 17. For loading, the dissipation due to damage is assured as $\dot{\omega}$ only can increase by definition which gives positive values for all states of stress and strain. However, at unloading, when changing from tension to compression, $\dot{\omega}$ is negative. Although, the volumetric part of the stress is zero in this point the deviatoric stress may not. This drawback is a consequence of the decoupled variant of the plastic and damage parts.

3.2 Dissipation of energy in the plastic part

Normally, the yield surface is defined by stress invariants. Thereby, Equation 16 can be rewritten by Haigh-Westergaard coordinates ($\boldsymbol{\sigma}^{\mathrm{P}} = [\xi\ \rho]$) according to

$$\boldsymbol{\sigma}^{\mathrm{P}} : \dot{\lambda}\frac{\partial g}{\partial \boldsymbol{\sigma}^{\mathrm{P}}} + H\kappa_{\mathrm{p}}\dot{\lambda}\frac{\partial q_{\mathrm{h}}}{\partial \kappa_{\mathrm{p}}} = \dot{\lambda}\left(\xi\left[\frac{\partial g}{\partial \boldsymbol{\sigma}^{\mathrm{P}}}\right]_1 + \rho\left[\frac{\partial g}{\partial \boldsymbol{\sigma}^{\mathrm{P}}}\right]_2 + H\kappa_{\mathrm{p}}\frac{\partial q_{\mathrm{h}}}{\partial \kappa_{\mathrm{p}}}\right) \geq 0 \tag{18}$$

and the characteristics of the individual components can be identified. The characteristics depend on the fact that fluctuating load is considered, i.e. different characteristics for compression and tension. These characteristics can be summarised as:

- $\dot{\lambda}$ – is positive by definition, Equation 35.
- ξ – is positive for tension loading, but negative for compression loading.
- $\left[\frac{\partial g}{\partial \boldsymbol{\sigma}^{\mathrm{P}}}\right]_1$ – determines the amount of plastic strain in the volumetric direction (ξ).
- ρ – is positive by definition for tension as well as compression.

- $\left[\frac{\partial g}{\partial \boldsymbol{\sigma}^{\mathrm{P}}}\right]_2$ – determines the amount of plastic strain in the deviatoric direction (ρ).
- H is the hardening/softening modulus.
- κ_{p} is the plastic hardening parameter.
- q_{h} is the hardening function. The derivative of the hardening function by the plastic hardening parameter is assumed to be: for tension $\frac{\partial q_{\mathrm{h}}}{\partial \kappa_{\mathrm{p}}} = 1$ and compression $\frac{\partial q_{\mathrm{h}}}{\partial \kappa_{\mathrm{p}}} = 0$.

Assume a plastic potential that defines the direction of the plastic flow according to the Drucker-Prager definition:

$$g(\xi, \rho) = \alpha_\psi \xi + \rho \tag{19}$$

where α_ψ is the dilatancy coefficient which controls the volumetric part of the plastic strain.

Three cases are identified and evaluated below for the plastic part: **A,** the outer-yield surface in compression; **B,** the outer-yield surface in tension; and **C,** the inner-yield surface in compression and tension.

A Consider the outer-yield surface in compression to define $\left[\frac{\partial g}{\partial \boldsymbol{\sigma}^{\mathrm{P}}}\right]_1$. For compression, $\frac{\partial q_{\mathrm{h}}}{\partial \kappa_{\mathrm{p}}} = 0$. Hence, the first component of the plastic potential can be defined by the relation between the volumetric and deviatoric stresses according to

$$\left[\frac{\partial g}{\partial \boldsymbol{\sigma}^{\mathrm{P}}}\right]_1 = \frac{-\rho}{\xi} \tag{20}$$

B Consider the outer-yield surface in tension ($\xi \geq 0$). In accordance with, **A**, the first term of the plastic potential is defined as

$$\left[\frac{\partial g}{\partial \boldsymbol{\sigma}^{\mathrm{P}}}\right]_1 = \frac{-\rho - H\kappa_{\mathrm{p}}\frac{\partial q_{\mathrm{h}}}{\partial \kappa_{\mathrm{p}}}}{\xi} \tag{21}$$

and $\left[\frac{\partial g}{\partial \boldsymbol{\sigma}^{\mathrm{P}}}\right]_2 = 1$, according to Equation 19. Hence, H can be stated as

$$H \geq \frac{-\xi\left[\frac{\partial g}{\partial \boldsymbol{\sigma}^{\mathrm{P}}}\right]_1 + \rho}{\kappa_{\mathrm{p}}\frac{\partial q_{\mathrm{h}}}{\partial \kappa_{\mathrm{p}}}}. \tag{22}$$

C Consider the inner-yield surface in tension and compression with $H = 0$. Assuming a plastic potential with no volumetric evolution, i.e.

$$g^{\emptyset}(\rho) = \rho. \tag{23}$$

Then, $\left[\frac{\partial g^{\emptyset}}{\partial \boldsymbol{\sigma}^{\mathrm{P}}}\right]_1 = 0$ and $\left[\frac{\partial g^{\emptyset}}{\partial \boldsymbol{\sigma}^{\mathrm{P}}}\right]_2 = 1$, which yields a positive dissipation for all states of ρ.

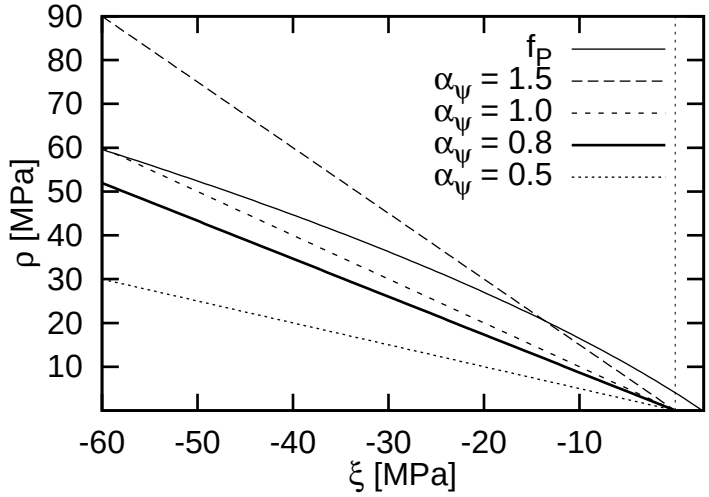

Figure 2: Different values of α_ψ for the plastic potential with regard to the outer-yield surface.

As given above there may exist states of stress where the model is not thermodynamical admissible. Those states are dependent on the choice of α_ψ. In Figure 2 different plastic potential functions are plotted, to identify for which compressive states a certain value of α_ψ is valid. The value of $\alpha_\psi = 0.86$ corresponds to biaxial compression.

$\dot{\lambda} \geq 0$ according to the loading/unloading conditions in Equation 35.

This satisfies the Clausius-Duheim inequality and assures that choices made within the given limits result in a thermodynamical admissible model.

4 Constitutive configuration

The nominal stress $\boldsymbol{\sigma}$ is composed by a damage- and a plastic part as presented in Equation 7. Consequently, the nominal-stress – strain relationship can be presented as

$$\boldsymbol{\sigma} = \boldsymbol{\sigma}^{\mathrm{D}} + \boldsymbol{\sigma}^{\mathrm{P}} = (1-\alpha_{\mathrm{e}})(1-\omega)\boldsymbol{D}_{\mathrm{e}} : \boldsymbol{\varepsilon}_{\mathrm{e}}^{\mathrm{D}} + \alpha_{\mathrm{e}}\boldsymbol{D}_{\mathrm{e}} : \boldsymbol{\varepsilon}_{\mathrm{e}}^{\mathrm{P}}. \tag{24}$$

Next follows the constitutive configuration of these parts.

4.1 Damage part

The damage variable ω is a scalar, thus the damage model is an isotropic damage model. Though, the damage variable is only valid for tension, which results in a stiffness recover at deformation reversal, understood as at unloading of a localised crack the stiffness is recovered at complete closure of the crack. The evolution of

damage is defined by the loading function

$$f_{\mathrm{D}} = \tilde{\varepsilon} - \kappa_{\mathrm{D}} \tag{25}$$

where the equivalent strain is determined according to

$$\tilde{\varepsilon} = \sqrt{\boldsymbol{\varepsilon}_{\mathrm{e}}^{\mathrm{D}} : \boldsymbol{\varepsilon}_{\mathrm{e}}^{\mathrm{D}}} = \sqrt{\boldsymbol{\varepsilon} : \boldsymbol{\varepsilon}}; \tag{26}$$

κ_{D} is the damage-history variable which is computed as the maximum equivalent strain that the model has experienced according to

$$\kappa_{\mathrm{D}} = max(\tilde{\varepsilon}). \tag{27}$$

At a completely localised and opened crack no stress transfer is possible. This is considered by a material parameter ε_{f} that defines, for uniaxial tension, a linear softening law which is dependent on the ultimate strength f_{t} and the strain

$$\boldsymbol{\sigma}^{\mathrm{D}} = (1 - \frac{\kappa_{\mathrm{D}}}{\varepsilon_{\mathrm{f}}}) f_{\mathrm{t}}. \tag{28}$$

The linear softening law and the damage stress (Equation 14) is used for deriving the damage function

$$\omega(\kappa_{\mathrm{D}}) = \begin{cases} 0 & \varepsilon_0 \geq \kappa_{\mathrm{D}} \\ \frac{1-\frac{\varepsilon_0}{\kappa_{\mathrm{D}}}}{1-\frac{\varepsilon_0}{\varepsilon_{\mathrm{f}}}} & \varepsilon_0 < \kappa_{\mathrm{D}} \leq \varepsilon_{\mathrm{f}} \end{cases} \tag{29}$$

where ε_0 is the strain at the onset of damage. Equation 29 is used for computing the damage parameter in tension ($\sigma_{\mathrm{v}} > 0$), while for compression ($\sigma_{\mathrm{v}} \leq 0$) the damage parameter is set to zero.

To consider localisation the smeared crack approach is used, i.e. the crack width is smeared over the length of the element in the direction of the largest principal strain.

4.2 Plastic part

The plastic stress of the dual-model was derived in Equation 15. The plastic part of the dual-model consists of an outer- and an inner-yield surface. These control if yielding is present for loading or unloading, respectively. The yield surfaces are illustrated in Figure 3. The presence of an inner-yield surface is of fundamental art when describing cyclic loading, as it has been observed in experiments that plastic flow evolve during unloading (Reinhardt et al., 1986; Gylltoft, 1983, among others).

The choice of the shape of the outer-yield surface depends on the physical interpretation of concrete in compression and tension. It is observed in experiments (e.g. (Imran, 1994)) that the shape of the final strength varies along the hydrostatic axis as illustrated in Figure 3. For limitations to reasonably high confined stress states

this shape can be considered as open, as illustrated to the upper-left in Figure 3. The outer-yield surface has the shape of a circle in the deviatoric stress space, as shown to the lower-left in Figure 3. For high hydrostatic pressure the shape of a circle in the deviatoric stress space is considered as a correct interpretation (Jirasek and Bazant, 2001). However, at low hydrostatic pressure the shape of a triangle is more correct. Thus, experiments show that there is an evolution of the shape during increasing hydrostatic pressure from a triangular- to a circular shape in the deviatoric stress space. Though, for simplicity the shape of an circle is assumed in this work.

On the opposite, the choice of the shape of the inner-yield surface is only dependent on the fact that it should bound the stress and exhibit plastic flow during unloading; therefore, a shape of von Mises was chosen as it was considered to be suitable. This is shown to the right in Figure 3. As unloading starts from a loaded state, there is a need for activation of the inner-yield surface for stress states inside the inner-yield surface.

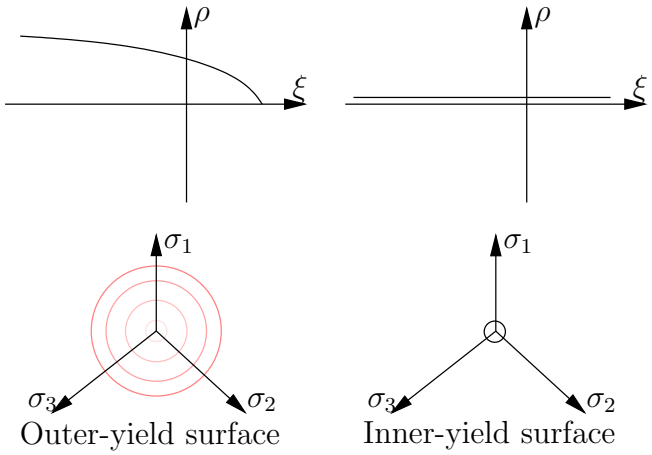

Figure 3: Illustration of the outer- and inner-yield surfaces. Above, the volumetric stress space (Haigh-Westergaard coordinates) is given and below the deviatoric stress space.

Next follows a deeper presentation of the outer- and inner-yield surface.

4.2.1 Outer-yield surface

The stress state is bound by the outer-yield surface chosen according to the Ottosen yield surface proposed by (Ottosen, 1977). The Ottosen yield surface has the shape as illustrated to the left in Figure 3 and is therefore limited to reasonable high confined stress states in compression. The Ottosen yield surface is stated as

$$f_{\mathrm{P}} = \frac{C_1}{f_{\mathrm{c}}}(\xi - H_{\mathrm{P}}^*) + \frac{C_2}{f_{\mathrm{c}}}\rho + \frac{C_3}{f_{\mathrm{c}}^2}\rho^2 - 1 \tag{30}$$

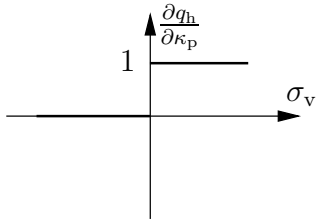

Figure 4: Evolution of the plastic-strain-history variable.

where C_1, C_2 and C_3 are material parameters given at input and H_P^* is the softening function.

In Chapter 3 a non-associated flow rule is assumed. For the outer-yield surface a potential from the Drucker-Prager criterion was chosen according to

$$g(\xi, \rho) = \alpha_\psi \xi + \rho \tag{31}$$

The evolution of the plastic strain consequently becomes

$$\dot{\boldsymbol{\varepsilon}}_\mathrm{p} = \dot{\lambda} \frac{\partial g}{\partial \boldsymbol{\sigma}^\mathrm{P}}. \tag{32}$$

Softening of the plastic part of the model is needed to achieve a stress-free, fully opened crack. This is introduced in the plastic part by a linear softening function H_p^* which is valid for tension, while for compression it is equal to zero, i.e. perfect plasticity is applied for compressive states. To achieve a stress-free, fully opened crack the plastic stress must soften in accordance with the damage stress. The softening function is driven by the plastic-strain-history variable κ_p that evolves with its evolution function $\frac{\partial q_\mathrm{h}}{\partial \kappa_\mathrm{p}}$ (Figure 4) according to

$$\dot{\kappa}_\mathrm{p} = \begin{cases} \dot{\lambda} \frac{\partial q_\mathrm{h}}{\partial \kappa_\mathrm{p}} & \text{if } \sigma_\mathrm{v} \geq 0 \\ 0 & \text{if } \sigma_\mathrm{v} \leq 0 \end{cases} \tag{33}$$

The evolution of κ_p depends on the stress state that is defined by the volumetric stress σ_v. This is a fundamental issue of cyclic loading, why it is discussed last in this section (Chapter 4.3).

Finally, the softening function is defined as

$$H_\mathrm{p}^* = H \kappa_\mathrm{p} \tag{34}$$

where H is the softening modulus.

The Kuhn-Tucker loading/unloading conditions of the outer-yield surface are defined in standard fashion. The yield function must remain negative in the elastic regime at the same time as the rate of the plastic multiplier must be zero, or remain constant at reloading. However, in the plastic regime the rate of the plastic multiplier must be positive. The loading/unloading conditions for compression and tension are

$$f_\mathrm{P} \leq 0 \quad \dot{\lambda} \geq 0 \quad \dot{\lambda} f_\mathrm{P} = 0 \tag{35}$$

4.2.2 Inner-yield surface

As discussed in the introduction, a non-linear unloading response is observed for compression as well as for tension due to the sliding of crack zones/surfaces. This is treated by an inner-yield surface chosen according to von Mises, which bounds the deviatoric stress states close to zero.

$$f^{\emptyset} = \rho - f_{\mathrm{y}}^{\emptyset}; \tag{36}$$

$f_{\mathrm{y}}^{\emptyset}$ is the inner-yield stress.

As commented sliding of crack surfaces happens for a stress state close to zero during unloading. Therefore, the inner-yield surface can not be active during the whole unloading process, as the unloading starts from a loaded state. This calls for an activation rule of the inner-yield surface. The authors define unloading by the increment of the largest principal strain according to $\Delta\varepsilon_1 \leq 0$ and propose negative distortional energy ($W_{\mathrm{D}}^{\mathrm{P}} \leq 0$) as an activation rule of the inner-yield surface. The distortional energy corresponds to the deviatoric part of the energy according to

$$W_{\mathrm{D}}^{\mathrm{P}} = \frac{1}{2}\boldsymbol{s}^{\mathrm{P}} : \boldsymbol{e} \tag{37}$$

where $\boldsymbol{s}^{\mathrm{P}} = \boldsymbol{\sigma}^{\mathrm{P}} - \sigma_{\mathrm{v}}^{\mathrm{P}}\boldsymbol{\delta}$ is the deviatoric stress and
$\boldsymbol{e} = \boldsymbol{\varepsilon} - \varepsilon_{\mathrm{v}}\boldsymbol{\delta}$ is the deviatoric strain.

As commented the evolution of the plastic deformation during unloading of concrete is an important issue to consider. Before, it was derived for a non-associated flow rule that there exists a conservative limitation of the evolution of plastic strain. However, for the chosen inner-yield surface the derivation corresponds to an associated flow rule

$$\dot{\boldsymbol{\varepsilon}}_{\mathrm{p}} = \dot{\lambda}\frac{\partial f^{\emptyset}}{\partial \boldsymbol{\sigma}^{\mathrm{P}}} \tag{38}$$

that restrains the volumetric rate of the plastic strain to zero due to the nature of the inner-yield surface.

The loading/unloading conditions of the inner-yield surface are the same as for the outer-yield surface

$$f^{\emptyset} \leq 0 \quad \dot{\lambda} \geq 0 \quad \dot{\lambda} f^{\emptyset} = 0. \tag{39}$$

4.3 Stress reversal – determination of stress state

To consider stress reversal in a 3-dimensional stress state, there stems a need of a variable that determines the state of tension or compression. The volumetric stress $\sigma_{\mathrm{v}} = \boldsymbol{\sigma} : \boldsymbol{\delta}$ is proposed as variable for determine the stress state. The choice of σ_{v} limits the model to only consider volumetric-stress reversal as deviatoric-stress reversal is not defined by σ_{v}. Thus, cyclic-stress reversal is defined parallell to the

hydrostatic axis only. Voyiadjis and Abulebdeh ((Voyiadjis and Abulebdeh, 1994)) make a different approach. They define plastic unloading in the deviatoric plane by means of the distance from the current stress point to the tensile meridian. This distance is normalised with the current distance between the hydrostatic axis and the yield surface. That concept introduces complexities which are not easily penetrated and hide limitations of the formulation. The dual-model instead intend to always change sign of the stress close to zero, which makes the current stress state well defined as well as whether it is loading, unloading or reloading in tension or compression.

5 Implementation

The present model is implemented in the framework of finite elements and the loading process is divided into discrete time steps. At the end of each step the boundary value problem and the integration of the constitutive model are solved.

For the global problem (boundary value problem) the tangent-stiffness matrix

$$\boldsymbol{D}_{\mathrm{ep}} = (1-\alpha_{\mathrm{e}})(1-\omega)\boldsymbol{D}_{\mathrm{e}} + \boldsymbol{D}_{\mathrm{e}} - \frac{(1-\alpha_{\mathrm{e}})(1-\omega)+\alpha_{\mathrm{e}}}{\alpha_{\mathrm{e}}} \frac{\boldsymbol{D}_{\mathrm{e}} : \frac{\partial g}{\partial \boldsymbol{\sigma}} \otimes \frac{\partial f}{\partial \boldsymbol{\sigma}} : \boldsymbol{D}_{\mathrm{e}}}{\frac{\partial f}{\partial \boldsymbol{\sigma}} : \boldsymbol{D}_{\mathrm{e}} : \frac{\partial g}{\partial \boldsymbol{\sigma}}} \tag{40}$$

is used, where the gradient of the yield law is defined as:

- For the outer- and inner-yield surfaces, respectively

$$\frac{\partial f_{\mathrm{P}}}{\partial \boldsymbol{\sigma}} = \frac{C_1}{\sqrt{3}}\boldsymbol{\delta} + C_2 + 2C_3 J_2 \frac{\sqrt{2}}{2\sqrt{J_2}}\boldsymbol{s} \tag{41}$$

  and

$$\frac{\partial f^{\emptyset}}{\partial \boldsymbol{\sigma}} = J_2 \frac{\sqrt{2}}{2\sqrt{J_2}}\boldsymbol{s}. \tag{42}$$

- The gradient of the plastic potential of the outer- and the inner-yield surface, respectively

$$\frac{\partial g}{\partial \boldsymbol{\sigma}} = \frac{\alpha}{\sqrt{3}}\boldsymbol{\delta} + \frac{\sqrt{2}}{2\sqrt{J_2}}\boldsymbol{s}. \tag{43}$$

  and

$$\frac{\partial g^{\emptyset}}{\partial \boldsymbol{\sigma}} = \frac{\partial f^{\emptyset}}{\partial \boldsymbol{\sigma}}. \tag{44}$$

In the above equations $J_2 = 1/2\boldsymbol{s} : \boldsymbol{s}$ is the second stress invariant.

For the case of pure damage $\alpha_{\mathrm{e}} = 0$ a problem of division by zero arises in the definition of the tangent-stiffness matrix, Equation 40. This problem is avoided by using the secant-stiffness matrix

$$\boldsymbol{D}_{\mathrm{s}} = (1-\omega)\boldsymbol{D}_{\mathrm{e}} \tag{45}$$

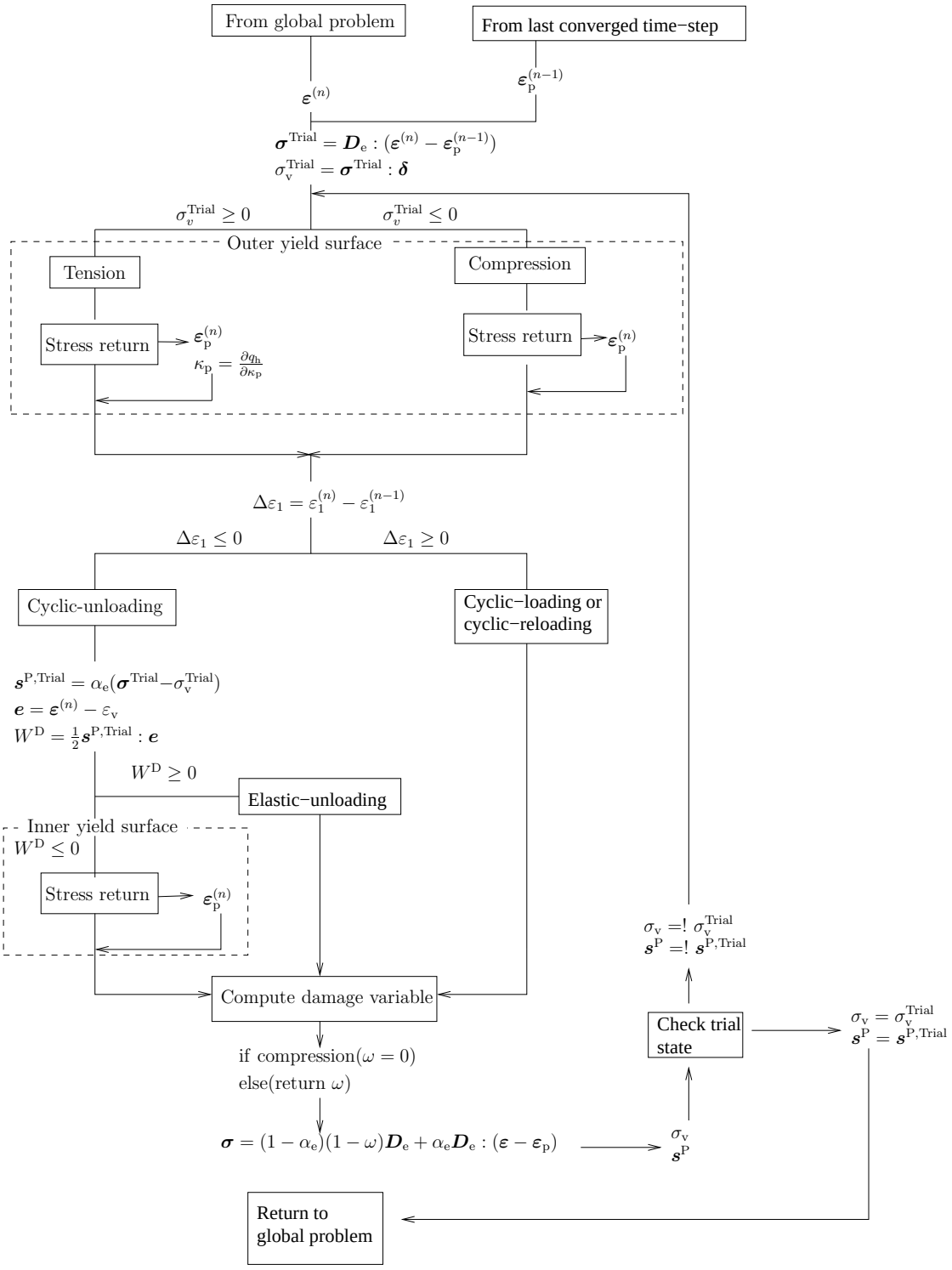

Figure 5: Flow chart of the major steps of the implemented dual-model.

for the case of pure damage.

The solving is divided into sequential steps of (Figure 5): Firstly, solving the plastic part that generates the plastic strain $\boldsymbol{\varepsilon}_{\mathrm{p}}$ and the plastic-stress $\boldsymbol{\sigma}^{\mathrm{P}}$ and secondly, solving the damage part that generates the isotropic damage variable ω and the damage-stress $\boldsymbol{\sigma}^{\mathrm{D}}$. The stresses are then added to yield the nominal stress at the end of the step n.

5.1 Damage part

The solving of the local problem of the damage part is efficient as the equivalent strain $\tilde{\varepsilon}$ is determined by the total strain $\boldsymbol{\varepsilon}$ according to Equation 26.

5.2 Plastic part

The stress return algorithm computes the stress coordinates on the yield surface by the direction defined by the plastic flow potential, starting from the trial stress, i.e. the stress on the yield surface is the projection of the trial stress on the yield surface. This is a procedure which consists of solving a number of non-linear equations. The method of closest point projection is used for solving these non-linear equations. The shape of the plastic potential in the deviatoric plane determines the lode angle of the trial stress and the stress on the yield surface. If the lode angle is the same for both cases the number of non-linear equations are significantly reduced, which is the case for the proposed dual-model. Then, the number of non-linear equations to solve is reduced to four; each of the non-linear equations has a residual that should be zero at equilibrium. Thus, when the norm of the residuals is close to zero convergence is reached. The following residuals are identified for the stress return algorithm used for the dual-model:

$$R_1^{(n+1)} = -\varepsilon_{\mathrm{p},\xi}^{(n+1)} + \varepsilon_{\mathrm{p},\xi}^{(n)} + \Delta\lambda \left(\frac{\partial g}{\partial \xi}\right)^{(n+1)} \tag{46}$$

$$R_2^{(n+1)} = -||\varepsilon_{\mathrm{p},\rho}^{(n+1)}|| + ||\varepsilon_{\mathrm{p},\rho}^{(n)}|| + \Delta\lambda \left(\frac{\partial g}{\partial \rho}\right)^{(n+1)} \tag{47}$$

$$R_3^{(n+1)} = -\kappa_{\mathrm{p}}^{(n+1)} + \kappa_{\mathrm{p}}^{(n)} + \Delta\lambda \left(\frac{\partial q_{\mathrm{h}}}{\partial \kappa_{\mathrm{p}}}\right)^{(n+1)} \tag{48}$$

$$f^{(n+1)} = f(\xi^{(n+1)}, \rho^{(n+1)}, \Delta\lambda, \kappa_{\mathrm{p}}). \tag{49}$$

In the above first two equations the plastic strains correspond to the volumetric plastic strain ($\varepsilon_{\mathrm{p},\xi} = 1/3(\varepsilon_{\mathrm{p},1} + \varepsilon_{\mathrm{p},2} + \varepsilon_{\mathrm{p},3})$) and the length of the deviatoric plastic strain, respectively.

6 Constitutive response

The constitutive response was used to evaluate the involved parameters that are important for the cyclic response. For the analyzes the presented material parameters in Table 1 was used. First, a general response of three different cyclic loads are presented. Second, the influence of α_e is discussed and finally the distortional energy W^D for different cases of loading is presented and discussed.

Table 1: Material parameters chosen for the analyses

E	ν	ε_0	ε_f	H	α_ψ
30 MN/m^2	0.18	0.0095 ‰	1.0 ‰	$0.1E$	0.1

C_1	C_2	C_3	f_c	$f_y^\emptyset$
5.25	3.55	0.5	16.5 MN/m^2	1 kN/m^2

6.1 General response

For the general response on constitutive level three different loadings are considered to be interesting because they capture the most likely loadings to occur:

1. Three cycles after peak-load in uniaxial tension, unloaded to a nominal stress 0.2 MPa (Figure 6)
2. Three cycles after peak-load in uniaxial tension, unloaded to a nominal stress -3.0 MPa (Figure 7)
3. Three cycles after peak-load in uniaxial tension, unloaded to a strain of -11.0 ‰, -10.75 ‰ and -10.50 ‰ (Figure 8)

For the analyses $\alpha_e = 0.3$ was chosen as this was evaluated during the analyses to be a reasonable value, see Section 6.2.

The stress-strain response of cyclic loading after peak-load in tension is presented in Figure 6. Initially the response is elastic, but after peak-load damage deteriorates the stiffness and the response softens. At 1.70 ‰ the first unloading is performed. The response is elastic, but the stiffness has been reduced by the damage. At approximately 1.1 ‰ unloading plastic flow is initiated. When a stress of 0.2 MPa is reached reloading is performed with the same stiffness as for unloading. At the completeness of a hysteresis loop softening once again is initiated and the stiffness deteriorate.

In Figure 7 and 8 the unloading is continued so that a stress reversal is achieved. The low stiffness at unloading is recovered when the model enters a stress state of

compression. In Figure 7 the response in compression is elastic, while in Figure 8 the unloading is continued to initiate plastic flow in compression. The perfect plastic response assumed in compression is shown in Figure 8.

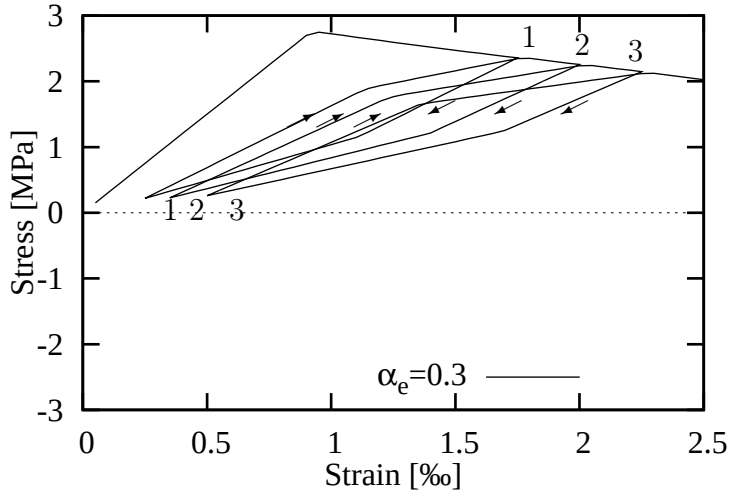

Figure 6: Response of an uniaxial deformation with $\alpha_e = 0.3$. Three cycles (1,2,3) are loaded to a strain of: 1.70 ‰, 2.0 ‰ and 2.25 ‰, respectively and unloaded to a stress of 0.2 MPa.

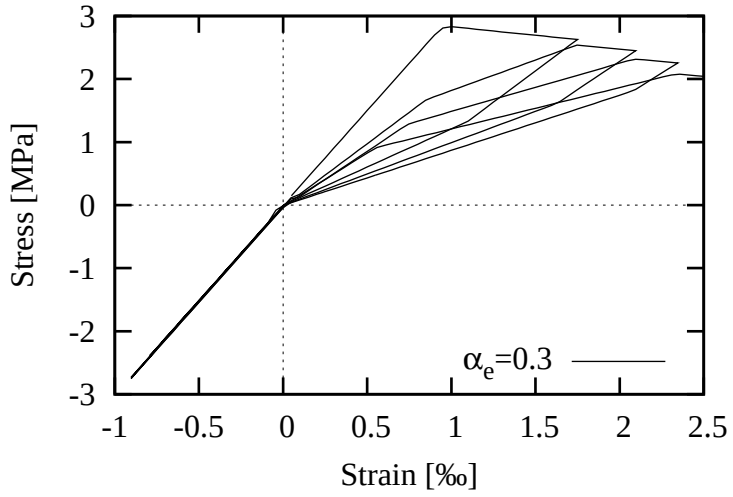

Figure 7: Response of an uniaxial deformation with $\alpha_e = 0.3$. Three cycles are loaded to a strain of: 1.70 ‰, 2.0 ‰ and 2.25 ‰, and unloaded to a stress of -3.0 MPa.

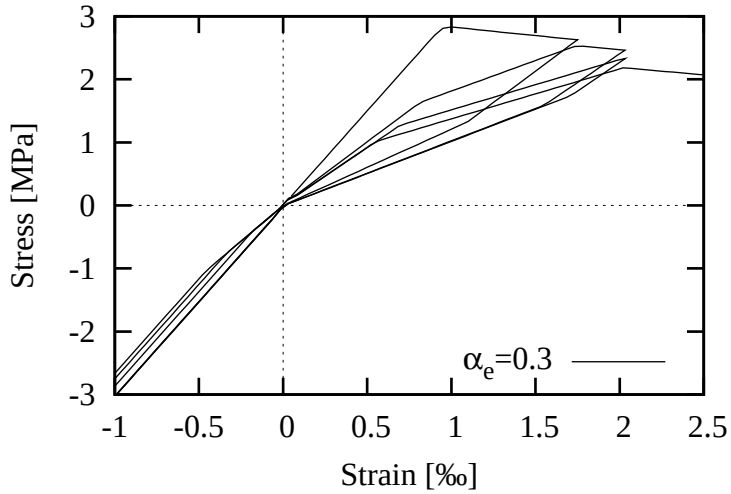

Figure 8: Response of an uniaxial deformation with $\alpha_{\mathrm{e}} = 0.3$. Three cycles are loaded to a strain of: 1.70 ‰, 2.0 ‰ and 2.25 ‰, and unloaded to a strain of -11.0 ‰, -10.75 ‰ and -10.50 ‰.

6.2 The influence of α_{e} on the stress-strain response

In Figure 9 the extremities of α_{e} that corresponds to a pure plastic- or damage response of the dual-model is shown for one cycle in uniaxial tension unloaded to -3.0 MPa. During the elastic- and softening phase the response is similar, but at unloading the pure damage configuration unloads with a damaged stiffness to the origin; while the pure plastic response unloads with the same stiffness as the initial. When the plastic configuration reach zero stress plastic flow at unloading is initiated and evolves as long as the distortional energy is negative or the stress is reversed. To present the influence of α_{e} on the hysteresis loops three values are presented in Figure 10 for one cycle unloaded to -3.0 MPa. It shows that a value of α_{e} which corresponds to higher contribution of the damage part leads to a reduced size of the hysteresis loops, because of the reduction of plastic flow. It can also be observed that the deviation from the initial softening branch differs for different values of α_{e}: a higher contribution of the plastic part results in a larger deviation. This increased deviation is motivated by the larger sized hysteresis loop and is a consequence of a larger plastic flow; hence, further development on the softening branch of the plastic part. From this discussion a reasonable value of $\alpha_{\mathrm{e}} = \sim 0.3$ is extracted for further application.

6.3 Study of the distortional energy W^{D}

One of the most important variables in the dual-model is the distortional energy W^{D} as it controls the duration of yielding at unloading. W^{D} is studied for one cycle that ends at 0 deformation. In Figure 11 and 11 c the stress-strain response and the distortional energy is shown for the earlier considered values of α_{e}, respectively. To

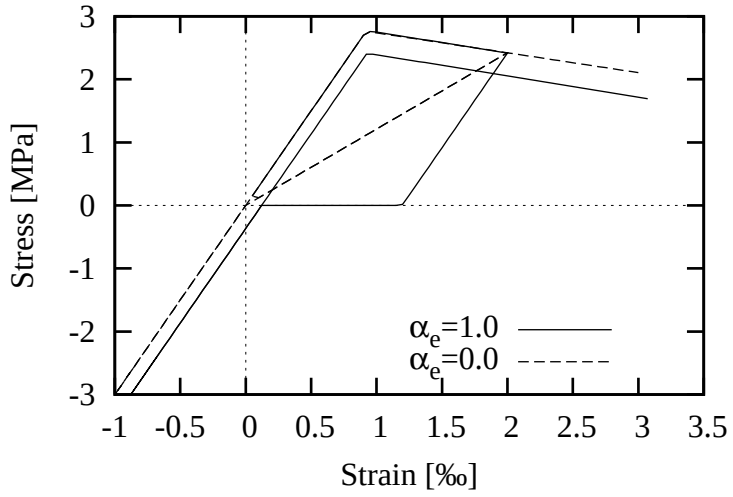

Figure 9: Response of an uniaxial deformation with $\alpha_e = 1.0$ and $\alpha_e = 0.0$.

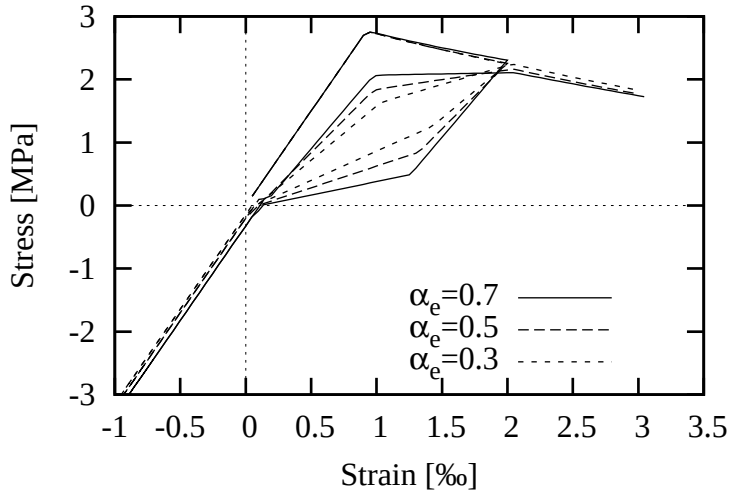

Figure 10: Response of an uniaxial deformation with $\alpha_e = 0.7$, $\alpha_e = 0.5$ and $\alpha_e = 0.3$.

get an idea of a pure response no confinement is added at this stage. In the stress-strain response (Figure 11) the consequence of increased contribution of the plastic part is observed as increased unloading stiffness and amount of plastic deformation of unloading. There is a small difference in the response after peak-load, but before unloading. This difference shows that the softening branch depends on α_e through the term $\alpha_e\omega$ found in the stress-strain relationship (Equation 24). Observing the evolution of distortional energy in Figure 11 c shows that no negative energy is produced for the case of pure damage. While, for an increased contribution of plasticity the duration of negative distortional energy is approximately the same.

In the next step confinement is added with fixed lateral boundaries, which introduce a lateral state of tension that decreases the elastic phase of loading as well

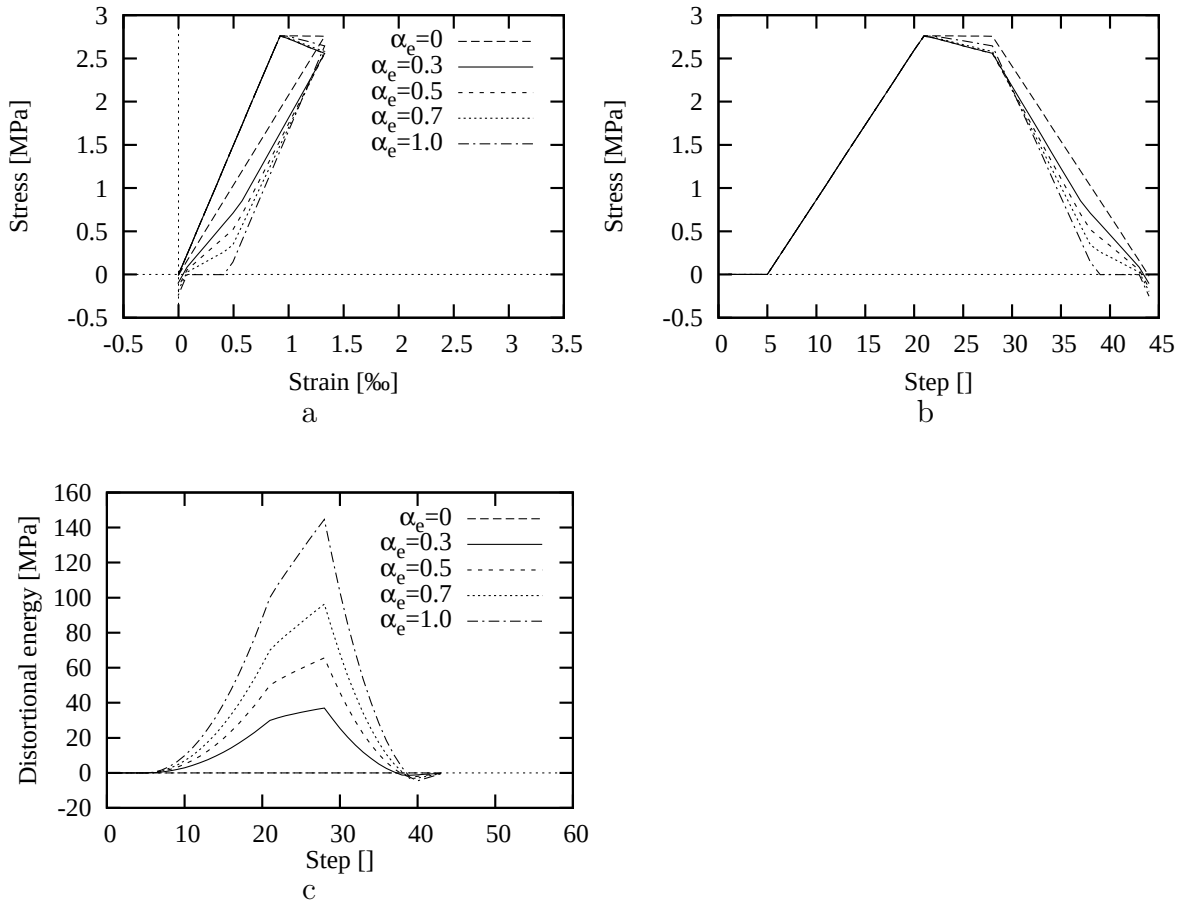

Figure 11: Analyses without lateral confinement for: $\alpha_{\mathrm{e}} = 0$, $\alpha_{\mathrm{e}} = 0.3$, $\alpha_{\mathrm{e}} = 0.5$, $\alpha_{\mathrm{e}} = 0.7$, and $\alpha_{\mathrm{e}} = 1.0$. a/ Stress-strain response, b/ evolution of the stress and c/ behaviour of the distortional energy W^{D}.

as unloading (Figure 12 a). In contrast to the unconfined response the confined unloading unloads towards a confined state due to the volumetric-plastic expansion during yielding of loading. A plastic unloading state is observed for all cases with $\alpha_{\mathrm{e}} \geq 0$ and is very dominant for the pure plastic case. At this point the stiffness changes since the plastic deviatoric stress component has reached the inner-yield surface. The deviatoric stress component decreases rapidly during unloading because of the high lateral stress components. Thus, when all the nominal-stress components intersect the inner-yield surface is reached. For fixed boundaries the distortional energy decreases rapidly after peak-load which results in a larger phase of negative distortional energy compared to the response of free boundaries (Figure 11).

In Figure 13 the response from the case with fixed boundaries (Figure 12) is presented in stress-invariants. The figures explain the change of stiffness at unloading seen in Figure 12 a. The change of stiffness is related to the plastic flow. As plastic flow occurs for $\alpha_{\mathrm{e}} \geq 0$ the point of stress-return shifts along the yield surface. This

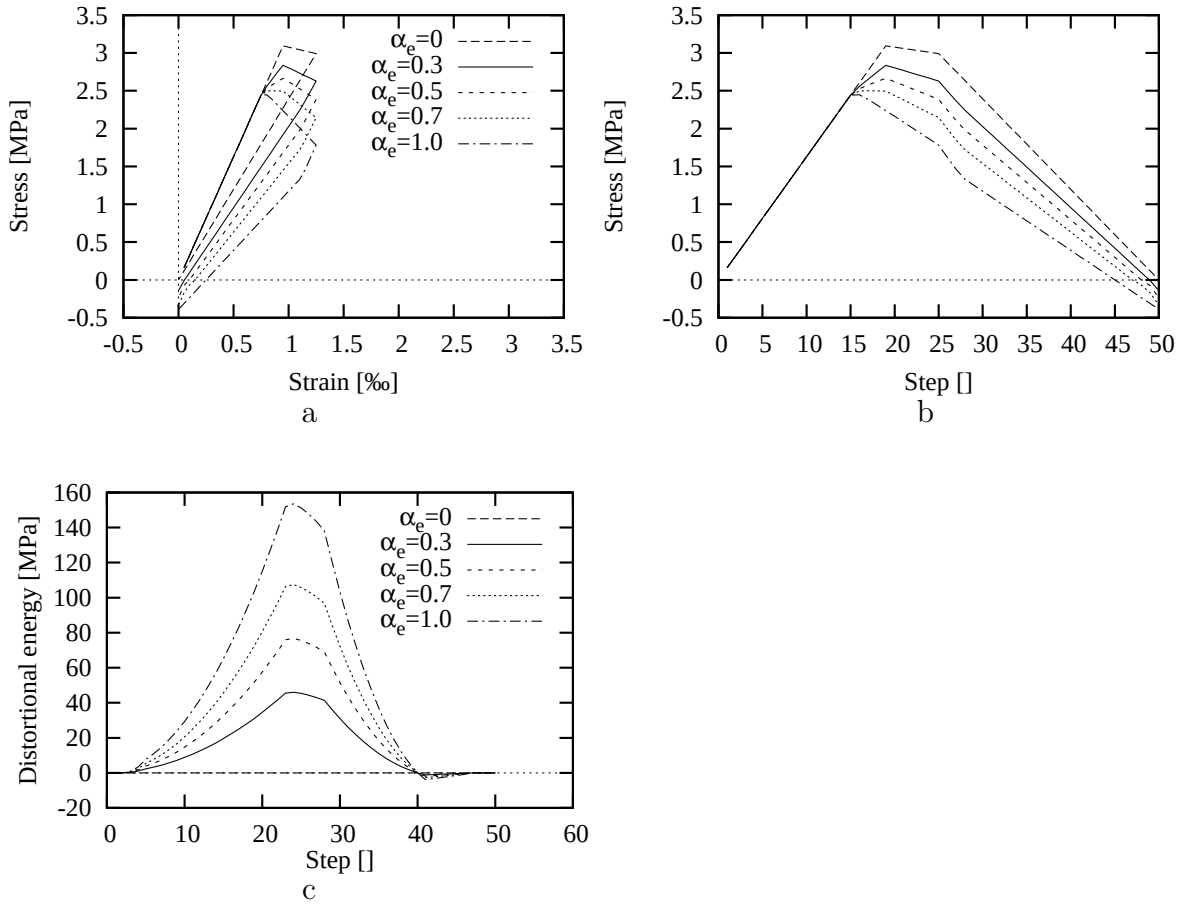

Figure 12: Analyses with fixed boundaries for: $\alpha_e = 0$, $\alpha_e = 0.3$, $\alpha_e = 0.5$, $\alpha_e = 0.7$, and $\alpha_e = 1.0$. a/ Stress-strain response, b/ evolution of the stress and c/ behaviour of the distortional energy W^D.

shift is dependent on a load direction that is not normal to the yield surface; thus, nor is the elastic predictor. However, the plastic corrector is evaluated along the normal to the plastic potential. This type of plastic flow consequently yields the shift along the yield surface. In Figure 13 it is seen that for $\alpha_e = 0$ there is no change of stiffness and no sliding along the yield surface; while, for $\alpha_e \geq 0$ this sliding increases and the stress drops consequently during plastic flow.

In Figure 14 the evolution of distortional energy of two confinement states are compared to the above presented states of free- and fixed boundaries. The results are concluded as:

- An increase in duration of negative distortional energy is observed for states of positive lateral strain. This is due to increased volumetric-plastic strain when loading and unloading is applied.
- For negative lateral strain the amount of produced distortional energy is in-

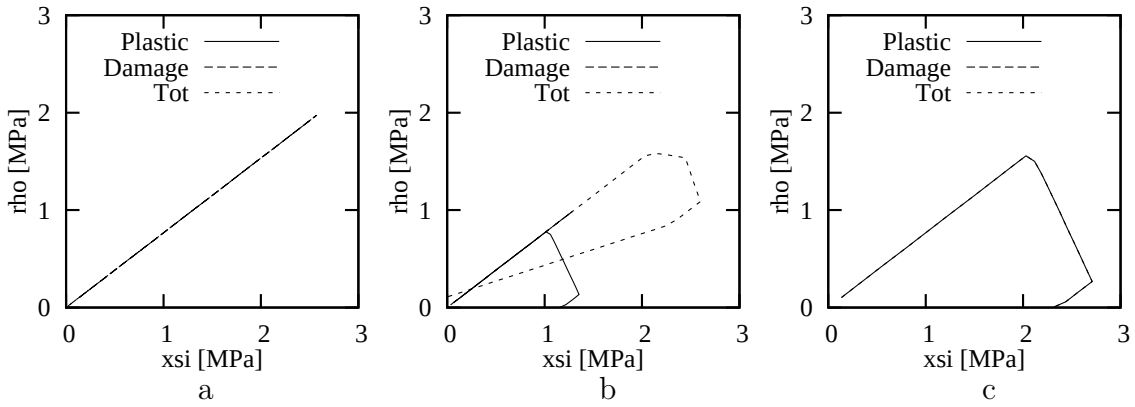

Figure 13: Haigh-Westergaard coordinates for fixed boundaries: a $\alpha_{\mathrm{e}} = 0$, b/ $\alpha_{\mathrm{e}} = 0.5$, and c/ $\alpha_{\mathrm{e}} = 1.0$.

creased compared to positive lateral strain. This is related to smaller volumetric-plastic strain.

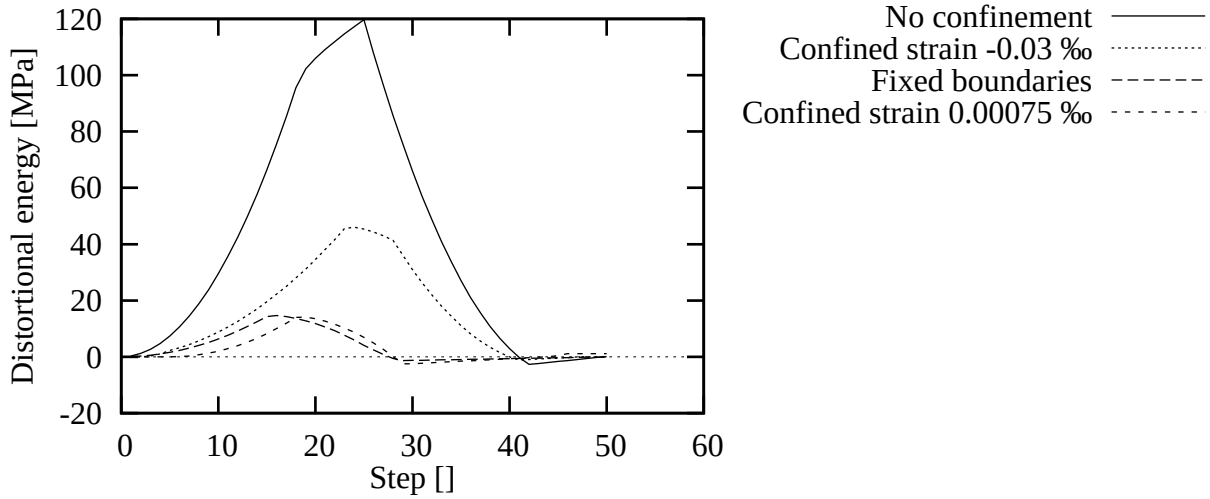

Figure 14: Behaviour of the distortional energy $W^{\mathrm{D}} = 1/2\boldsymbol{s} : \boldsymbol{e}$ for: $\alpha_{\mathrm{e}} = 0.3$.

7 Conclusions

A constitutive model was developed that aims at describing the response of concrete subjected to cyclic loading in tension with stress reversal to reasonable high compression stress. The proposed model is based on a parallel combination of plasticity and damage mechanics. The following parameters are proposed and considered to be decisive for describing concrete subjected to cyclic loading:

- A parameter that controls the contribution to the overall stiffness of the two theories, α_{e}. This parameter also influences the size of the characteristic hysteresis loops of cyclic loaded concrete: a value that corresponds to more damage decreases the size of the hysteresis loops.

- A parameter that controls the stress state, σ_{v}. This choice limits the model to only consider volumetric cyclic-unloading, i.e. stress reversal parallel to the hydrostatic axis. The benefit of this choice is that the stress state is well defined.

- A parameter that determines the duration of yielding of cyclic-unloading, W^{D}, which is influenced by α_{e} and lateral confinement.

  Thus, it can be concluded that the constitutive response of the model agrees with the physical reality: The over-all softening response is described with the damage part, while the plastic deformation at cyclic-loading as well as -unloading is described by the plastic part. In addition, the damage part decreases the cyclic-unloading stiffness. Moreover, completed hysteresis loops decreases the remaining fracture energy so that a new softening trend is achieved.

Acknowledgements

The simulations were performed with the object-oriented finite element package OOFEM (Patzák, 1999; Patzák and Bittnar, 2001) extended by the present authors.

References

Abu-Lebdeh, T. and Voyiadjis, G. (1993). Plasticity-Damage Model for Concrete under Cyclic Multiaxial Loading, *Journal of Engineering Mechanics-Asce*, Vol. 119, No. 7, pp. 1465–1484.

Baluch, M. H., Qureshy, A. B. and Azad, A. K. (1987). Fatigue crack propagation in plain concrete, *Fracture of Concrete and Rock: SEM-RILEM International Conference.*, Soc for Experimental Mechanics Inc, Bethel, CT, USA, Houston, TX, USA, pp. 112–119.

CEB (1988). *Fatigue of concrete structures, State of the art report*, Tech. Rep. 188.

Clemmer, H. (1922). Fatigue of concrete, *Proceedings of the American Society for Testing Materials*, 2, pp. 408–419.

Cornelissen, H. A. W., Hordijk, D. A. and Reinhardt, H. W. (1986). Experimenatal determination of crack softening characteristics of normalweight and lightweight concrete, *Heron*, Vol. 31, No. 2, pp. 45–56.

Crepps, R. (1923). Fatigue of mortar, *Proceedings of the American Society for Testing Materials*, 2, pp. 329–340.

Dafalias, Y. F. (1986). Bounding surface plasticity. I: Mathematical foundation and hypoplasticity, *Journal of Engineering Mechanics*, Vol. 112, No. 9,, pp. 966–987.

Desmorat, R., Ragueneau, F. and Pham, H. (2007). Continuum damage mechanics for hysterisis and fatigue of quasi-brittle materials and structures, *International Journal for Analytical and Numerical Methods in Geomechanics*, Vol. 31, pp. 307–329.

Gopalaratnam, V. and Shah, S. (1985). Softening response of plain concrete in direct tension, *Journal of the American Concrete Institute*, Vol. 82, No. 3, pp. 310–323.

Grassl, P. and Rempling, R. (2006). Influence of volumetric-deviatoric coupling on crack prediction in concrete fracture tests, *Accepted for publication in Engineering Fracture Mechanics,*, pp. 16.

Grassl, P. and Rempling, R. (2008). A damage-plasticity interface approach to mesoscale modelling of heterogeneous materials subjected to cyclic loading, *Engineering Fracture Mechanics*, Vol. 75, No. 16, pp. 4804–4818.

Gylltoft, K. (1983). *Fracture mechanics models for fatigue in concrete structures.*, Doctoral thesis 1983:25d, Luleå University of Technology, pp. 210.

Hai-cheng, L., Wei, C. and Yu-pu, S. (2004). Fatigue properties of plain concrete under triaxial compressive cyclic loading, *China Ocean Engineering*, Vol. 18, No. 3, pp. 457–468.

Holmberg, G. (2001). *Fatigue of Concrete Piles of High Strength Concrete Exposed to Impact Load*, Licentiate thesis, Chalmers University of Technology, pp. 71.

Holmen, J. (1979). *Fatigue of concrete by constant and variable amplitude loading*, Doctoral thesis, The Norwegian Institute of Technology, Trondheim, Norway, No. 79-1, pp. 218.

Hordijk, D. (1991). *Local approach to fatigue of concrete*, Doctoral thesis, Technische universiteit te Delft, The Netherlands, ISBN 90-9004519-8, pp. 210.

Imran, I. (1994). *Applications of non-associated plasticity in modelling the mechanical response of concrete*, Doctoral thesis, Department of Civil Engineering, Univerity of Toronto, Canada, pp. 208.

Jason, L., Pijaudier-Cabot, G., Huerta, A., Crouch, R. and Ghavamian, S. (2004). An elastic plastic damage formulation for the behavior of concrete, Li, V., Leung, C., Willam, K. and Billington, S., eds., *Fracture mechanics of concrete structures*, pp. 549–556.

Jirasek, M. and Bazant, Z. P. (2001). *Inelastic analysis of structures*, John Wiley and Sons, 1 ed.

Johansson, U. (2004). *Fatigue tests and analysis of reinforced concrete bridge deck models*, Licentiate thesis, Royal Institute of Tecjnology, pp. 198.

Karsan, I. D. and Jirsa, J. O. (1969). Behaviour of concrete under compressive loadings, *Journal of Structural Division-ASCE*, Vol. 95, pp. 2543–2563.

Lee, J. and Fenves, G. (1998). Plastic-damage model for cyclic loading of concrete structures, *Journal of Engineering Mechanics-Asce*, Vol. 124, No. 8, pp. 892–900.

Murdock, J. (1965). A critical review of research on fatigue of plain concrete, *Univeristy of Illinois College of Engineering, Engineering experiment station*, Vol. 62, No. 62.

Murdock, J. and Kesler, C. (1958). Effect of range of stress on fatigue strength of plain concrete beams, *ACI Journal*, pp. 221–231.

Ottosen, N. S. (1977). A failure criterion for concrete, *Journal of Engineering Mechanics, ASCE*, Vol. 103, pp. 527–535.

Pandolfi, A. and Talercio, A. (1998). Bounding surface models applied to fatigue of plain concrete, *Journal of engineering Mechanics*, Vol. 124, pp. 556–564.

Papa, E. and Taliercio, A. (1996). Anisotropic damage model for the multiaxial static and fatigue behaviour of plain concrete, *Engineering Fracture Mechanics*, Vol. 55, pp. 163–179.

Patzák, B. (1999). Object oriented finite element modeling, *Acta Polytechnica*, Vol. 39,, pp. 99–113.

Patzák, B. and Bittnar, Z. (2001). Design of object oriented finite element code, *Advances in Engineering Software*, Vol. 32,, pp. 759–767.

Petkovic, G. (1991). *Properties of concrete related to fatigue damage with emphasis in high strength concrete*, Phd, Univeristetet i Trondheim, Norges tekniske hogskole, pp. 217.

Plizzari, G., Cangiano, S. and Alleruzzo, S. (1997). The fatigue behaviour of cracked concrete, *Fatigue and Fracture of Engineering Materials and Structures*, Vol. 20, No. 8, pp. 1195–1206.

Ragueneau, F., Borderie, C. L. and Mazars, J. (2000). Damage model for concrete-like materials coupling cracking and friction, contribution towards structural damping: first uniaxial applications, *Mechanics of Cohesive-Frictional Materials*, Vol. 5, pp. 607–625.

Reinhardt, H. W. (1984). Fracture mechanics of an elastic softening material like concrete, *Heron*, Vol. 29, No. 2, pp. 42.

Reinhardt, H. W., Cornelissen, H. A. W. and Hordijk, D. A. (1986). Tensile tests and failure analysis of concrete., *Journal of Structural Engineering*, Vol. 112, No. 11, pp. 2462–2477.

Rempling, R. and Grassl, P. (2008). A parametric study of the meso-scale modelling of concrete subjected to cyclic compression, *Submitted to Computers and Concrete*.

Simo, J. and Ju, J. (1987). Strain-Based and Stress-Based Continuum Damage Models 1. Formulation, *International Journal of Solids And Structures*, Vol. 23, No. 7, pp. 821–840.

Sinha, B. P., Gerstle, K. H. and Tulin, L. G. (1964). Stress-strain relations for concrete under cyclic loading, *American Concrete Institute – Journal*, Vol. 61, No. 2, pp. 195.

Spooner, D. and Dougill, J. (1975). Quantitative Assessment of Damage Sustained in Concrete During Compressive Loading, *Magazine of Concrete Research*, Vol. 27, No. 92, pp. 151–160.

Svahn, P.-O. (2005). *Dynamic Behaviour of Reinforced Concrete Structures: Analyses with a strong discontinuity approach*, Doctoral thesis, Chalmers University of Technology, pp. 46.

Tepfers, R. (1978). *En undersökning av betongens utmattningshållfashet*, Tech. Rep. R86:1978, Avdelningen för husbyggnadsteknik, Chalmers University of Technology, Sweden,, pp. 121.

Thun, H. (2006). *Assessment of Fatigue Resistance and Strength in Existing Concrete Structures*, Doctoral thesis, Luleå University of Technology, pp. 48.

Mier, van , J. (1984). *Strain-softening of concrete under multiaxial loading conditions*, Doctoral thesis, Technische hogeschool Eindhoven, pp. 248.

Mier, van , J. G. M. (1986). Fracture of concrete under complex stress, *HERON*, Vol. 31, No. 3, pp. 89.

Voyiadjis, G. Z. and Abulebdeh, T. M. (1993). Damage Model for Concrete Using Bounding Surface Concept, *Journal of Engineering Mechanics-ASCE*, Vol. 119, No. 9,, pp. 1865–1885.

Voyiadjis, G. Z. and Abulebdeh, T. M. (1994). Plasticity Model for Concrete Using the Bounding Surface Concept, *International Journal of Plasticity*, Vol. 10, No. 1,, pp. 1–21.

Winnicki, A. and Cichon, C. (1998). Plastic model for concrete in plane stress state. i.: Theory, *Journal of Engineering Mechanics*, Vol. 124, pp. 591–602.

Yang, B.-L., Dafalias, Y. F. and Herrmann, L. R. (1985). BOUNDING SURFACE PLASTICITY MODEL FOR CONCRETE, *Journal of Engineering Mechanics*, Vol. 111, No. 3, pp. 359.

Nomenclature

$\dot{}$	Superscript: Rate of ...
^{n}	Superscript: Number of iterations
$^{\mathrm{D}}$	Superscript: ... of the damage part
$^{\mathrm{P}}$	Superscript: ... of the plastic part
$^{\mathrm{Trial}}$	Superscript: Trial state
$^{\emptyset}$	Superscript: ... of inner yield surface
$_{\mathrm{e}}$	Subscript: Elastic part of ...
$_{\mathrm{p}}$	Subscript: Plastic part of ...
$_1$	Subscript: First variable of principal direction
$_\rho$	Subscript: Deviatoric part of ...
$_\xi$	Subscript: Volumetric part of ...
C_1, C_2, C_3	Ottosen yield surface material parameter
$\boldsymbol{D}_{\mathrm{ep}}$	Tangential stiffness matrix
$\boldsymbol{D}_{\mathrm{s}}$	Secant stiffness matrix
D	Dissipation of energy
D_κ	Energy conjugate
D_ω	Energy conjugate
$\boldsymbol{e}$	Deviatoric part of the strain
f	Loading- and yield function
f_{y}	Yield stress
$\boldsymbol{g}_{\Omega\Omega}$	Second derivative of the plastic potential

$\boldsymbol{g}_\Omega$	First derivative of the plastic potential
G	Elastic shear modulus
g	Plastic potential
H	Hardening modulus for yielding
H_{P}^*	Softening function of the plastic part in tension
J_2	Second stress invariant
K	Elastic bulk modulus
q_{h}	Hardening function
$R_{1,2,3}$	Residuals for the plastic part
$\boldsymbol{s}$	Deviatoric part of the stress
T	Temperature
W	Energy
W_{D}	Distortional energy
W_{V}	Volumetric part of the energy
α_{e}	Distribution of free energy between damage and plastic part
α_ϕ	Dilatancy coefficient of the outer-yield surface potential
δ	Iterative change
$\boldsymbol{\delta}$	Kronecker delta
$\tilde{\varepsilon}$	Equivalent strain
ε_0	Uniaxial strain at the onset of damage
ε_{f}	Uniaxial strain for which no stress transfear is possible
ε_{v}	Volumetric part of the strain
$\boldsymbol{\varepsilon}$	Strain tensor
κ	History variable
λ	PLastic multiplier
ψ	Free energy
ρ	Haigh-Westergaard coordinate for the deviatoric stress

ρ_ψ	Mass density
σ_{v}	Volumetric part of the stress tensor
$\boldsymbol{\sigma}$	Stress tensor
ξ	Haigh-Westergaard coordinate for the volumetric stress

This page intentionally contains only this sentence.

Doctoral Theses in Civil Engineering, Chalmers University of Technology, 1946 - 1966

Theses are given in order of time of publication. The numbers refer to the two series of dissertations at Chalmers University of Technology (the original, 1941-1975, and the new from 1971). The first Ph D dissertation was arranged in1948 although the first theses were published earlier.

Löfquist, Bertil (1946): *Temperatureffekter i hårdnande betong. Undersökning av några faktorer som påverka sprickbildningen i grövre konstruktioner - Jämförelse mellan två svenska cement.* (Temperature Effects on Hardened Concrete, Investigation of some Factors that influences the Cracking in Massive Structures. A Comparison between two Swedish Cement Qualities. In Swedish). No. 3, 195 pp

Tengvik, Nils (1952): *Den svenska byggnadsmaterialmarknaden. Produktion, distribution och prissättning av jord- och stenindustrins material.* (The Swedish Building Material Market. Producion, Distribution and Prices on Material from Earth and Stone Industry. In Swedish). No. 7, 318 pp.

Ödman, Sven (1955): *Studies of Boundary Value Problems*. No. 10, 10 pp + app.

Kärrholm, Gunnar (1956): *Parallelogram Plates Analysed by Strip Method*. No. 11, 196 pp.

Larsson, Lars-Erik (1959): *Bearing Capacity of Plain and Reinforced Concrete Walls*. No. 20. 248 pp.

Hansbo, Sven (1960): *Consolidation of Clay, with Special Reference to Influence of Vertical Sand Drains. A Study Made in Connection with Full-scale Investigation at Skå-Edeby*. No. 25, 160 pp.

Hedar, Per Anders (1960): *Stability of Rock-fill Breakwaters*. No 26, 119 pp.

Losberg, Anders (1960): *Structurally Reinforced Concrete Pavements*. No. 29, 444 pp.

Samuelsson, Alf (1962): *Linear Analysis of Frame Structures by Use of Algebraic Topology*. No. 36, 115 pp.

Åkesson, Bengt Å (1966): *On Lévy's Plate Solution*. No. 52, 16 pp + app.

Backsell, Gunnar (1966): *Experimental Investigations into Deformations Resulting from Stresses Perpendicular to Grain in Swedish Whitewood and Redwood in Respect of the Dimensioning of Concrete Formwork.* No. 57, 113 pp.

Doctoral Theses in Concrete Structures, Chalmers University of Technology, 1967 – 1989

Cederwall, Krister (1971): *Time-dependent behaviour of reinforced concrete structures.* No 109. Published as Document 1971:3 by the National Swedish Building Research and as Publication 71:1 by the Division of Concrete Structures, 173 pp.

Elfgren, Lennart (1971); *Reinforced Concrete Beams Loaded in Combined Torsion, Bending and Shear: A Study of the Ultimate Load-Carrying Capacity*. New Series No 28. Publication 71:3 by the Division of Concrete Structures, 202 pp. Second Ed 1972, 230 pp. Available at: http://www.ltu.se/shb/2.2079/d155/d4946/d19273

Karlsson, Inge (1973): *Stiffness Properties of Reinforced Concrete Beams in Combined Torsion, Bending and Shear*. No 126. Publication 73:1 by the Division of Concrete Structures, 203 pp.

Tepfers, Ralejs (1973): *A Theory of Bond Applied to Overlapped Tensile Reinforcement Splices for Deformed Bars.* No 122A. Publication 73:2 by the Division of Concrete Structures, 328 pp. Available at: http://documents.vsect.chalmers.se/structural-engineering/TepfersDrThesis.pdf

Nilsson, Ingvar H. E. (1973): *Reinforced Concrete Corners and Joints Subjected to Bending Moment: Design of Corners and Joints in Frame Structures*, New Series No 90. Also published as Document 1973:7 by the National Swedish Building Research and as Publication 73:6 by the Division of Concrete Structures, 249 pp.

Cajdert, Arne (1980): *Laterally Loaded Masonry Walls.* New Series No 346. Publication 80:5 by the Division of Concrete Structures, 283 pp.

Berge, Olav (1981): *Armerade konstruktioner i lättballastbetong (Reinforced Structures in Lightweight Aggregate Concrete. In Swedish),* New Series No 357. Publication 81:3 by the Division of Concrete Structures, 373 pp.

Licentiate Theses and Doctoral Theses, Concrete Structures,
Chalmers University of Technology, 1990-

90:1 Stig Öberg: *Post Tensioned Shear Reinforcement in Rectangular RC Beams*. Publication 90:1. Göteborg, April 1990. 603 pp. (No. 1021). Doctoral Thesis.

90:2 Johan Hedin: *Långtidsegenskaper hos samverkanskonstruktioner av stål och betong (Long Time Behaviour of Composite Steel Concrete Structures)*. Publication 90:2. Göteborg, August 1990. 53 pp. (No. 1079). Licentiate Thesis.

92:1 Björn Engström: *Ductility of Tie Connections in Precast Structures*. Publication 92:1. Göteborg, October 1992. 368 pp. (Nos. 936, 999, 1023, 1052). Doctoral Thesis.

93:1 Mario Plos: *Shear Behaviour in Concrete Bridges - Full Scale Shear Test. Fracture Mechanics Analyses and Evaluation of Code Model*. Publication 93:1. Göteborg, April 1993. 70 pp. (Nos. 1088, 1084). Licentiate Thesis.

93:2 Marianne Grauers: *Composite Columns of Hollow Steel Sections Filled with High Strength Concrete*. Publication 93:2. Göteborg, June 1993. 140 pp. (No. 1077). Doctoral Thesis.

93:4 Li An: *Load Bearing Capacity and Behaviour of Composite Slabs with Profiled Steel Sheet*. Publication 93:4. Göteborg, September 1993. 134 pp. (No. 1075). Doctoral Thesis.

93:5 Magnus Åkesson: *Fracture Mechanics Analysis of the Transmission in Zone in Prestressed Hollow Core Slabs*. Publication 93:5. Göteborg, November, 1993. 64 pp. (No 1112). Licentiate Thesis.

95:1 Christina Claeson: *Behavior of Reinforced High Strength Concrete Columns*. Publication 95:1. Göteborg, June 1995. 54 pp. (No. 1105). Licentiate Thesis.

95:2 Karin Lundgren: *Slender Precast Systems with Load-Bearing Facades*. Publication 95:2. Göteborg, November 1995. 60 pp. (No. 1098). Licentiate Thesis.

95:3 Mario Plos: *Application of Fracture Mechanics to Concrete Bridges. Finite Element Analysis and Experiments*. Publication 95:3. Göteborg, November 1995. 127 pp. (Nos. 1067, 1084, 1088, 1106). Doctoral Thesis.

96:1 Morgan Johansson: *New Reinforcement Detailing in Concrete Frame Corners of Civil Shelters. Non-linear Finite Element Analyses and Experiments*. Publication 96:1. Göteborg, November 1996. 77 pp. (No. 1106). Licentiate Thesis.

96:2 Magnus Åkesson: *Implementation and Application of Fracture Mechanics Models for Concrete Structures*. Publication 96:2. Göteborg, November 1996. 159 pp. (No. 1112). Doctoral Thesis.

97:1 Jonas Magnusson: *Bond and Anchorage of Deformed Bars in High-Strength Concrete*. Publication 97:1. Göteborg, November 1997. 234 pp. (No. 1113). Licentiate Thesis.

98:1 Christina Claeson: *Structural Behavior of Reinforced High-Strength Concrete Columns*. Publication 98:1. Göteborg 1998. 92 pp + I-IV, 75 pp. (No. 1105). Doctoral Thesis.

99:1 Karin Lundgren: *Three-Dimensional Modelling of Bond in Reinforced Concrete. Theoretical Model, Experiments and Applications.* Publication 99:1. Göteborg, November 1999. 129 pp. (No. 37). Doctoral Thesis.

00:1 Jonas Magnusson: *Bond and Anchorage of Ribbed Bars in High-Strength Concrete*. Publication 00:1. Göteborg, February 2000. 300 pp. (No. 1113). Doctoral Thesis.

00:2 Morgan Johansson: *Structural Behaviour in Concrete Frame Corners of Civil Defence Shelters*. Publication 00:2. Göteborg, March 2000. 220 pp. (No. 1106). Doctoral Thesis.

00:3 Rikard Gustavsson: *Static and Dynamic Finite Element Analyses of Concrete Sleepers*. Publication 00:3. Göteborg, March 2000. 58 pp. (No. 41). Licentiate Thesis.

00:4 Mathias Johansson: *Structural Behaviour of Circular Steel-Concrete Columns. Non-linear Finite Element Analyses and Experiments*. Publication 00:4. Göteborg, March 2000. 64 pp. (No. 48). Licentiate Thesis.

01:3 Gunnar Holmberg: *Fatigue of Concrete Piles of High Strength Concrete Exposed to Impact Load*. Publication 01:3. Göteborg, August 2001. 69 pp. (No. 55). Licentiate Thesis.

02:1 Peter Harryson: *Industrial Bridge Construction – merging developments of process, productivity and products with technical solutions*. Publication 02:1. Göteborg, January 2002. 90 pp. (No. 34). Licentiate Thesis.

02:2 Ingemar Löfgren: *In-situ concrete building systems – developments for industrial constructions*. Publication 02:2. Göteborg, March 2002. 125 pp. (No. 35). Licentiate Thesis.

02:4 Joosef Leppänen: *Dynamic Behaviour of Concrete Structures subjected to Blast and Fragment Impacts.* Publication 02:4. Göteborg, April 2002. 78 pp. (No. 31). Licentiate Thesis.

02:5 Peter Grassl: *Constitutive Modelling of Concrete in Compression*. Publication 02:5. Göteborg, May 2002. 95 pp. (No. 37). Licentiate Thesis.

02:6 Rikard Gustavson: *Structural Behaviour of Concrete Railway Sleepers*. Publication 02:6. Göteborg, September 2002. 180 pp. (No. 32). Doctoral Thesis.

02:8 Mathias Johansson: *Composite Action and Confinement Effects in Tubular Steel-Concrete Columns*. Publication 02:8. Göteborg, November 2002. 173 pp. (No. 33). Doctoral Thesis.

03:1 Per-Ola Svahn: *Impact-Loaded Concrete Piles – Theoretical and experimental study of load effects and capacity*. Publication 03:1. Göteborg, May 2002. 99 pp. (No. 38). Licentiate Thesis.

04:3 Peter Grassl: *Plasticity and Damage Mechanics for Modeling Concrete Failure*. Publication 04:3. Göteborg, September 2004. 159 pp. Doctoral Thesis.

04:4 Joosef Leppänen: *Concrete Structures Subjected to Fragment Impacts – Dynamic Behaviour and Material Modelling*. Publication 04:4. Göteborg, October 2004. 125 pp. (No. 31). Doctoral Thesis.

2005 Helen Broo: *Shear and Torsion Interaction in Prestressed Hollow Core Slabs.* Lic 2005:2. Göteborg 2005. 83 pp. Licentiate Thesis.

2005 Per-Ola Svahn: *Dynamic Behaviour of Reinforced Concrete Structures: Analyses with a Strong Discontinuity Approach.* Ny serie nr 2366. Göteborg 2005. 159 pp. Doctoral Thesis.

2005 Ingemar Löfgren: *Fibre-reinforced Concrete for Industrial Construction – a fracture mechanics approach to material testing and structural analysis.* Ny serie nr. 2378. Göteborg 2005. pp 243.

2006 Rasmus Rempling: *Constitutive Modelling of Concrete Subjected to Tensile Monotonic and Cyclic Loading*. Lic 2006:4. Göteborg 2006. 59 pp. Licentiate Thesis.

2008 Anette Jansson: *Fibres in Reinforced Concrete Structures – analysis, experiments and design*. Lic 2008:3. Göteborg 2008. 84 pp. Licentiate Thesis.

2008 Ulrika Nyström: *Concrete Structures Subjected to Blast and Fragment Impacts, Numerical Simulations of Reinforced and Fibre-reinforced Concrete*. Lic 2008:4. Göteborg 2008. 117 pp. Licentiate Thesis.

2008 Kamyab Zandi Hanjari: *Load-Carrying Capacity of Damaged Concrete Structures*. Lic 2008:6. Göteborg 2008. 108 pp. Licentiate Thesis.

2008 Peter Harryson: *Industrial Bridge Engineering – Structural developments for more efficient bridge construction*. Ny serie nr. 2810. Göteborg 2008. Doctoral Thesis.

2008 Helén Broo: *Shear and Torsion in Concrete Structures. Non-Linear Finite Element Analysis in Design and Assessment*. Ny serie nr. 2786. Göteborg 2008. Doctoral Thesis.